High-Resolution Experiments of Momentum- and Buoyancy-Driven Flows for the Validation and Advancement of Computational Fluid Dynamics Codes

by

Daniel Nunez

A dissertation submitted in partial fulfillment
of the requirements for the degree of
Doctor of Philosophy
(Nuclear Engineering and Radiological Sciences)
in The University of Michigan
2020

Doctoral Committee:

Professor Annalisa Manera, Co-Chair
Dr. Victor Petrov, Co-Chair
Dr. David Pointer
Professor Xiaodong Sun
Assistant Professor Aaron Towne

– Jorge Cham, PhD Comics

"The whole purpose of education is to turn mirrors into windows."

– Sydney Justin Harris

"Education's purpose is to replace an empty mind with an open one."

– Malcolm Stevenson Forbes

danielnu@umich.edu

ORCID ID: 0000-0002-7187-750X

2020

To my parents, Felix and Rosa

Acknowledgements

"Sometimes it takes more courage to ask for help than to act alone."

— Ken Petti

First and foremost, I would like to thank my co-advisors Annalisa Manera and Victor Petrov for their invaluable guidance and unconditional support. Without their help, I could not have completed this thesis. Annalisa, Victor, thank you for believing in me and teaching me how to approach research with curiosity, patience, and optimism. Thank you for helping me adopt these qualities, and I apologize for not putting these three pieces together early on during my Ph.D. I realize how fortunate I am, and I sincerely believe that having you both as my mentors was the perfect combination. I am indebted for the opportunities you provided me with throughout these years. Thank you.

Second, I would like to thank my committee for their invaluable support, fruitful discussions, and suggestions. I would like to thank all of the postdoctoral researches and visiting scholars that joined our group. Especially, I would like to thank Benedikt for several fruitful discussions that further sparked my curiosity about turbulence. I would also like to express my most sincere gratitude to all my colleagues from the Experimental and Computational Multiphase Flow group. In particular, I would like to thank John, Julio, and Sunming for their emotional support, entertaining discussions, and for all of their help inside and outside the laboratory. It was a pleasure working with and learning from each one of you. I will miss you all.

I would like to thank all of my friends who made my stay at Michigan a delightful time. Ben, thank you for being such a great friend and for always willing to lend a helping hand. I

cannot describe how thankful I am for all of your support throughout these years. I would like to thank Anna, Anthony, Darby, and Stephanie for believing in me. I could not have achieved my goals without your words of encouragement. I would like to thank all of my friends from Dance Revolution for helping me relax during the stressful times. I would also like to thank all of my professors and classmates who helped me at the University of Michigan. Thank you all for your support and for sharing not only your knowledge with me, but also a good laugh.

Most importantly, I would like to thank my parents, brothers, and sister for their support throughout my time away from home. Thank you mom and dad for letting me move to Michigan, believing in me, and for always making sure that I was doing well. I cannot thank you enough for your advice, calls, and the sacrifices that you have made for me throughout my life. I love you.

Finally, I gratefully acknowledge the funding support provided by the U.S. Department of Energy's Nuclear Energy University Program (NEUP), the University of Michigan's Rackham Merit Fellowship (RMF) Program, and the Nuclear Regulatory Commission (NRC).

Table of Contents

List of Figures

Figure

List of Tables

Table

List of Abbreviations

ATWS	Anticipated Transient Without Scram
ANL	Argonne National Laboratory
BWR	Boiling Water Reactor
CAD	Computer-Aided Design
CFD	Computational Fluid Dynamics
DFT	Discrete Fourier Transform
DI	Deionized
DMD	Dynamic Mode Decomposition
DNS	Direct Numerical Simulation
ECCS	Emergency Core Cooling System
ECMF	Experimental and Computational Multiphase Flow
GDH	Gradient-Diffusion Hypothesis
GPM	Gallons Per Minute
HiRJet	High Resolution Jet
LDV	Laser Doppler Velocimetry
LES	Large Eddy Simulation
LIF	Laser-Induced Fluorescence
LOCA	Loss Of Coolant Accident
LWR	Light-Water Reactor
MSLB	Main Steam Line Break
NGNP	Next Generation Nuclear Plant
NSTF	Natural Convection Shutdown Heat Removal Test Facility
PIV	Particle Image Velocimetry
POD	Proper Orthogonal Decomposition
PSD	Power Spectral Density
PWR	Pressurized Water Reactor
RANS	Reynolds-Averaged Navier-Stokes

RCCS	Reactor Cavity Cooling System
RPV	Reactor Pressure Vessel
SLCS	Standby Liquid Control System
SPIV	Stereo Particle Image Velocimetry
SPOD	Spectral Proper Orthogonal Decomposition
TKE	Turbulent Kinetic Energy
VHTR	Very High Temperature Reactor
WMS	Wire-Mesh Sensor

Abstract

A thorough understanding of fluid dynamics is essential to predict the performance of systems in a wide range of engineering disciplines. In nuclear engineering, fluid dynamics and heat transfer play a crucial role in efficiently and safely removing heat from the nuclear reactor core to produce electricity from thermal energy. Moreover, new designs of nuclear power plants have incorporated passive safety features and passive cooling systems to provide adequate heat removal from the reactor core without the intervention of an operator or the need of external power. These passive systems rely on fluid-dynamic phenomena, such as natural circulation, for their operation. An accurate prediction of such phenomena is important to assess the performance of these systems and ensure that the core cooling is adequate during all accident scenarios.

Typically, safety systems of nuclear power plants are assessed using so-called best-estimate thermal-hydraulic system codes. These models are based on 1D formulations of mass, momentum, and energy balance and cannot correctly capture the three-dimensionality of buoyant flows and other fluid-dynamic phenomena relevant for passive safety systems. In recent years, because of the increased computational resources, Computational Fluid Dynamics (CFD) is taking a growing role in the assessment of operational and safety features of nuclear power plants. To model turbulence, Reynolds-Averaged Navier-Stokes (RANS) formulations are commonly used due to their low computational cost and robustness; however, experimental data is needed to address some shortcomings of these models.

The primary goal of this thesis is to develop a high-resolution high-fidelity experimental database for the development and improvement of CFD codes, and to gain physical insight into complex phenomena relevant for nuclear power applications. These phenomena include the propagation of stratified fronts and the mixing/interaction of multiple jets in a plenum. These phenomena are relevant for several reactor designs. To achieve this goal, the High Resolution

Jet (HiRJet) and the Reactor Cavity Cooling System (RCCS) experimental facilities were built and equipped with Laser Doppler Velocimetry (LDV) and Particle Image Velocimetry (PIV) systems to obtain velocity fields, and Wire-Mesh Sensor (WMS) units to obtain scalar fields (e.g., concentration, density). Both measurement techniques allow for high-resolution experiments in space and time necessary for the validation and advancement of CFD models. The boundary conditions were also monitored with this advanced instrumentation, making these data adequate for CFD validation. Additionally, these measurements incorporate uncertainties due to geometries, image post-processing algorithms, and the measurements' reproducibility and repeatability.

PIV data obtained in the RCCS facility were utilized to study the interaction between multiple rectangular jets. Through time averages and modal decomposition analyses, dominant frequencies and the coherent structures associated with these frequencies were discerned. These structures were determined to be independent of Reynolds numbers. Furthermore, these data exhibited significant differences between separate PIV measurements. It was observed that uncertainty bands that do not consider changes in the measurement conditions and human effects do not always capture these large variations. Through comparisons between experimental data and RANS simulations, under- and over- production of the Reynolds stresses, along with their consequent effects on the velocity profiles, were identified. Furthermore, WMS data obtained in the HiRJet facility were obtained to investigate the propagation of stratified fronts in the presence of positive and negative density gradients. These data were also used to assess the predictive capabilities of RANS simulations. Through these experiments, it was determined that depending on the sign of the density gradient, the simulations over- or under-predicted the extensions of the mixing regions and the speed of the density front propagation. These differences were attributed to an excess of Turbulent Kinetic Energy (TKE) when lighter fluid is injected, and due to a lack of TKE when the denser fluid is injected. Lastly, an experimental technique based on the synchronized use of a WMS and a PIV system was developed to measure the correlation between local concentration and velocity fluctuations (turbulent scalar fluxes).

Chapter 1

Introduction

The goal of this thesis is to gain physical insight into selected fluid-dynamics phenomena relevant to nuclear power plants and to generate a high-resolution high-fidelity experimental database for the validation and further advancement of Computational Fluid Dynamics (CFD) models relevant to nuclear engineering applications. In this chapter, we discuss the motivation for the work in this thesis, and provide a brief theoretical background as the basis for the analyses presented herein.

1.1 Motivation

Nuclear energy is responsible for generating about 20% of the United States' electricity consumption [1]. As of 2019, this electricity is generated by 98 nuclear Light-Water Reactors (LWRs) through a process known as fission (the splitting of an atom). While several types of nuclear reactors exist, only Boiling Water Reactors (BWRs) and Pressurized Water Reactors (PWRs) are in commercial operation in the United States. The BWR and PWR designs utilize water as a moderator (to slow down neutrons for fission reactions to occur) and as a coolant (to remove heat from the reactor core to generate electricity). Nuclear reactor cooling and passive safety systems rely on fluid flow to adequately remove heat from the reactor core and control the reactor's power output during normal operations and accident situations. Therefore, a good understanding of heat transfer and fluid-dynamic mechanisms (including mixing) is imperative for determining the behavior and performance of these systems.

Natural circulation, thermal stratification, and the mixing of a single and/or multiple jets with

the surrounding environment are examples of phenomena which are relevant to several systems in LWRs and non-LWRs. In LWRs, these flow conditions dictate the transient behavior of accident scenarios, including, but not limited to, Anticipated Transient Without Scram (ATWS)[1] in BWRs, and boron dilution and Main Steam Line Breaks (MSLBs) in PWRs. In non-LWRs, such as Very High Temperature Reactors (VHTRs) these phenomena determine the performance of passive safety systems such as the Reactor Cavity Cooling System (RCCS). In sodium-cooled pool-type reactors, for example, the formation and propagation of stratified fronts in the pool upper region will determine the rate of heat transfer to the secondary loop, and the magnitude of natural circulation flow in the core, following a loss of flow event.

The most common types of reactors in the world are BWRs and PWRs. A BWR has one primary circuit (typically organized into four individual loops) pressurized to approximately 7.2 MPa, which allows the coolant to boil in the Reactor Pressure Vessel (RPV) at about 286°C. A PWR instead has a primary circuit and a secondary circuit (also, typically organized into four individual loops). In the primary circuit, the coolant is maintained at about 15.5 MPa at approximately 332°C to prevent boiling in the RPV [2]. The primary and secondary circuits are thermally connected through a steam generator (i.e., a heat exchanger) where water at about 7 MPa is converted into steam. In both types of reactors, the steam is then transferred to a turbine generator to produce electricity. Simplified schematics of a BWR and a PWR are shown in Figure 1.1.

To illustrate the importance of the prediction of flow phenomena such as natural circulation, stratification, and mixing, a few scenarios are described. In nuclear reactors, control rods are used to control the fission rate and, thereby, the power output. In the event of an accident, the control rods are fully inserted to stop further fissions. In addition to the use of control rods, borated water and so-called burnable poisons within the fuel are employed in PWRs to control the excess of reactivity and keep criticality[2] throughout the fuel cycle. In order to adequately design the safety systems so that the integrity of the nuclear fuel can be maintained during accident

[1] A hypothetical worst case accident where the emergency shutdown system, through the use of control rods, fails to work [1].

[2] The normal operating condition of a nuclear reactor in which a nuclear chain reaction can be sustained [1].

(a)

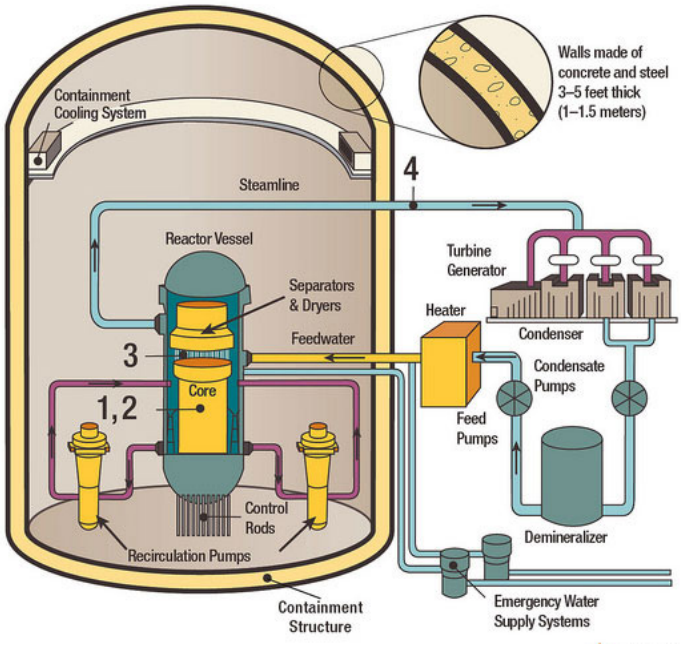

(b)

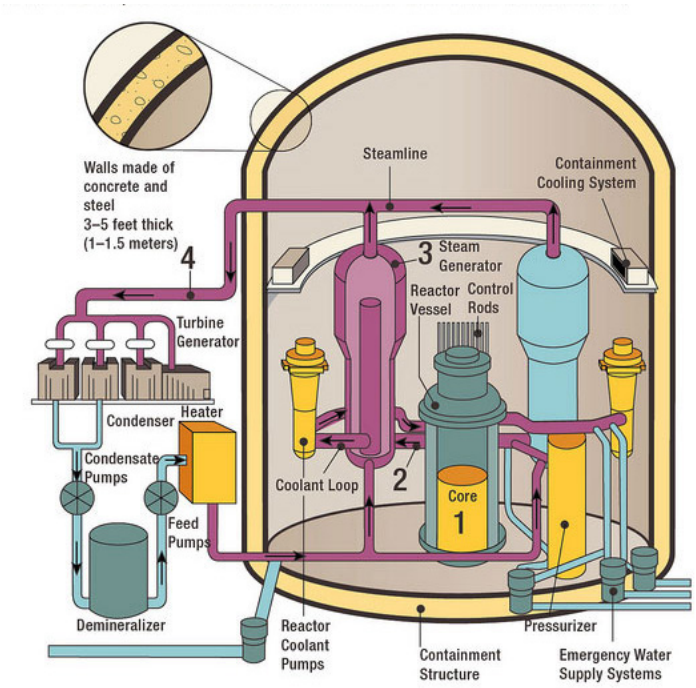

Figure 1.1: Schematics of two types of nuclear power plants: a) BWR; b) PWR. Reprinted from [1].

conditions, several postulated accident scenarios are considered during the design process of the cooling safety systems. One such postulated event is boron dilution following a small-break Loss

Of Coolant Accident (LOCA)[3] in a PWR. In the event of a small-break LOCA, the Emergency Core Cooling System (ECCS) is actuated. In the event of a malfunction of this system, the ECCS injection might stop, leading to boiling in the core. Once a stratified flow forms in the cold and hot legs of the primary circuit, steam will condensate on the primary side of the steam generator, leading to the build up of deborated water in the primary circuit (in the "cold leg"). A simplified illustration of this event is shown in Figure 1.2. Should this deborated water enter the core due to establishment of natural circulation or through restart of the main recirculation pump (forced circulation), the deborated water would lead to an undesired insertion of reactivity in the core (a safety concern) even though all of the control rods have been inserted to shutdown the reactor [3–5]. To correctly capture the plant behavior during such a scenario, an accurate prediction of the distribution of deborated water in the core is of importance.

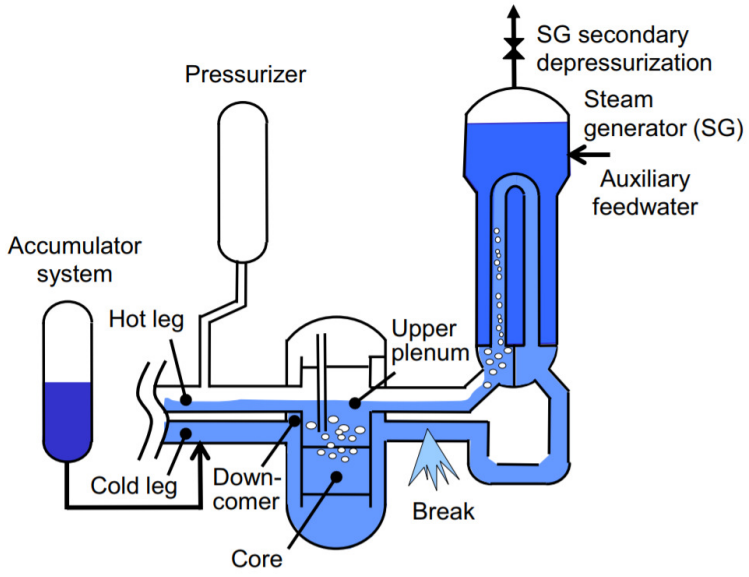

Figure 1.2: Illustration of a small-break LOCA in a PWR. Reprinted from [9].

In a MSLB in PWR, it is postulated that the main steam-line of one of the secondary loops fails. The safety concern in this case is also a possible return to criticality and high local power peaking which could result in core damage [6–8]. Because of the large pressure difference between the affected secondary loop and the containment, a MSLB event would result in flashing

[3] An accident that leads to loss of reactor coolant, due to pipe failures in the primary loop, and which could result in reactor core damage if safety systems are not properly designed [1].

of the secondary coolant present in the steam generator of the affected loop, with a consequent increase in the heat transfer between primary and secondary coolant in the affected loop. The increased heat removal from the primary circuit in the affected loop yields considerably lower primary coolant temperatures [6] at the inlet of the RPV (in the "cold leg"). The temperature at the inlet of the core, and therefore, the corresponding reactivity insertion, will strongly depend on the mixing between the coolant coming from the unaffected loops with the colder coolant coming from the affected loop, and on the degree of stratification of the colder fluid in the RPV lower plenum.

Stratification is also important in BWR safety systems. Certain BWRs are equipped with a Standby Liquid Control System (SLCS), a safety system which is designed to operate during a ATWS scenario to shutdown the reactor without the use of control rods. During ATWS, a boron solution is injected into the lower plenum of the reactor vessel of a BWR through SLCS lines, as depicted in Figure 1.3. However, because the temperature of the injected fluid is lower than that of the fluid present in the lower plenum, stratified layers might appear depending on the SLCS flow rate [10, 11], yielding insufficient mixing and delays for the boron solution to shutdown the reactor during an ATWS scenario.

Furthermore, a system where the mixing of multiple jets and thermal stratification is of interest is the RCCS upper plenum of VHTRs. A Computer-Aided Design (CAD) of the air-cooled RCCS is shown in Figure 1.4. The RCCS is a key safety system for the Next Generation Nuclear Plants (NGNPs) gas-cooled thermal reactors, and is designed to passively transfer core decay heat to the environment during accident situations. In this system, heat from the hot walls of the RPV is transferred through radiation and convection to the RCCS pipes surrounding the RPV. In the RCCS pipes, the flow is induced by natural circulation. The RCCS pipes then join together in an upper plenum where the mixing of multiple rectangular jets (of varying temperatures) occurs. One postulated issue with this system is the formation of a thermal stratification (created from the jet flows of different temperatures) that may inhibit natural circulation in the RCCS pipes, and therefore, hamper the RCCS's performance.

(a)

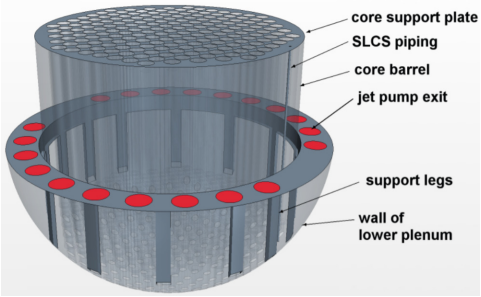

(b)

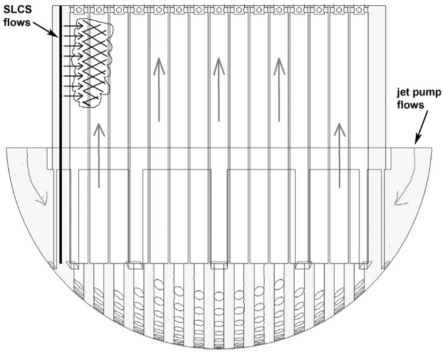

(c)

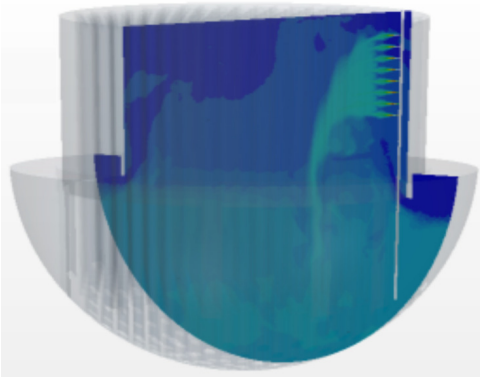

(d)

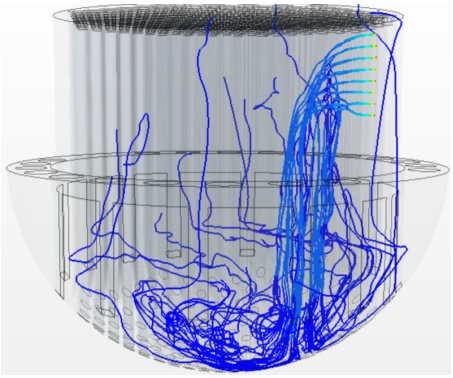

Figure 1.3: Illustration of a BWR SLCS system during a ATWS scenario: a) CAD of BWR lower plenum; b) Flow path in the lower plenum; c) SLCS injection concentration field; d) Streamlines from the SLCS jets. Reprinted from [10, 11].

The aforementioned list of postulated scenarios in LWRs and non-LWRs includes just a few examples to demonstrate the importance of accurate predictions of flow stratification, mixing, and transport of scalars (boron concentration or temperature) in various power plant components in order to capture, with an adequate degree of confidence, the safety system responses of the plant to accident situations.

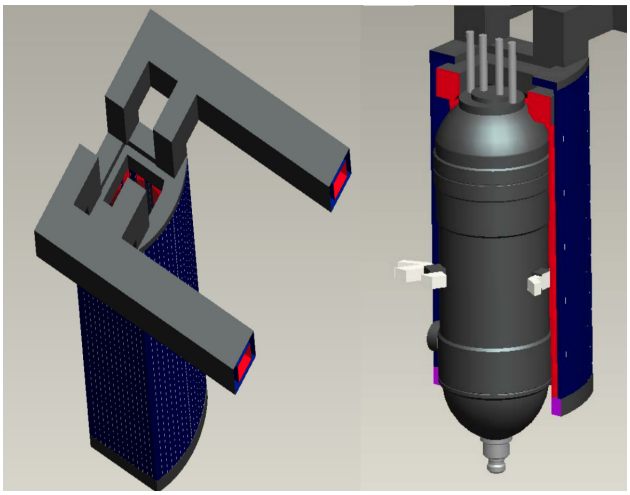

Figure 1.4: CAD of the air-cooled RCCS. The risers are in red and the downcomer in blue. Reprinted from [12].

1.2 Background

Momentum- and buoyancy-driven flows are relevant for determining the behavior of nuclear power plants during normal operation, operational transients, and accident conditions. Under normal operation conditions, momentum-driven flows induced by the main recirculation pumps circulate the primary coolant to remove heat from the reactor core, which is then converted into electricity.

Buoyancy-driven flows are present during normal operations (e.g., the secondary flow in steam generators in PWRs is established without the need of a circulation pump), and can also be established in the RPV during accident conditions. Buoyancy-driven flows are at the basis of the operation of several passive safety systems. However, in the presence of density gradients (due to temperature differences), density stratification may occur, which could negatively affect the capability of passive safety systems to remove heat, or could impact the core flow conditions in accident scenarios, as described in the previous section. Therefore, the accurate prediction of the rate of mixing of two or more flow streams (i.e., the same fluid at different temperatures) is essential to understand the power plant behavior under accident conditions. With a better prediction of the flow conditions, adequate safety margins can be chosen when designing safety systems.

During normal operations, nuclear reactor systems exhibit turbulent flow conditions. Turbu-

lence is characterized by an increased rate of mass, momentum, energy transport with respect to laminar flow conditions, and therefore, yields enhanced mixing. Analytical solutions to turbulent flows are not available; instead, several modeling approaches have been developed to predict turbulent flows through CFD. Reynolds-Averaged Navier-Stokes (RANS) turbulence models are commonly used to model turbulent flows due to their robustness and their relatively low computational cost in comparison to higher fidelity models such as Large Eddy Simulation (LES). RANS models require closure relationships for the Reynolds stresses and turbulent scalar fluxes. The Reynolds stresses (six individual components in a three-dimensional space) are given by the correlation of two fluctuating velocity components, while the turbulent fluxes (three individual components) are given by the correlation of a fluctuating velocity component and a scalar quantity (i.e., temperature, density, etc.). More details about the mathematical representation of these quantities will be given in the next section.

RANS models have been found to under- or over-estimate several mean flow quantities (e.g., velocity, temperature, densities, etc.) under constant and varying density conditions [13–20]. This can lead to inaccurate predictions of the turbulent kinetic energy distribution in the system, and consequently on the rate of fluid mixing and heat transfer [16–18, 21–24]. Additionally, based on separate observations, RANS models have been found to over-estimate thermal stratification and under-estimate turbulent mixing when buoyancy effects are present [25, 26].

Over the past decades, there has been an increase of interest for CFD simulations in the nuclear field due to the growing increase of computational resources and the increased maturity of turbulence models and CFD codes [27]. Consequently, there is a demand for high-fidelity CFD-grade experiments (i.e., experiments with high temporal and spatial resolution) for the validation and development of CFD models. With the advances in high-resolution instrumentation, there has been an increase in the number of published articles with experimental data aimed at CFD validation; however, the sources of uncertainties are often overlooked, and are not always provided. In addition to the sources of uncertainty associated to the algorithms used for post-processing of the raw data, experimental results inherit uncertainties from variations in the

geometries (e.g., instrumentation alignment and measurement probe locations), equipment, and the ability to replicate the measurement conditions between experiments.

The experimental data presented in this thesis was obtained in two facilities: one built to study the interaction of multiple jets under constant density conditions, and another to investigate the influence of buoyancy forces on the propagation and extension of stratified fronts in the presence of positive and negative density gradients. These data were used to gain physical insight, validate current CFD models, and understand the reasons for the inaccuracy of current turbulence models. Furthermore, several efforts in the present research work have been dedicated to the characterization of the measurements' uncertainties. The experiments presented in this work are characterized by well-defined, measured boundary conditions, and the measurements' uncertainties have been well characterized, resulting in a high-fidelity, CFD-grade database that can be used for the development and validation of Reynolds stresses and turbulent scalar fluxes models.

1.2.1 The Governing Equations of Fluid Motion

The Navier-Stokes equations, combined with mass and energy equations, constitutes the governing equations for viscous fluids. Derived in analogy to Newton's second law of motion[4], the Navier-Stokes equation represents the conservation of momentum of a fluid element. In Einstein notation, the Navier-Stokes equation is given by:

$$\underbrace{\frac{\partial(\rho u_i)}{\partial t} + \frac{\partial(\rho u_i u_j)}{\partial x_j}}_{1} = \underbrace{-\frac{\partial p}{\partial x_i}}_{2} + \underbrace{\frac{\partial \tau_{ij}}{\partial x_j}}_{3} + \underbrace{\rho f_i}_{4} . \tag{1.1}$$

Here, x represents the space variable, t time, ρ the density of the fluid, u_i the velocity component in the ith direction, p the pressure, μ the dynamic molecular viscosity, and f_i are the components of the body forces per unit mass (e.g., gravitational forces, electromagnetic forces, etc.) in the ith direction. The terms in Equation 1.1 correspond to the inertial forces[5] (1), the pressure forces

[4]With the assumption that stresses experienced by the fluids are caused by a diffusing viscous term (due to velocity gradients), and a pressure term.

[5]Forces due to the momentum of the fluid.

(2), the viscous forces (3), and the body forces applied to the working fluid (4). Equation 1.1 is a non-linear partial differential equation, and this non-linearity is the source for turbulence, which causes chaotic solutions that are very sensitive to initial conditions. Turbulent flows are characterized by a wide range of length and time scales which increases with larger Reynolds number $Re = \dfrac{\rho V_0 L}{\mu}$, where V_0 is the nominal velocity, and L a characteristic length (i.e., jet hydraulic diameter). Furthermore, the Navier-Stokes equation is solved in conjunction with the continuity equation, a statement of conservation of mass given by:

$$\frac{\partial \rho}{\partial t} + \frac{\partial (\rho u_j)}{\partial x_j} = 0. \tag{1.2}$$

The transport of scalar quantities is dictated by the scalar transport equation. Equation 1.3 provides the means to describe the mixing of contaminant species as it is transported by fluid motion. The conservation equation of a scalar quantity is given by:

$$\frac{\partial (\rho \phi)}{\partial t} + \underbrace{\frac{\partial (\rho \phi u_j)}{\partial x_j}}_{1} = \underbrace{\frac{\partial}{\partial x_j}\left(\rho \Gamma \frac{\partial \phi}{\partial x_j}\right)}_{2}. \tag{1.3}$$

Here, ϕ is the scalar quantity being transported (e.g. boron concentration in water), and Γ is the corresponding diffusion coefficient. If ϕ represents the fluid temperature, the diffusion coefficient would be the thermal diffusivity α. Similarly, if ϕ represents the concentration of a species, the diffusion coefficient would be the mass diffusivity D. The terms in Equation 1.3 represents the transport of the scalar quantity by fluid motion (1) and transport of the scalar by diffusion (2). While the scalar transport equation is linear, ϕ is advected by the turbulent fluid motion, which enhances its rate of mixing/transport.

1.2.2 Description of Turbulent Flows

1.2.2.1 Averages

To address the non-linearity of the Navier-Stokes equation, a statistical description of turbulent flows is often followed. In probabilistic terms, the mean behavior of an unsteady quantity can be calculated by averaging a large number of independent realizations/experiments [28, 29]. For a time varying function $f(\boldsymbol{x}, t)$ its ensemble average is expressed as

$$F(\boldsymbol{x}, t) = \lim_{M \to \infty} \frac{1}{M} \sum_{k=1}^{M} f^k(\boldsymbol{x}, t), \tag{1.4}$$

where $F(\boldsymbol{x}, t)$ is the ensemble average, M is the total number or measurements, and k is the index of the kth measurement. An illustration of different realizations (k_1, k_2, k_3) of a variable $f(x_0, t)$ and its ensemble average is shown in Figure 1.5.

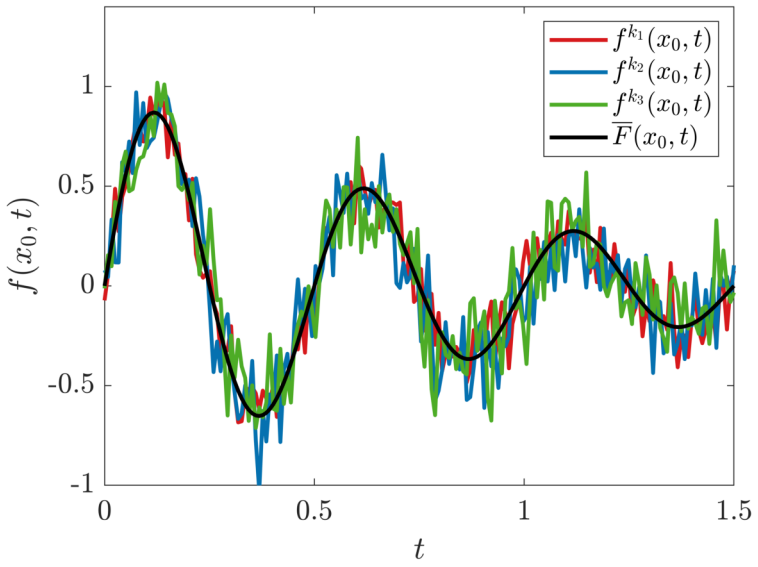

Figure 1.5: Illustration of an ensemble average.

Based on the idea of ensemble averages, an instantaneous variable $f(\boldsymbol{x}, t)$ can be separated into its mean and its fluctuating component:

$$f(\boldsymbol{x},t) = F(\boldsymbol{x},t) + f'(\boldsymbol{x},t), \tag{1.5}$$

where $F(\boldsymbol{x},t)$ is the averaged/mean component and $f'(\boldsymbol{x},t)$ is the instantaneous fluctuating component[6]. Equation 1.5 is often referred to as Reynolds decomposition/averaging.

In statistically steady/stationary (i.e., the statistics do not vary with time) turbulent flows, the mean flow variable can be considered a result of time averaging. Time-averaging for a instantaneous flow variable $f(\boldsymbol{x},t)$ is defined as

$$F(\boldsymbol{x}) = \lim_{T\to\infty} \frac{1}{T} \int_{t_0}^{t_0+T} f(\boldsymbol{x},t')dt'. \tag{1.6}$$

Here, $F(\boldsymbol{x})$ is the time-averaged field and T is the period over which the averaging takes place. For discrete measurements with constant sampling frequency in time, Equation 1.6 can be expressed in discrete form as

$$F(\boldsymbol{x}) = \frac{1}{M} \sum_{k=1}^{M} f(\boldsymbol{x},t_k). \tag{1.7}$$

1.2.2.2 Correlations

Correlations are a measure of how two signals change in relation to each other and provide the means to identify coherent structures in the flow [28–31]. Mathematically, the correlation function of a random variable $\alpha(\boldsymbol{x},t)$ with the random variable $\beta(\boldsymbol{x}+\boldsymbol{r},t+\tau)$ is given by:

$$R_{\alpha\beta}(\boldsymbol{x},\boldsymbol{x}+\boldsymbol{r},\tau) = \overline{\alpha(\boldsymbol{x},t)\beta(\boldsymbol{x}+\boldsymbol{r},t+\tau)}, \tag{1.8}$$

where $\boldsymbol{r}$ is the distance between two points in the flow domain, and τ is the time shift between the two signals (also known as time lag). For statistically stationary flows, the $\overline{(\cdot)}$ notation indicates time-averaging. Furthermore, if α and β are measured at the same location in space (i.e, $\boldsymbol{r}=0$),

[6]The lower case variables will be used for the instantaneous time evolving components, the upper case variables for the averaged components, and the lower case variables with an apostrophe for the instantaneous fluctuating components.

this function takes the following form:

$$\begin{aligned} R_{\alpha\beta}(\boldsymbol{x}, \boldsymbol{x}, \tau) &= \overline{\alpha(\boldsymbol{x}, t)\beta(\boldsymbol{x}, t+\tau)} \\ &= \overline{\alpha(t)\beta(t+\tau)} \\ &= R_{\alpha\beta}(\tau) \\ &= \frac{1}{M-1}\sum_{k=1}^{M}\alpha(t_k)\beta(t_k+\tau). \end{aligned} \tag{1.9}$$

For the cases where $\alpha \neq \beta$ and $\alpha = \beta$, this function is referred to as the cross-correlation and auto-correlation function, respectively. Furthermore, when the stochastic variables α and β correspond to the velocity fluctuations $u_i'(t)$ and $u_j'(t)$, the one-point correlations at $\tau = 0$ are known as the Reynolds stresses or momentum fluxes (described in Section 1.2.3.1):

$$\begin{aligned} R_{u_i'u_j'}(\tau = 0) &= \overline{u_i'(t)u_j'(t)} \\ &= \frac{1}{M-1}\sum_{k=1}^{M}u_i'(t_k)u_j'(t_k). \end{aligned} \tag{1.10}$$

Often times, the correlation function (Equation 1.9) is normalized by the variances of the stochastic variables to obtain a better interpretation of how well the two variables are correlated. This gives rise to the correlation coefficient $\rho(\tau)$ defined as

$$\rho_{\alpha\beta}(\tau) = \frac{\overline{\alpha(t)\beta(t+\tau)}}{\sqrt{\overline{\alpha^2(t)}}\sqrt{\overline{\beta^2(t+\tau)}}}. \tag{1.11}$$

This correlation coefficient has a domain between $-1 \leq \rho_{\alpha\beta} \leq 1$. A value of $\rho_{\alpha\beta} = -1$ indicates perfect anti-correlation, $\rho_{\alpha\beta} = 0$ no correlation, and $\rho_{\alpha\beta} = 1$ perfect correlation (i.e., $\alpha = \beta$). For discrete measurements with constant acquisition rates, the correlation can be expressed as

$$\rho_{\alpha\beta}(\tau) = \frac{\sum_{k=1}^{M}\alpha(t_k)\beta(t_k+\tau)}{\sqrt{\sum_{k=1}^{M}\alpha^2(t_k)}\sqrt{\sum_{k=1}^{M}\beta^2(t_k+\tau)}}. \tag{1.12}$$

Another useful form of the correlation coefficient function is obtained by writing Equation 1.11 as a function of a reference location $\boldsymbol{x}$ and a spatial separation $\boldsymbol{r}$. This form is referred to as the two-point correlation coefficient function, and is used to describe the spatial distance over which the stochastic variables are correlated. Based on the magnitude of the correlation from Equation 1.13, spatial structures/patterns of the turbulent flow fields can be discerned

$$\begin{aligned}\rho_{\alpha\beta}(\boldsymbol{x}, \boldsymbol{x}+\boldsymbol{r}) &= \frac{\overline{\alpha(\boldsymbol{x},t)\beta(\boldsymbol{x}+\boldsymbol{r},t)}}{\sqrt{\overline{\alpha^2(\boldsymbol{x},t)}}\sqrt{\overline{\beta^2(\boldsymbol{x}+\boldsymbol{r},t)}}}, \\ &= \frac{\sum_{k=1}^{M}\alpha(\boldsymbol{x},t_k)\beta(\boldsymbol{x}+\boldsymbol{r},t_k)}{\sqrt{\sum_{k=1}^{M}\alpha^2(\boldsymbol{x},t_k)}\sqrt{\sum_{k=1}^{M}\beta^2(\boldsymbol{x}+\boldsymbol{r},t_k)}}.\end{aligned} \tag{1.13}$$

1.2.2.3 Power Spectral Density Estimates

Moments of the instantaneous fields provide a description of the mean flow behavior. To characterize the time dynamics, several spectral/frequency analysis tools can be used. Dominant frequencies, which indicate periodicities in signals, can be identified through Power Spectral Density (PSD) analysis of the time-series of flow variables. For a time-series $\alpha(t)$, its PSD function $S_{\alpha\alpha}(f)$ is defined as the Fourier transform of its autocorrelation function $R_{\alpha\alpha}(\tau)$ and is given by:

$$S_{\alpha\alpha}(f) = \int_{-\infty}^{\infty} R_{\alpha\alpha}(\tau)e^{-2\pi i f\tau}d\tau, \tag{1.14}$$

where f is the signal frequency and $R_{\alpha\alpha}(\tau)$ is defined in Equation 1.9. While several PSD estimate techniques exist, Welch's method [32] was employed for the analysis in this thesis. This method reduces the noise in the frequency spectrum (in exchange of loss of frequency resolution) and provides convergent estimates of the power spectral densities. Here, we provide a short outline of the method. Consider a single flow variable $q(\boldsymbol{x}, t)$ which consists of a data set of M equally spaced time instances, and let $q_{\boldsymbol{x}_0} \in \mathbb{R}^{1\times M}$ represent the time series of the flow variable $q(\boldsymbol{x}_0, t)$

at a given location $\boldsymbol{x}_0$

$$q_{\boldsymbol{x}_0} = [q(\boldsymbol{x}_0, t_1), q(\boldsymbol{x}_0, t_2), ..., q(\boldsymbol{x}_0, t_M)] \in \mathbb{R}^{1\times M}. \tag{1.15}$$

To employ Welch's method, the time series is first divided into N_b successive overlapping blocks/segments with N_f instances of the variable:

$$q^{(n)}_{\boldsymbol{x}_0} = [q^{(n)}_{\boldsymbol{x}_0,1}, q^{(n)}_{\boldsymbol{x}_0,2}, ..., q^{(n)}_{\boldsymbol{x}_0,N_f}] \in \mathbb{R}^{1\times N_f}, \tag{1.16}$$

where $n = 1, ..., N_b$ is the overlapping block number. Next, the Discrete Fourier Transform (DFT) of the windowed[7] overlapping blocks are calculated:

$$\hat{q}^{(n)}_{\boldsymbol{x}_0} = [\hat{q}^{(n)}_{\boldsymbol{x}_0,1}, \hat{q}^{(n)}_{\boldsymbol{x}_0,2}, ..., \hat{q}^{(n)}_{\boldsymbol{x}_0,N_f}] \in \mathbb{R}^{1\times N_f}, \tag{1.17}$$

to obtain periodograms $\hat{P}^{(n)}_{\boldsymbol{x}_0}$ for each overlapping block of length N_f:

$$\hat{P}^{(n)}_{\boldsymbol{x}_0} = \frac{1}{N_f}\left|\hat{q}^{(n)}_{\boldsymbol{x}_0}\right|^2 \in \mathbb{R}^{1\times N_f}. \tag{1.18}$$

These periodograms are then averaged to obtain the PSD estimate

$$\hat{S}_{\boldsymbol{x}_0} = \frac{1}{N_b}\sum_{n=0}^{N_b-1} \hat{P}^{(n)}_{\boldsymbol{x}_0} \in \mathbb{R}^{1\times N_f}. \tag{1.19}$$

1.2.2.4 Spectral Proper Orthogonal Decomposition

In addition to describing the flow fields by averages, correlations, and local PSD estimates, modal decomposition techniques can be used to discern coherent flow structures present in the flow fields. Here we provide a brief description of a few prominent modal decomposition techniques and describe the method chosen for our analyses. A comprehensive overview of several

[7] Windowing is the process of taking a small subset of a larger data set. Windowing helps reduce spectral leakage caused by the non-periodicity of the data.

mode decomposition techniques is presented in the review by Taira et al. [33]. Proper Orthogonal Decomposition (POD), introduced by Lumley [34], is one of the most commonly used modal decomposition techniques for analyzing fluid flows [33]. POD is a mathematical technique that aims to extract spatially dependent set of modes (i.e., structures); however, POD modes represent flow phenomena at several time scales, which may suppress important dynamical information about the flow fields at several frequencies. As a result, while widely used, this method is ineffective at discerning coherent flow structures that occur at different time scales. Fluid dynamic systems exhibit multiscale phenomena in both space and time, thus other techniques such as Dynamic Mode Decomposition (DMD) and Spectral Proper Orthogonal Decomposition (SPOD) are preferred over POD to extract the flow structures that evolve coherently in space and time [34, 35]. One advantage of SPOD over DMD is that it identifies energy-ranked modes each associated to a single frequency, thus enabling a more robust method to discern spatiotemporal coherent structures, making SPOD a more desirable modal decomposition tool for turbulent flows [36].

In this manuscript, we employed the SPOD algorithm developed by Towne et al. [36], which is an expansion of the technique described in Section 1.2.2.3. Here we briefly describe this algorithm. The instantaneous flow variable $\boldsymbol{q}(\boldsymbol{x}, t)$ on a spatial domain $\boldsymbol{x}$ at time t_k, can be represented as a vector $\boldsymbol{q}_k \in \mathbb{R}^N$ (known as a snapshot), where the length N of the vector is equal to the number of flow variables times the number of grid points. If M equally spaced time instances are available, the data set can be organized as

$$\boldsymbol{Q} = [\boldsymbol{q}_1, \boldsymbol{q}_2, ..., \boldsymbol{q}_M] \in \mathbb{R}^{N \times M}. \tag{1.20}$$

The cross-spectral density tensor is then estimated by means of Welch's method, where the spectra is averaged over multiple realizations of the flow. To perform this task, the data set is first divided into smaller overlapping blocks, each containing N_f number of snapshots. We can then write each block as:

$$\boldsymbol{Q}^{(n)} = [\boldsymbol{q}_1^{(n)}, \boldsymbol{q}_2^{(n)}, ..., \boldsymbol{q}_{N_f}^{(n)}] \in \mathbb{R}^{N \times N_f}, \tag{1.21}$$

where $n = 1, ..., N_b$. We then compute the DFT of each windowed block

$$\hat{\boldsymbol{Q}}^{(n)} = [\hat{\boldsymbol{q}}_1^{(n)}, \hat{\boldsymbol{q}}_2^{(n)}, ..., \hat{\boldsymbol{q}}_{N_f}^{(n)}] \in \mathbb{R}^{N \times N_f}. \tag{1.22}$$

Next, a new data matrix is formed by sorting the Fourier coefficients at frequencies f_k from all the blocks into a new data matrix

$$\hat{\boldsymbol{Q}}_{f_k} = [\hat{\boldsymbol{q}}_k^{(1)}, \hat{\boldsymbol{q}}_k^{(2)}, ..., \hat{\boldsymbol{q}}_k^{(N_b)}] \in \mathbb{R}^{N \times N_b} \tag{1.23}$$

which is used to obtain the estimated cross-spectral density tensor at frequency f_k:

$$\mathbf{S}_{f_k} = \hat{\boldsymbol{Q}}_{f_k} \hat{\boldsymbol{Q}}_{f_k}^*. \tag{1.24}$$

The estimated cross-spectral density tensor at frequency f_k is then written as an eigenvalue problem:

$$\mathbf{S}_{f_k} \mathbf{W} \boldsymbol{\Psi}_{f_k} = \boldsymbol{\Psi}_{f_k} \boldsymbol{\Lambda}_{f_k}, \tag{1.25}$$

where the columns of the eigenvectors $\boldsymbol{\Psi}_{f_k}$ are the SPOD modes at frequency f_k, which are ordered according to their corresponding eigenvalues $\boldsymbol{\Lambda}_{f_k}$. Thus, the eigenvector with the largest eigenvalue represents the optimal mode for the given frequency f_k. For further details, we refer the reader to the paper by Towne et al. [36].

1.2.3 Modeling Turbulent Flows

1.2.3.1 The Reynolds-Averaged Transport Equations

Turbulent flows consist of a wide spectrum of small and large turbulent eddies that fluctuate in space and time. The large scale eddies extract energy from the mean flow and this energy is then transferred from the larger eddies to the smaller eddies through an energy cascade process [37]. Eventually, at the smallest eddies scales, the kinetic energy is converted into internal energy

through viscous dissipation.

There are three main computational approaches used to predict turbulent flows: Direct Numerical Simulation (DNS), Large Eddy Simulation (LES), and Reynolds-Averaged Navier-Stokes (RANS) simulation. DNS resolves the whole turbulence spectrum (i.e., all eddies sizes) and does not require any modeling. However, the high computational cost required to resolve all turbulence scales makes this approach limited to idealized cases and low Reynolds numbers, far from flows of practical applications. LES is an approach in which the Navier-Stokes equation is spatially averaged. Through this method, the energy containing eddies (large scales) are resolved and the small scales (responsible for viscous dissipation) are modeled. However, while computationally less expensive than DNS, this method is still impractical for most large scale applications. Last but not least, RANS simulations solve the equations for the mean flow and requires modeling for all of the turbulent scales [29, 38]. This modeling approach is computationally inexpensive compared to DNS and LES, and is widely used for industrial applications. The simulation results for a turbulent jet flow by these three simulation approaches are shown in Figure 1.6 (note that DNS and LES results are transient in nature, therefore, the images in the figure correspond to one particular time snapshot, while mean flow results are computed by RANS).

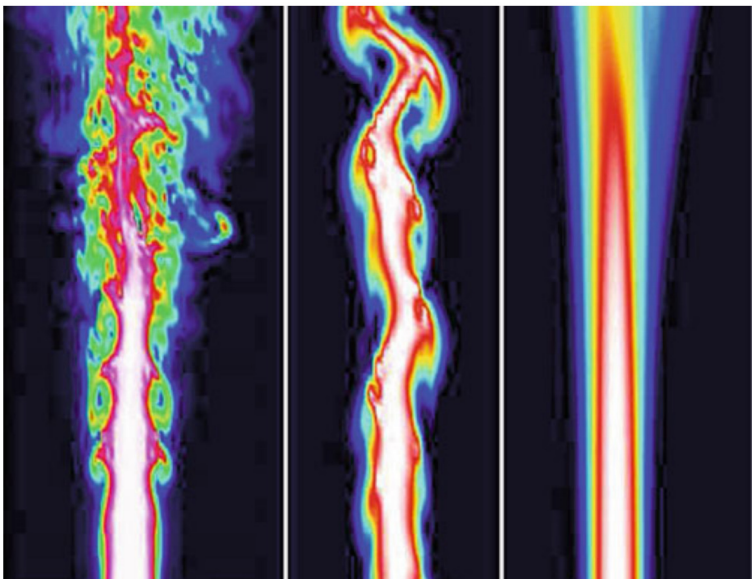

Figure 1.6: Turbulent flow simulations through DNS (left), LES (middle), and RANS (right). Reprinted from [39].

The RANS-averaged equations are derived by Reynolds-averaging (employing Equation 1.5) the governing equations of fluid motion (Equations 1.1, 1.2, 1.3), and take the following forms:

$$\frac{\partial\left(\rho U_i\right)}{\partial t}+\frac{\partial(\rho U_i U_j)}{\partial x_j}=-\frac{\partial P}{\partial x_i}+\frac{\partial}{\partial x_j}\left[T_{ij}-\rho\overline{u_i^{'}u_j^{'}}\right], \tag{1.26}$$

$$\frac{\partial\rho}{\partial t}+\frac{\partial\left(\rho U_j\right)}{\partial x_j}=0. \tag{1.27}$$

Equations 1.26 and 1.27 are referred to as the Reynolds-Averaged Navier-Stokes (RANS) and the Reynolds-averaged Continuity equation, respectively. The only difference between the Continuity equation and its Reynolds-averaged formulation is that the Reynolds-averaged equation solves for the mean velocity U_j instead of the instantaneous velocity u_j. Similarly, the RANS equation contains the mean flow quantities U_j, P, and T_{ij}; however, an additional term arises: $-\rho\overline{u_i^{'}u_j^{'}}$. This correlation of the velocity fluctuations is known as the Reynolds stresses or momentum fluxes (experimentally obtained via Equation 1.10), and is the source of turbulent transport and mixing (in simpler frameworks, modeled as an additional momentum diffusion term). The inclusion of this term makes this an underdetermined system of equations and requires the introduction of closure relations [8].

To solve the equations for the mean flow variables, the Reynolds stresses must be modeled. Over the past decades, large amounts of experimental data have been used to develop a wide range of models for the Reynolds stresses; however, additional databases are needed for the improvement of these models. One common approach to close these equations is to relate the Reynolds stresses to the mean velocity gradients. This approach is known as the Boussinesq Eddy viscosity assumption and is given by:

$$-\rho\overline{u_i^{'}u_j^{'}}=\mu_t\left(\frac{\partial U_i}{\partial x_j}+\frac{\partial U_j}{\partial x_i}\right)-\frac{2}{3}\rho k\delta_{ij}, \tag{1.28}$$

[8] This is known as the closure problem in turbulence theory.

where μ_t is the dynamic turbulent/eddy viscosity [9], δ_{ij} the Kronecker delta, and k is the turbulent kinetic energy (i.e., the mean kinetic energy per unit mass associated with eddies in turbulent flow):

$$k = \frac{1}{2}\overline{u_i' u_i'}. \tag{1.29}$$

The mean scalar fields are obtained via the Reynolds-averaged scalar transport equation:

$$\frac{\partial(\rho\Phi)}{\partial t} + \frac{\partial(\rho\Phi u_j)}{\partial x_j} = \frac{\partial}{\partial x_j}\left(\rho\Gamma\frac{\partial\Phi}{\partial x_j} - \rho\overline{u_j'\phi'}\right). \tag{1.30}$$

In this case, a new diffusive term (the source of turbulent mixing) arises by Reynolds-averaging the scalar equation. This $-\rho\overline{u_j'\phi'}$ term is referred to as the turbulent scalar fluxes and is commonly modeled by employing the Gradient-Diffusion Hypothesis (GDH) [10]

$$-\rho\overline{u_j'\phi'} = \rho\Gamma_t\frac{\partial\Phi}{\partial x_j}, \tag{1.31}$$

in which the scalar fluxes are assumed to be proportional the gradient of the mean scalar field by means of a turbulent diffusion coefficient Γ_t. In Chapters 3 and 4 we discuss the shortcomings of the current models for the Reynolds stresses and turbulent scalar fluxes. Currently, there is no single turbulence model that can accurately predict all turbulent flows, and most of the efforts are put into modifying the current models. To identify the deficiencies and to support the development of these models, CFD-grade experimental data were obtained in the facilities described in Chapter 2.

1.2.3.2 The $k\epsilon$ Turbulence Model

A variety of eddy viscosity models [11] can be used to solve for the eddy viscosity term μ_t in Equation 1.28; however, we utilize the $k\epsilon$ two-equation model for our simulations. The $k\epsilon$ model introduces two additional transport equations: an equation for the Turbulent Kinetic Energy

[9] μ_t is assumed to be isotropic but not homogeneous.
[10] Or a variation of this gradient-transport closure.
[11] Algebraic models, one- and multiple-equation models (which include m additional transport equations).

(TKE) k and another for the turbulence dissipation rate ϵ. Our simulations were carried out using the commercial finite volume CFD code STAR-CCM+ 12.06 (Siemens) [40]. The $k\epsilon$ equations implemented in STAR-CCM+ are the following:

$$\frac{\partial}{\partial t}(\rho k) + \frac{\partial}{\partial x_i}(\rho k U_i) = \frac{\partial}{\partial x_i}\left[\left(\mu + \frac{\mu_t}{\sigma_k}\right)\frac{\partial k}{\partial x_i}\right] + G_k + G_b - \rho\epsilon, \tag{1.32}$$

$$\frac{\partial}{\partial t}(\rho \epsilon) + \frac{\partial}{\partial x_i}(\rho \epsilon U_i) = \frac{\partial}{\partial x_i}\left[\left(\mu + \frac{\mu_t}{\sigma_\epsilon}\right)\frac{\partial \epsilon}{\partial x_i}\right] + \frac{\epsilon}{k}C_{\epsilon 1}\left(G_k + C_{\epsilon 3}G_b\right) - C_{\epsilon 2}f_2\rho\frac{\epsilon^2}{k}, \tag{1.33}$$

where the turbulent/eddy viscosity is calculated by $\mu_t = \rho C_\mu k^2/\epsilon$, $\sigma_k = 1.0$, $\sigma_\epsilon = 1.3$, $C_{\epsilon_1} = 1.44$, $C_{\epsilon_2} = 1.92$, f_2 is a damping function, and $C_\mu = 0.09$.

In these equations, G_k represents the TKE production due to shear, and G_b represents the production or quenching of TKE due to buoyancy forces:

$$G_k = \mu_t S^2 - \frac{2}{3}\rho k\frac{\partial U_i}{\partial x_i} - \frac{2}{3}\mu_t\left(\frac{\partial U_i}{\partial x_i}\right)^2, \tag{1.34}$$

$$G_b = \beta\frac{\mu_t}{Pr_t}\frac{\partial (T g_i)}{\partial x_i}, \tag{1.35}$$

where $S^2 = 2\boldsymbol{S}{:}\boldsymbol{S}$, the mean strain rate tensor $\boldsymbol{S} = S_{ij} = \frac{1}{2}\left(\frac{\partial U_i}{\partial x_j} + \frac{\partial U_j}{\partial x_i}\right)$, β is the coefficient of thermal expansion, and Pr_t is the turbulent Prandtl number. Furthermore, in the absence of a temperature gradient, G_b may be expressed as:

$$G_b = -\frac{1}{\rho}\frac{\mu_t}{Sc_t}\frac{\partial (\rho g_i)}{\partial x_i}, \tag{1.36}$$

where Sc_t is the turbulent Schmidt number. Based on Equation 1.36, the production or quenching of the TKE depends on the sign of the mean density gradients in the flow fields, which has strong implications on the speed of the propagation of stratified fronts as described in Chapter 4.

Chapter 2

Measurement Techniques and Experimental Facilities

In this chapter, we provide an overview of the high-resolution experimental measurement techniques and facilities used for the generation of our CFD-grade experimental database. The fluid-dynamics phenomena of interest for our investigations are a) propagation of stratified fronts and b) mixing of multiple jets in a plenum.

2.1 Particle Image Velocimetry

We use Particle Image Velocimetry (PIV) to measure instantaneous velocity vector fields. PIV is a non-intrusive optical measurement technique that was developed for flow visualization in the early 1980's [41]. PIV systems make use of a laser and appropriate optics to create a thin sheet of light. This is used to illuminate tracer particles mixed with the working fluid. These particles are very small in size (a few tenths of micrometers in diameter) and neutrally buoyant. One or more cameras are used to track the motion of these particles. In particular, the laser is used to illuminate twice, within a short period of time Δt, a selected cross-section of the experimental setup. The tracer particles within these illuminated areas are captured by a camera positioned perpendicular to the laser sheet. An illustration of a typical 2D PIV system and a pair of PIV raw images are shown in Figures 2.1 and 2.2, respectively. Once the image pairs are recorded, they are post-processed using cross-correlation techniques to obtain velocity instantaneous vector fields. Note that in a 2D PIV setup, only the two velocity components in the plane of the light sheet can be measured. If also the third velocity component (perpendicular to the light sheet) is desired, at least two cameras are needed for the image acquisitions (stereo PIV).

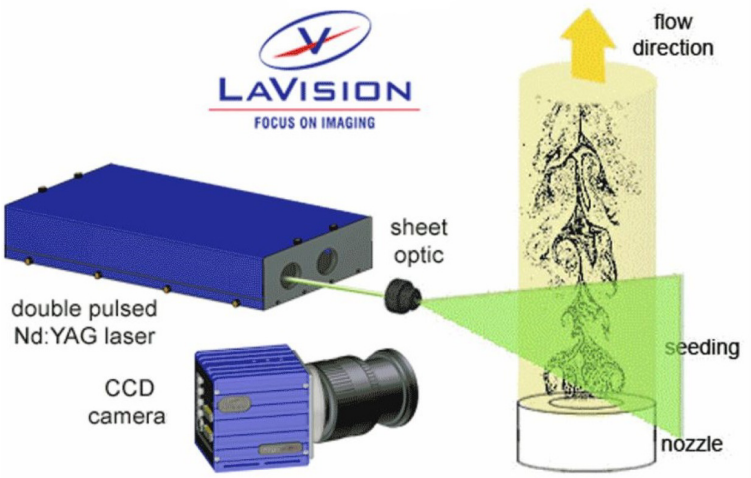

Figure 2.1: An illustration of a 2D PIV system. Reprinted from [42].

(a) (b)

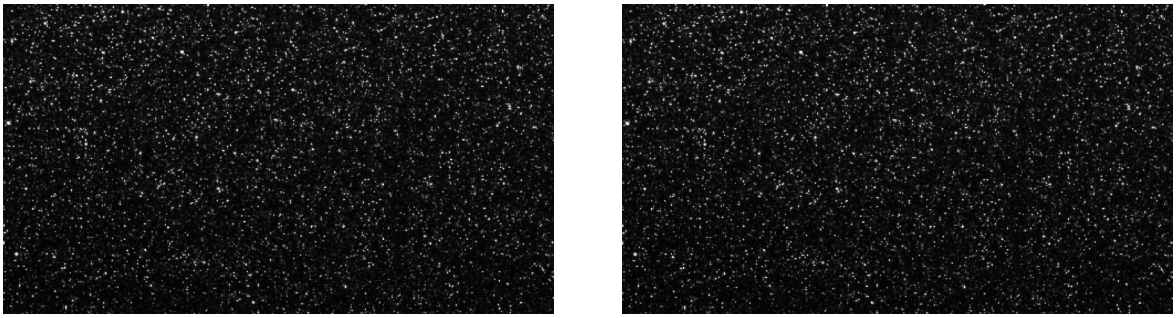

Figure 2.2: Pair of PIV images at two time steps: a) $t = t_0$; b) $t = t_0 + \Delta t$.

To efficiently post-process the PIV images, which contain a large amount of illuminated particles, the images are divided into small areas called interrogation windows. Consequently, the interrogation windows from the two images are cross-correlated (pixel by pixel) to determine the correlation peaks, and therefore, the average particle displacements $(\Delta x, \Delta y)$. Furthermore, to map the particle displacement from pixels to millimeters, and to correct for distortions in the PIV images (e.g., due to the camera's viewing angle of the measurement plane or due to the camera's optics), spatial calibrations are carried out. To do so, a calibration target (with a grid of equidistant marks) of known dimensions is used. The target is positioned such that the grid of points is illuminated by the laser sheet. To ensure that the target is placed at the same location during different measurements, we also utilize a holder/stand for the calibration target. The target and

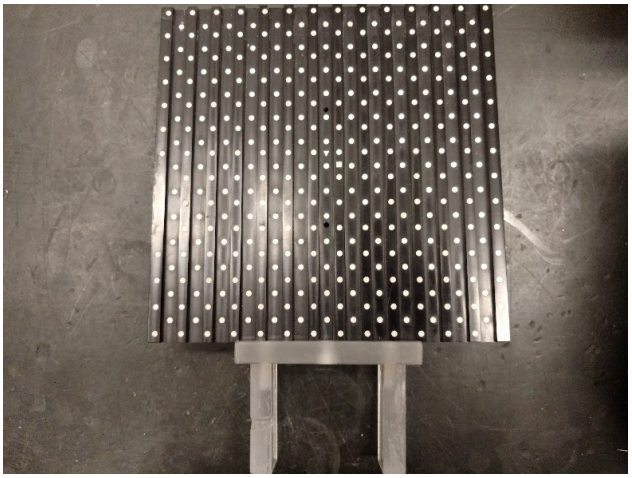

Figure 2.3: Calibration target and acrylic holder.

holder used for our PIV measurements is shown in Figure 2.3.

After obtaining the displacements, and knowing the time between images Δt, the velocity vector (u, v) for each interrogation window can be determined by:

$$u_i = \frac{\Delta x_i}{\Delta t}. \tag{2.1}$$

An illustration of this procedure is shown in Figure 2.4. For further details on the working principle of PIV, we refer the reader to [41, 43].

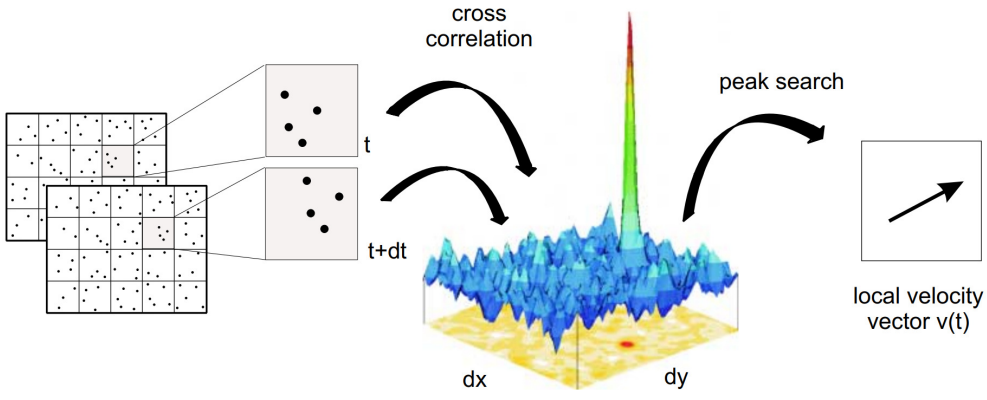

Figure 2.4: Illustration of the PIV post-processing algorithm. Reprinted from [42].

Two PIV systems have been used in the Experimental and Computational Multiphase Flow (ECMF) laboratory to carry out the experiments described in this thesis: one by LaVision GmbH

and another assembled in-house. The LaVision system includes a $527\ nm$ double-cavity, dual head Nd:YLF pulsed laser (Photonics Industries), which can operate at a maximum frequency of $10\ kHz$ and can produce $30\ mJ$ per pulse. This system uses a 4 MP CMOS camera (Phantom M340) and LaVision's high-speed controller/synchronizer model 1108075. The tracer particles used are $10\mu m$ borosilicate glass hollow spheres with a density of $1.10 \pm 0.05\ g/cm^3$. The in-house PIV system consists of a New Wave Research $532nm$ Nd:YAG pulsed laser, a 12MP CMOS camera (IO Industries) with a sensor size of $4096 \times 3072\ pixel^2$ (pixel size of $5.5 \times 5.5\ \mu m^2$), and a BNC 575 Pulse/Delay generator connected to a Core2 DVR Express (IO Industries) as a controller/synchronizer. The in-house system was specifically designed to allow for long measurements times. The Lavision system measurement time instead, is limited by the camera on-board memory. The in-house system was also coupled with UltraLasers Inc.'s $532nm$ Continuous Wave Laser (MGL-N-532A) for some of the measurements.

The LaVision's system was used for time-resolved measurements and allows the investigation of the instantaneous flow velocity fields, while the in-house system was used for long time measurements needed for statistical convergence of the time-averaged quantities (these quantities are typically needed for CFD validation). The recorded PIV images were processed using LaVision's DaVis 8.4.0 [42] using a multi-pass approach with an initial interrogation window of $64 \times 64\ pixels^2$ with 50% overlap for the first two passes, and a final interrogation of $32 \times 32\ pixels^2$, with a 75% overlap for the last three passes. Based on these settings and the locations of the PIV equipment, we were able to obtain velocity fields with spatial resolutions of $0.5 - 1.0\ mm$.

2.2 Wire-Mesh Sensor

Wire-Mesh Sensors (WMSs) were utilized to measure instantaneous density distributions in selected cross-sections of the experimental setup. These sensors consists of two planes of electrode wires rotated by 90°with respect to each other. These planes of electrodes are separated by a small axial distance. A voltage is applied to the electrodes of one of the planes (transmit-

ter plane) and the electrical current flowing through the electrodes of the second plane (receiver plane) is measured. During a measurement, the transmitter electrodes are actuated successively by a multiplex circuit, and then, the current is measured by the receiver electrodes. The current measured in each receiver electrode is a measure of the fluid conductivity within a control volume centered around the crossing point between a receiver and transmitter electrode. This current is then transformed into voltages by operational amplifiers, then sampled by individual sample/hold circuits, and stored in a computer connected to the analog to digital converters. A simplified schematic of a WMS unit and a diagram of the control signals are shown in Figures 2.5 and 2.6, respectively. In these schematics, S1-S4 are switches for the transmitter electrodes, SP the pulsed modulated driving voltage switch, ADC the analog to digital converters, and S/H are the sample/hold circuits. Here, a pulse modulated driving voltage switch is used to avoid electrolysis, which would lead to significant errors in the measurements. Furthermore, to avoid cross-talk between transmitter electrodes[1], the outputs of the transmitter drivers and the receiver inputs were designed with significantly low impedance [44].

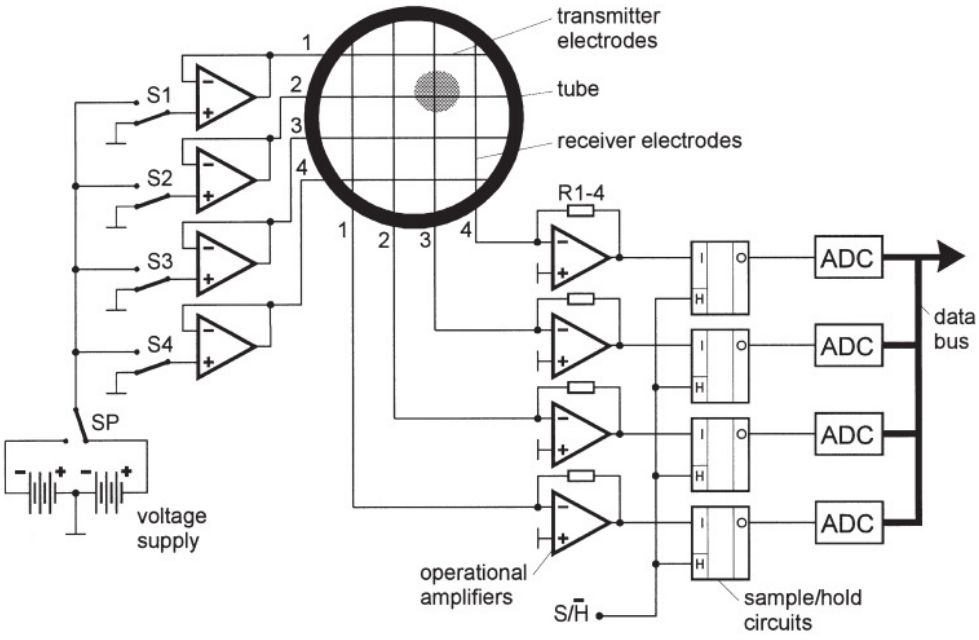

Figure 2.5: Schematic of a WMS system. Reprinted from [44].

[1]Cross-talk due to flow of the driving current from the actuated transmitter electrode to the neighboring non-actuated transmitter electrodes can cause blurring/loss of spatial resolution.

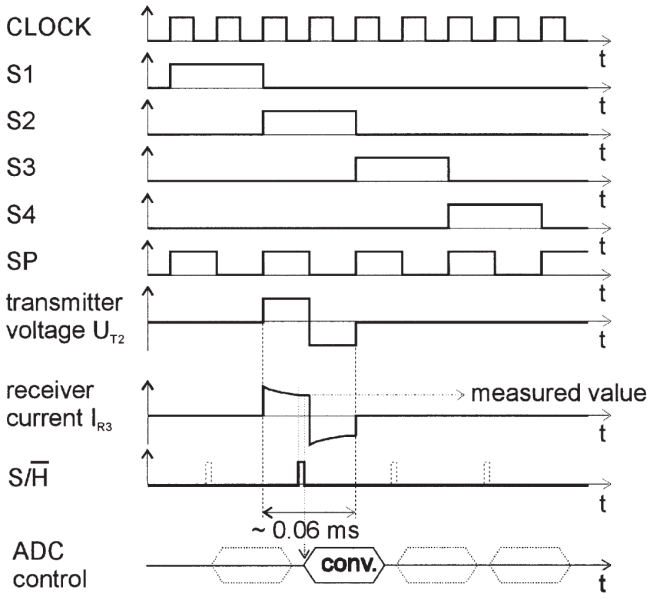

Figure 2.6: Diagram of a WMS's control signals. Reprinted from [44].

The electrical resistance induced by the fluid present in the control volume, centered around any given cross-point between a transmitter and a receiver electrode, will affect the current measured by the receiver electrode. As a result, distributions of fluids with different conductivities can be distinguished. To measure the density distributions in the cross-section where the WMS is mounted, two fluids with different electrical conductivities must be used (e.g., de-ionized water and tap water). To map the instantaneous current measurements $\rho(t)$ to a dimensionless scalar ρ^*_{Exp}, two calibration measurements are needed. With the WMS electrodes fully submerged, a calibration measurement with fluid 1 (with current readings ρ_1) and another with fluid 2 (with current reading ρ_2) is taken. With these reference measurements, ρ^*_{Exp} is calculated by:

$$\rho^*_{Exp}(t) = \frac{\rho(t) - \rho_1}{\rho_2 - \rho_1}, \tag{2.2}$$

where a value $\rho^*_{Exp} = 0$ indicates the probes are submerged in fluid 1, $\rho^*_{Exp} = 1$ submerged in fluid 2, and a value between (0,1) indicates a mixture of the two fluids. We would like to note to the reader that the measurements $\rho(t)$ exist for every control volume between the transmitter-receiver planes, and as a result, a ρ^*_{Exp} distribution of the fluid between the planes of electrodes

is obtained. If fluid 1 and fluid 2 have different densities, ρ^*_{Exp} represents the normalized density based on those two fluids.

A picture of a WMS unit is shown in Figure 2.7a. Figures 2.7b and 2.7c are pictures of two sensors that were fabricated in our lab and used in the High Resolution Jet (HiRJet) facility described in Section 2.4. For further details on the working principle of these sensors, we refer the reader to [44].

(a)

(b)

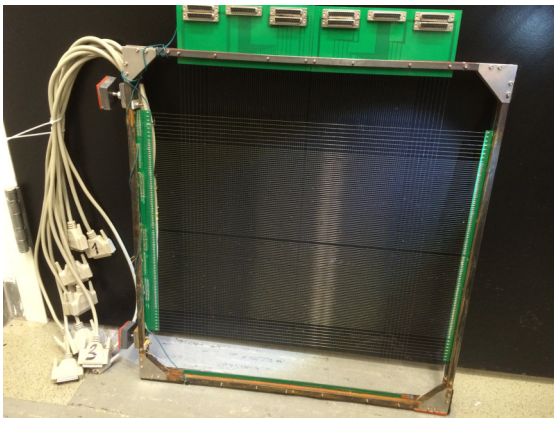

(c)

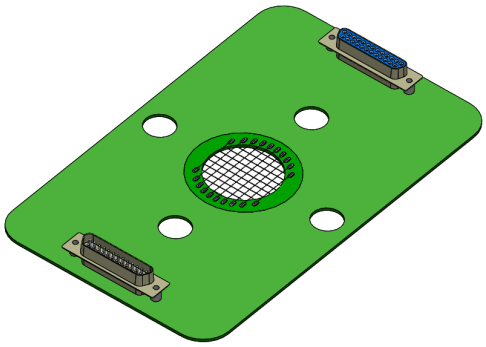

Figure 2.7: WMS equipment: a) WMS unit reprinted from [45]; b) large WMS; c) WMS designed for a circular channel.

The sensors shown in Figure 2.5, used to measure density distributions in the HiRJet facility, were connected to a WMS200 system electronic unit (HZDR Innovation GmbH). The electronic unit is capable of driving sensors with up to 128×128 measurement points (for a total of 16,384 simultaneous local conductivity measurements) with an acquisition frequency of up to 10,000 images/s. The sensors allow for a spatial resolution of up to 2 mm. The insertion of the electrodes

(stainless-steel wires with diameter of $0.1\ mm$) in the working fluid makes this an intrusive measurement technique; however, the flow perturbations induced by the wires are small and can be neglected for the range of Reynolds numbers of our experiments [46]. The WMS shown Figure 2.7b consists of 9216 measurement locations (fine grid), with a spatial resolution of $3.175\ mm$ over an area of $30.48 \times 30.48\ cm^2$. The same sensor has been designed to also be used in a coarse grid arrangement with 4096 measurement locations, corresponding to a spatial resolution of $6.35\ mm$, and covering a surface of $40.64 \times 40.64\ cm^2$. The axial distance between the two electrodes planes is $3.3\ mm$. Therefore, the fluid conductivity (and therefore density) is measured across control volumes of $3.175 \times 3.175 \times 3.3mm^3$ or $6.35 \times 6.35 \times 3.3\ mm^3$, respectively. If necessary, the distance between parallel electrode planes could be lowered to $1 - 2\ mm$. The WMS shown Figure 2.7c, is used to measure the density distribution at the inlet of the HiRJet facility, so that the boundary conditions can be well characterized. This sensor consists of a total of $10 \times 10 = 100$ measurement points distributed over a cross-section of $38 \times 38\ mm^2$. The axial distance between the electrodes planes is $1.5mm$, while the spatial resolution in the plane is of $3.8\ mm$. One of the major advantages of this sensor is that it enables us to measure the concentration fields (with high spatial and temporal resolution) at the inlet of our facility, which is essential to provide well-defined inlet boundary conditions for CFD simulations.

Another commonly used instrumentation for the measurement of concentrations is the optical measurement technique Laser-Induced Fluorescence (LIF); however, this system, as well as other optical measurement techniques such as PIV, are not directly applicable to study liquid flows in the presence of density differences because changes in density are typically associated with changes in the refractive index as well. A non-uniform refractive index matching in the test section will lead to blurred PIV and LIF raw images, and therefore to inaccurate measurements. In addition, because we need to measure the time-dependent density field at two cross-sections simultaneously (inlet and main test cross-sections), this would require the use of two separate LIF systems, which is economically challenging (LIF systems are expensive, of the order of a few $100,000 per unit). Furthermore, LIF would also require a calibration target in both measurement

cross-sections to correct for camera distortions. Inserting a calibration target in the facility inlet circular pipe would also be challenging. The aforementioned difficulties are not encountered with WMSs, thus making it our measurement equipment of choice.

2.3 The RCCS Separate-Effects Facility

The RCCS is a key safety system for NGNP reactor designs. This system is designed to passively transfer core decay heat to the environment. The RCCS is designed to operate without the need for operator actions and active components (such as pumps) during accident conditions, providing heat removal from the RPV and the reactor cavity using natural circulation. Two main designs for the RCCS have been proposed, one based on ducts using air from the enviroment as working fluid, and a second design based on pipes with water as working fluid. At Argonne National Laboratory (ANL), the Natural Convection Shutdown Heat Removal Test Facility (NSTF) was built to support the design of the air-cooled RCCS system [47–49]. However, the NSTF's instrumentation, while suitable for validation of system codes, do not always provide the necessary resolution for the validation of CFD models. As a result, local 3D effects are difficult to discern. To study important 3D thermal-hydraulics effects affecting the behavior of the air-cooled RCCS, and to complement the experimental and validation activities performed at ANL, a separate-effects scaled facility was built at the University of Michigan.

The RCCS separate-effects test facility, built in the ECMF laboratory, is a water-based scaled facility of the air-cooled RCCS design and consists of six risers and upper plenum. This facility was built to investigate the interaction of multiple rectangular jets in the RCCS upper plenum, and to study the potential for the formation of a thermal stratified layer. The understanding of the jet interactions and the potential formation of a thermal stratified layer in the RCCS upper plenum is important because this may inhibit natural circulation, and therefore affect the capability of the RCCS to remove heat produced by the core. In this thesis, the facility has been used to gather data and investigate the interaction of multiple water jets in constant-density conditions. Studies in the presence of density differences will be the focus of future investigations. A 3D CAD and a

picture of the facility are shown in Figure 2.8.

(a)

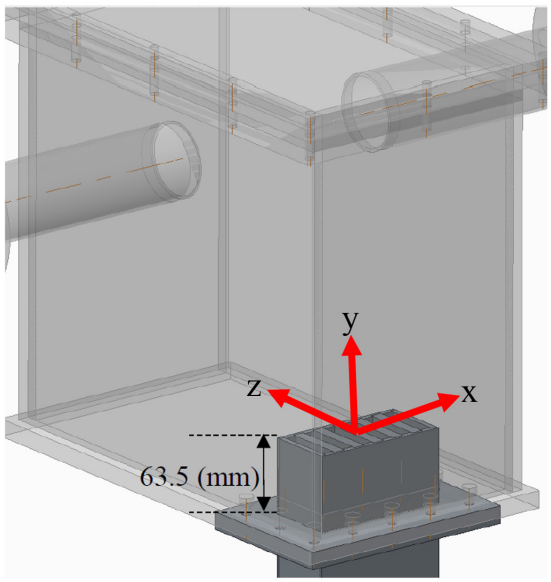

(b)

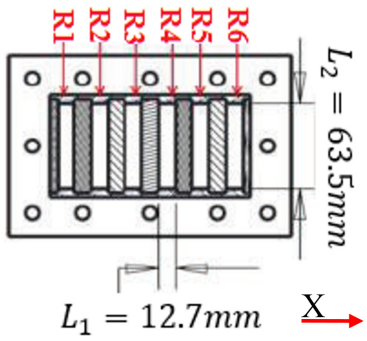

(c)

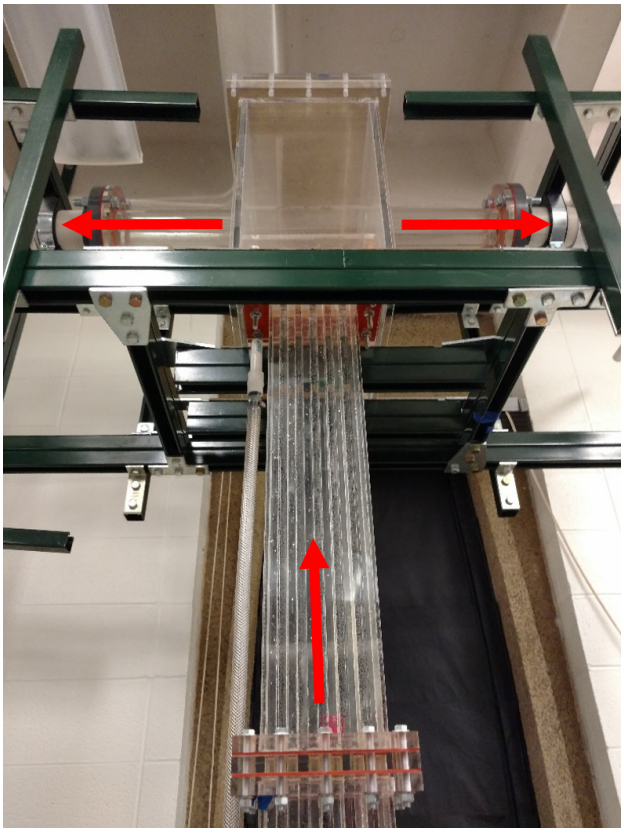

Figure 2.8: The RCCS facility: (a) CAD; (b) Risers dimensions; (c) Facility and flow direction (red arrows).

The scaled facility was designed to study the characteristics of the risers' flows entering the plenum. The fluid in the full-scale facility was air, while the fluid considered for the scaled model was water. Consequently, the scaling methods were developed to preserve the flow dynamics present in the regions of the riser ducts' outlets and the outlet plenum in the full-scale RCCS. The parameters considered for the scaling analysis were the Reynolds number, Froude number, the momentum forces, and the buoyant forces. Furthermore, to validate the analysis, the air flow in the region of the plenum-riser of the full-scale RCCS and the water flow in the plenum-riser of the scaled model were compared through RANS simulations. The comparisons showed good agreement between the velocity and TKE fields produced by the full and scaled facilities, indicating the preservation of the flow dynamics. For further details on the scaling analysis, we refer the reader to Reference [50].

The scaled facility consists of an acrylic upper plenum with dimensions of $470.6 \times 249.3 \times 462\ mm^3$. As shown in Figure 2.8a, the inlet consists of six rectangular risers (rectangular channels) intruded in the upper plenum at a depth of $63.5\ mm$. The risers are labeled R1-R6 and have dimensions of $L_1 \times L_2 = 12.7 \times 63.5\ mm^2$, with a spacing between successive risers of $S = 12.7\ mm$. A zoomed-in view of the riser configuration is shown in Figure 2.8b.

The outlets consist of two circular exhaust pipes with a diameter of $76.2\ mm$. The axial length of the risers is $800\ mm$ – sufficiently long for the flow to fully develop. A picture of our facility is shown in Figure 2.8c. The water is drawn from a 500 gallon reservoir and recirculated across the system. The flows of the six risers are driven by three centrifugal pumps (one pump per riser pair) that are controlled by a variable frequency drive. The flow rates were monitored by turbine flow meters (Blancett 1100) and flow meter monitors (Blancett B3000). The pumps and flow monitors are shown in Figure 2.9. A schematic of the RCCS facility is shown in Figure 2.10, and a list of main components in the schematic is provided in Table 2.1. To ensure that the flow rate shown in the monitors were accurate, a LabVIEW Virtual Instrument (VI) was used to read and record the flow rates during each experimental run. From the tests performed, the measured flow rates remained within one percent of the desired values.

Figure 2.9: Components of the RCCS facility: Three centrifugal pumps, six flow monitors, and six flow control valves.

Table 2.1: List of main components in the RCCS facility schematic.

Main components	Code	Main components	Code
Plenum		Flowmeter 3	FM3
Small Tank 1		Flowmeter 4	FM4
Small Tank 2		Flowmeter 5	FM5
Outlet Tank 1		Flowmeter 6	FM6
Outlet Tank 2		Valve to riser 1	V-riser1
Pump 1		Valve to riser 2	V-riser2
Pump 2		Valve to riser 3	V-riser3
Pump 3		Valve to riser 4	V-riser4
Valve to Small Tank 1	V-st1	Valve to riser 5	V-riser5
Valve to Small Tank 2	V-st2	Valve to riser 6	V-riser6
Valve to Outlet Tank 1	V-ot1	Valve to Outlet Tank 1	V-out-1
3-way Valve 1	3-way V-1	Valve to Outlet Tank 1	V-out-2
3-way Valve 2	3-way V-2	Valve to Outlet Tank 2	V-out-3
Flowmeter 1	FM1	Valve to Outlet Tank 2	V-out-4
Flowmeter 2	FM2		

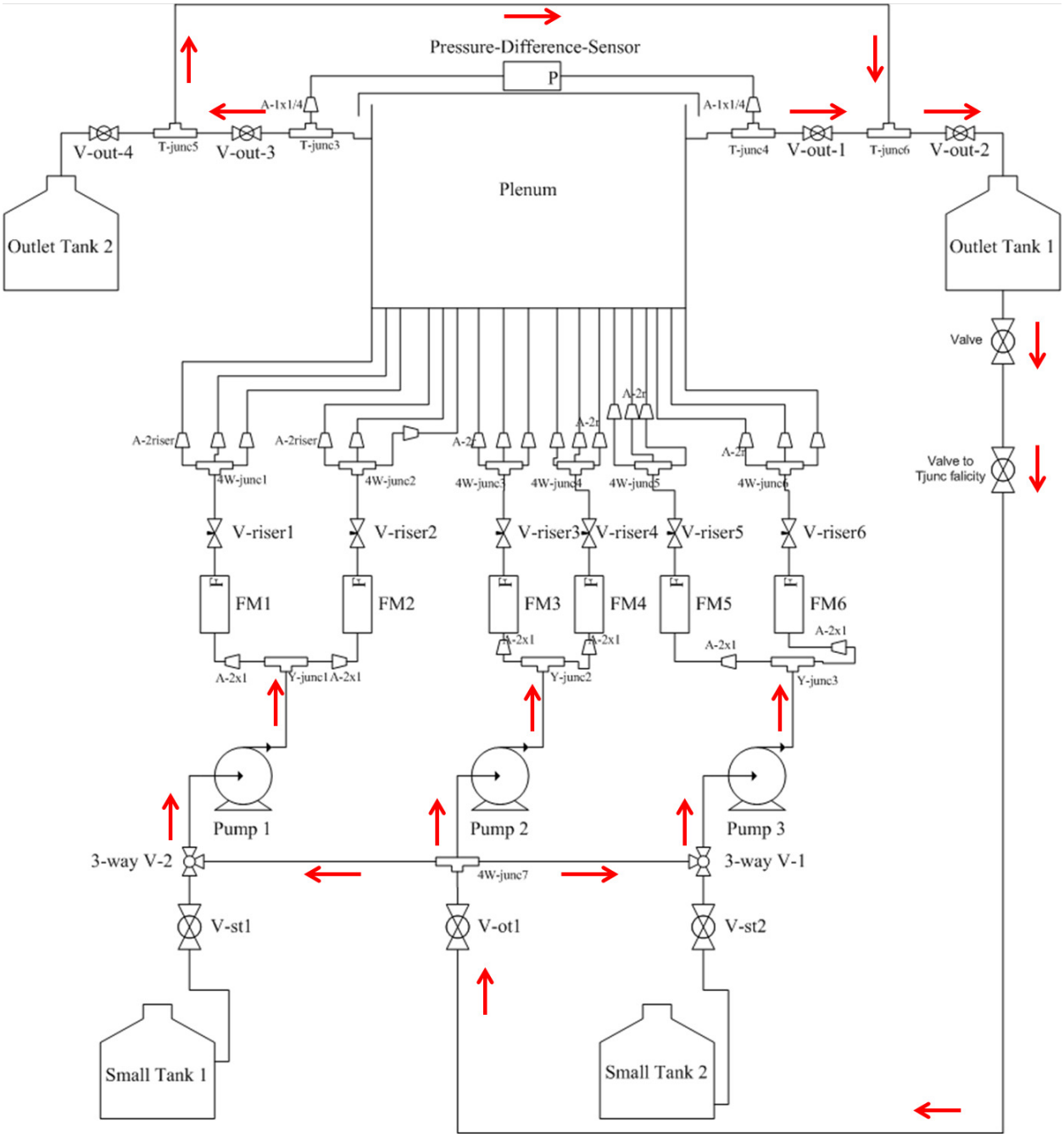

Figure 2.10: Schematic of the RCCS facility. The red arrows indicate the flow direction for the configuration with six operating jets.

2.4 The HiRJet Facility

The propagation of stratified fronts were investigated using the HiRJet facility, shown in Figure 2.11. The HiRJet facility was built at the University of Michigan to establish an experimental

database of high-resolution measurements capturing the propagation of stratified fronts at intermediate Reynolds numbers in the presence of positive and negative density gradients. The density gradients are created by using two different fluids instead of using heating elements as in [15, 51, 52]. With this approach uncertainties from unaccounted heat losses are avoided, and the facility does not need to be insulated, therefore allowing the use of optical measurement techniques as well. In particular water and a sugar-water solution were used as the two working fluids. The sugar concentration in the second fluid was used to change the density difference between the two working fluids.

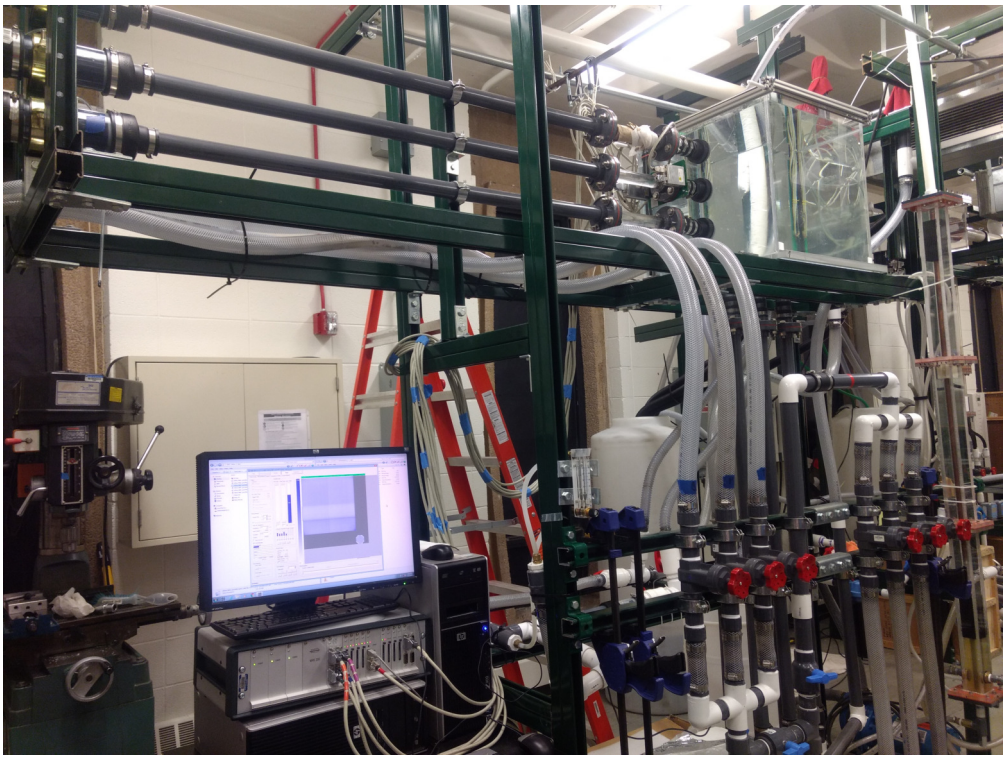

Figure 2.11: Full view of the HiRJet facility.

This facility consists of an acrylic tank with an inner cross section of $58.42\ cm$ by $60.96\ cm$ and a height of $60.96\ cm$. There are a total of six nozzles with an inner diameter D of $38\ mm$. Three nozzles are located on the left side of the tank, and three on bottom face of the tank. Each of the six nozzles is connected by a 1.8m long straight pipe to allow the flow to fully develop before entering the tank. All of the nozzles can be used as inlets or outlets; the experiments and simulations carried out for this thesis were performed using the middle nozzles on the side and

on the bottom of the tank as the inlet and outlet, respectively, as illustrated in Figure 2.13a. All the other nozzles remained closed. A simplified schematic of this facility illustrating only the nozzles in use, and a list of the components in this schematic, are given in Figure 2.12 and Table 2.2, respectively. For further details of the HiRJet facility we refer the reader to Reference [46].

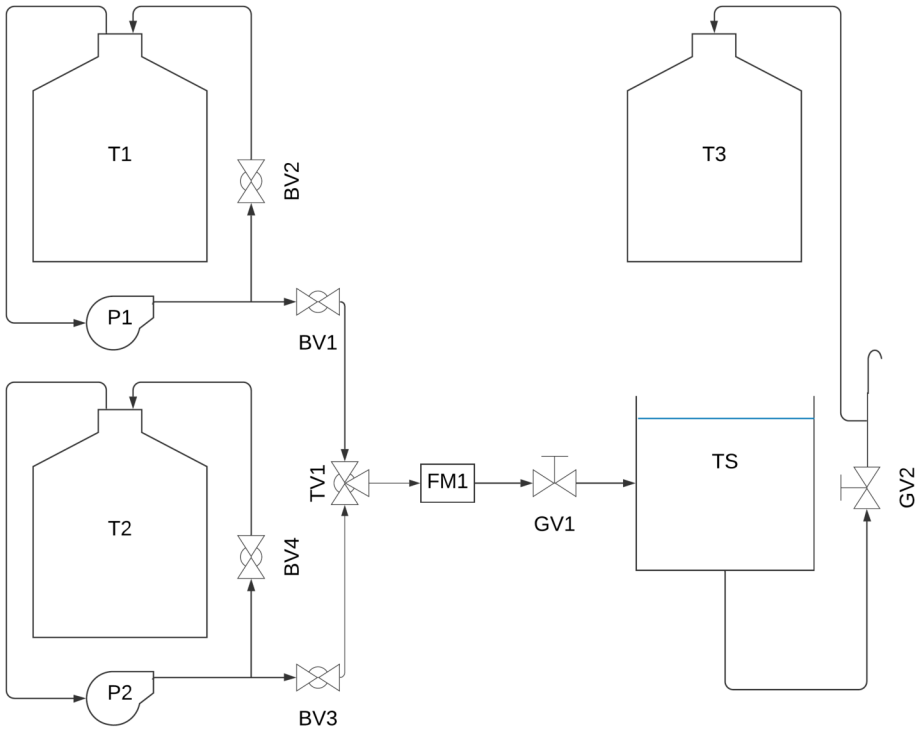

Figure 2.12: Simplified schematic of the HiRJet facility. The black arrows indicate the flow direction.

Table 2.2: List of main components in the HiRJet facility schematic.

Main components	Code	Main components	Code
Test Section	TS	Valve to Tank 1	BV1
Reservoir Tank 1	T1	Recirculation Valve 1	BV2
Reservoir Tank 2	T2	Valve to Tank 2	BV3
Outlet Tank	T3	Recirculation Valve 2	BV4
Pump 1	P1	Inlet Valve	GV1
Pump 2	P2	Outlet Valve	GV2
Three-way Valve 1	TV1		

The HiRJet facility is equipped with a WMS system to trace the propagation of fluids with

different densities. As shown in Figure 2.13a and 2.13c, there is a WMS upstream of the inlet, and a larger WMS inside the tank. Throughout this thesis, we refer to these WMS units as the “inlet WMS" and “large WMS" respectively.

A Coriolis flow meter (Endress+Hauser) in conjunction with LabView was used to measure the flow-rate circulating in the facility. The inlet boundary conditions were monitored with the inlet WMS (time-dependent density distribution) and a Laser Doppler Velocimetry (LDV) system (Artium Technologies). The latter was utilized to obtain the stationary inlet velocity profile in the acrylic section upstream of the inlet WMS. A close-up view of the LDV system is shown in Figure 2.13b.

The density of the two working fluids were measured using a 100mL flask and a high accuracy scale. These values were verified by measuring the degrees Brix number using a Digital Refractometer (Sper Scientific 300037). Furthermore, the viscosities of the working fluids were measured via an Ostwald viscometer. Knowing the density and viscosity of one working liquid (tap water) and the density of the second working liquid (sugar solution), one can calculate the viscosity of the second fluid via Equation 2.3:

$$\begin{aligned} \mu_x &= \mu_w \frac{\rho_x}{\rho_w} \frac{t_x}{t_w}, \\ \nu_x &= \frac{\mu_x}{\rho_x} = \nu_w \frac{t_x}{t_w}, \end{aligned} \tag{2.3}$$

where μ is the dynamic viscosity, ν is the kinematic viscosity, ρ is the density, and t is the time it takes the fluid to flow through the capillary under the influence of gravity. The subscripts w and x denote tap water and sugar solution, respectively. By closely monitoring the boundary conditions and measuring the fluid properties, we ensure that adequate and accurate boundary conditions are provided for the CFD simulations.

(a)

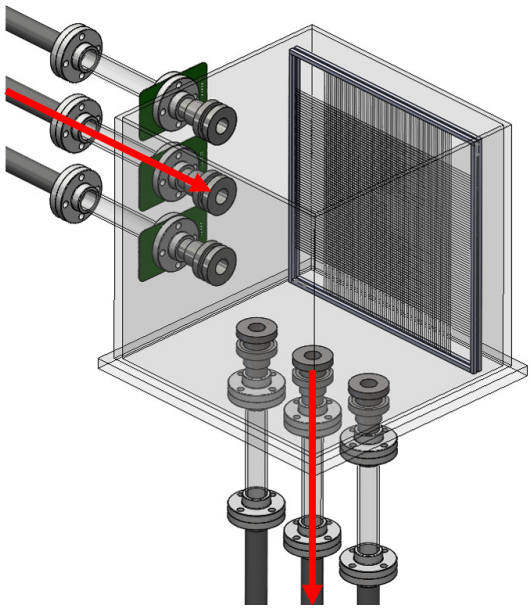

(b)

(c)

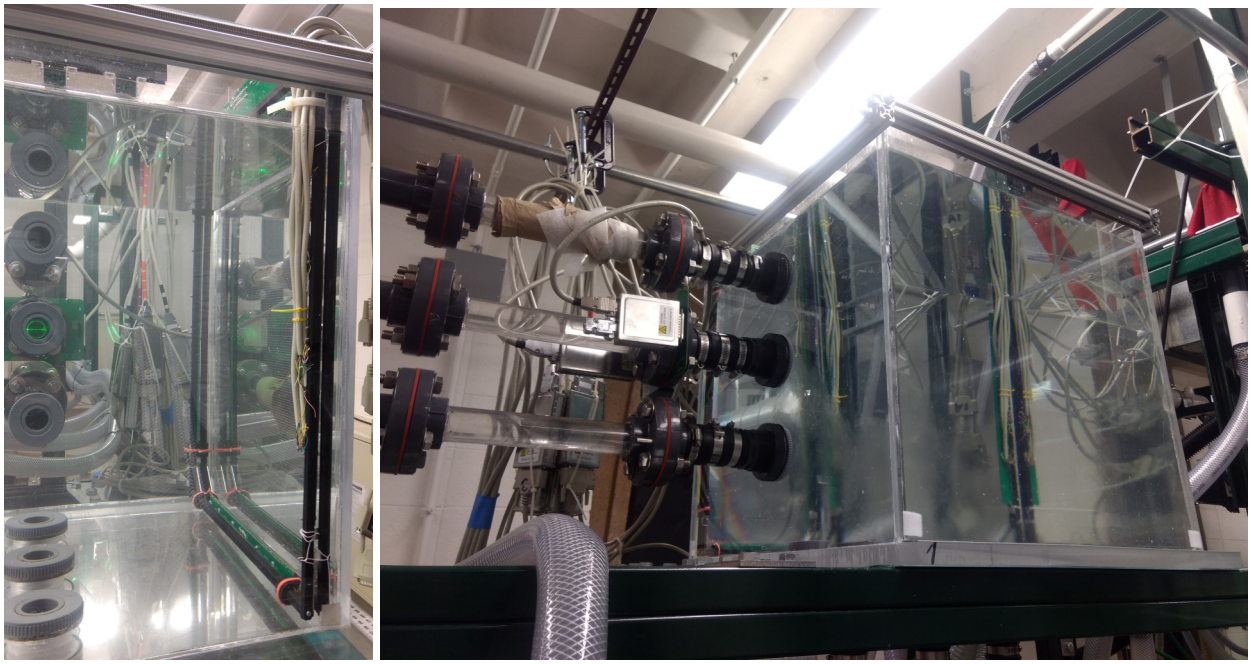

Figure 2.13: Pictures of the HiRJet facility: a) CAD of the HiRJet facility (flow direction in red); b) LDV located near the inlet section; c) Large WMS in tank and view of the LDV laser.

Chapter 3

The RCCS Separate-Effects Test Facility

Many efforts have been devoted into explaining the patterns/structures in the flow fields of dual plane jets through various statistical analyses of experimental and numerical data. In cases where a comparison between experiments and simulations were made, the authors reported generally good agreement in the mean velocity fields but significant differences between the Reynolds stresses. In this chapter, we experimentally investigate the possible causes for the discrepancies in their analyses. Our investigation of parallel jets includes PIV measurements taken in the RCCS separate-effects test facility. In Section 3.1, we provide an overview of previous literature on the study of dual plane jets. In Section 3.2, we provide a comparison between the time-averaged statistics of two, four, and six jets in the RCCS facility. In Section 3.3, we performed repeatability and reproducibility tests to quantify how small variations in the experimental conditions can have large effects on the statistical quantities. We quantify the level of uncertainty associated with advanced instrumentation such as PIV, and describe how these tests are an important factor when generating CFD-grade experimental databases for development and validation of CFD models. Furthermore, we utilize these data to identify discrepancies between our experiments and RANS simulations. In Section 3.4, we provide time-resolved experimental data and analyze the flow fields through PSD and SPOD. Lastly, in Section 3.5, we provide a summary of the contributions and findings from these experiments.

3.1 Overview

Dual-parallel plane jets have been extensively studied experimentally and numerically over several decades and distinct flow regions have been observed. In a two jet configuration, the entrainment between jets creates a low pressure region which draws both jets towards each other and induces an exchange of energy between them. As illustrated in Figure 3.1, the flow fields can be described as three flow regions: 1) a converging region, where there is a recirculation zone in between the inner shear layers which leads to the merging point (mp), 2) a merging region, where the jets interact with each other until the combined point (cp) which leads to a 3) combined region, where the jets have merged and resemble a single jet. A list of several studies on parallel rectangular jets is given in Table 3.1.

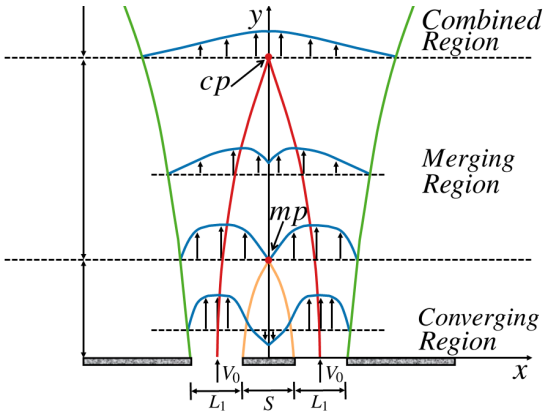

Figure 3.1: Schematic of the flow field for two-dimensional parallel jets. Adapted from Mondal et al. [58].

The initial experimental studies on dual-jet flows were carried out by Miller and Comings [53], where they described the resemblance between the flow structures of the combined dual-jets and a single jet flow at a high Reynolds number. Tanaka [54] [55] experimentally investigated the effects of the spacing between jets on the velocity, turbulence, and static pressure in the regions of jet interference at intermediate Reynolds numbers. They determined that these quantities fluctuate considerably due to the interference between the jets, that the width of the combined jets spreads linearly in the downstream direction, and that the combined jet spread increases with increasing jet spacing S.

Table 3.1: List of experiments and simulations of rectangular parallel jets.

Year	Authors	Re	S/L_1	Technique
1960	Miller and Comings	17,800	5	HWA
1970	Tanaka	4,290–8,750	7.5–25.3	HWA
1974	Tanaka	4,290–8,750	7.5–25.3	HWA
1983	Elbanna et al.	20,000	11.5	HWA
1989	Ko and Lau	40,000	1.5	HWA
1990	Lin and Sheu	7,600	29, 39	LDA
1997	Nasr and Lai	11,000	4.25	LDA
2001	Anderson and Spall	6,000	9–18.25	LDA, 2D RANS
2003	Anderson et al.	10,000–40,000	0.5–2	LDA
2005	Bunderson and Smith	21,500 and 43,000	6–26	HWA
2016	Mondal et al.	10,000	0.5–2.0	2D RANS
2017	Lee et al.	9,100	2.07	PIV
2017	Li et al.	9,100	2.07	RANS and PANS
2018	Li et al.	9,100	2.07	LES

Elbanna et al. [56] experimentally determined that the velocity profiles of the combined jet spread are similar and agree with the profiles of a single jet in the combined region. Furthermore, they observed that the centerline velocity decayed with the same rate as the single jet, but with larger amplitude; however, the distributions of the turbulent kinetic energy differed from those of a single jet. Through experimental investigation, Lin and Sheu [57] determined that the mean velocity fields are self-preserving in the merging and combined regions, while the turbulent intensities and the Reynolds shear stress are self-preserving only in the combined region.

In an experimental study, Ko and Lau [59] discerned the presence of coherent structures within the inner and outer mixing regions of each jet by means of cross-spectral analysis. Through their studies they noticed slightly more pronounced spectral peaks in the inner mixing layer than in the outer mixing layer. They speculated that the lack of sharpness in the spectral peaks in the outer mixing layer was due to vortex pairing in the inner mixing layers. Nasr and Lai [60] experimentally investigated the effects of an offset wall replacing the symmetry plane of parallel jets. They determined that a larger recirculation region was formed for the case with the offset wall. The experimental and computational investigation by Anderson and Spall [21] indicated that the merged and combined points of the parallel jets were well predicted by RANS CFD simulations.

Their results showed that the velocity profiles were well captured by the simulations; however, there were large discrepancies in the magnitude and decay of the profiles of the Reynolds normal and shear stresses. Anderson et al. [61] experimentally investigated the effect from varying the jet width L_1 while the jet spacing S was kept constant. Their investigation covered the range of $0.6 < S/L_1 < 2.0$, and their results indicated that periodic vortex shedding (similar to the flow behavior observed in the flows over bluff bodies) occurs for $S/L_1 > 0.6$. Their results indicated that a decrease in S/L_1 led to an increase in the vortex shedding frequencies. Furthermore, the experiments by Bunderson and Smith [62] revealed an instability characterized by sinuous flapping of the jets which leads to an increase of momentum transfer with the surrounding fluid. Their results also exhibited an increase in the vortex shedding frequencies for decreasing S/L_1 ratios.

Mondal et al. [58] numerically investigated the flow dependence on the jet separation distance for $0.5 < S/L_1 < 2.0$. Their results agreed with previous findings in that with an increase in separation distance S (i.e., with increasing S/L_1), there is a decrease in the Strouhal number

$$St = \frac{fL}{V_0} = \frac{\text{Unsteady Acceleration}}{\text{Advective Acceleration}}, \tag{3.1}$$

where f is the frequency of vortex shedding, L is the characteristic length (i.e., the jet hydraulic diameter), and V_0 the nominal velocity. Moreover, the frequency spectra of the streamwise and cross-stream velocity time series displayed a single dominant frequency at the same Strouhal number, at which periodic shedding occurred. Their results indicated that only the inner shear layers of both jets periodically interact with each other only within the range of $0.6 < S/L_1 < 1.4$, generating a well-organized von Karman vortex street. Lee and Hassan [63], investigated the flow structures of two parallel plane jets by employing a POD analysis along with PSD estimates, and they determined characteristic frequencies related to vortex pairing. Li et al. [64, 65] numerically investigated dual-jet flows using RANS and LES models. Their comparison between the RANS numerical data and the experimental data revealed good agreement

in the merging point region. On the other hand, the Reynolds stress components were largely over-predicted by the RANS models. Similar outcomes were observed for the LES results with the improvement in the agreement of the the dominant frequencies present in the flow.

3.2 Time-Averaged Statistics

3.2.1 Test Matrix

The data provided in this section consists of planar PIV measurements in the midplane of the RCCS's rectangular channels. An illustration of the measurement cross-section (xy-plane) and the location of the camera and laser for PIV measurements are shown in Figures 3.2a and 3.2b, respectively.

(a)

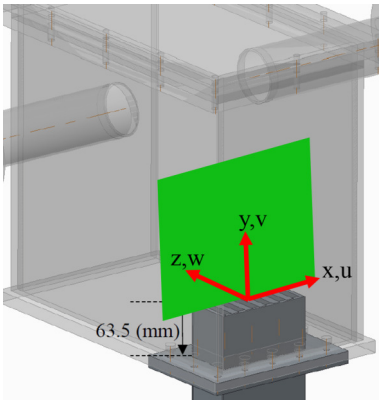

(b)

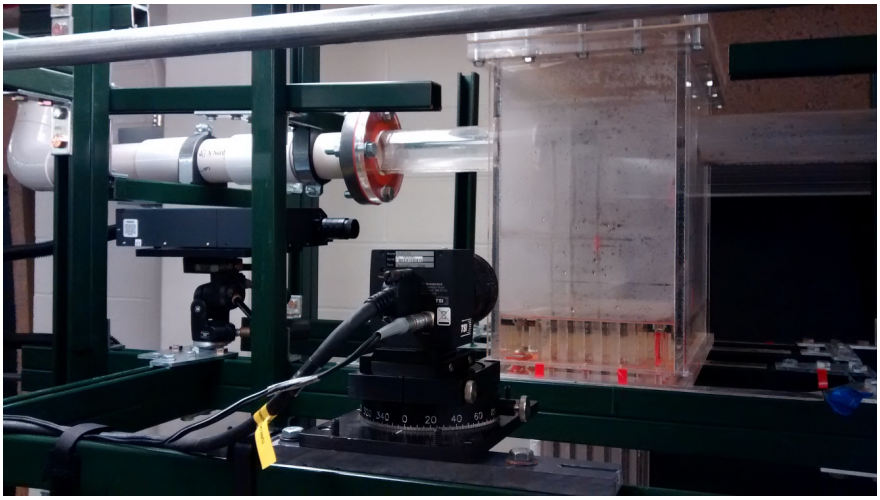

Figure 3.2: PIV setup in the RCCS facility: a) Laser plane location; b) Picture of the setup.

Three measurements were used to compare the flow statistics of two, four, and six jets. The experiments were conducted in constant-density conditions at a Reynolds number $Re = 13,800$[1]. To achieve statistical convergence of the time-averaged quantities of interest, the number of recorded samples must be high, and the sampling frequency must be low enough to ensure independent sampling [66]. To meet this criteria, the PIV system was used in Double-Frame Double-Exposure mode with a recording rate of $50\ Hz$. Additional information about the measurements are provided in Table 3.2.

Table 3.2: PIV recording information.

	Two Jets	Four Jets	Six Jets
Re (–)	13,800	13,800	13,800
Temperature (°C)	23.06	22.95	23.19
Recording Rate (Hz)	50	50	50
Total Number of Image Pairs Recorded (–)	30,000	30,000	30,000

We first focus our analysis on the mean velocities and Reynolds stresses, which are calculated by Equations 3.2 and 3.3, respectively:

$$\begin{aligned} U_i(\boldsymbol{x}) &= \overline{u_i} \\ &= \overline{u_i(\boldsymbol{x}, t)} \\ &= \frac{1}{M} \sum_{k=1}^{M} u_i(\boldsymbol{x}, t_k), \end{aligned} \tag{3.2}$$

$$\begin{aligned} \overline{u_i' u_j'} &= \overline{u_i'(\boldsymbol{x}, t) u_j'(\boldsymbol{x}, t)} \\ &= \frac{1}{M-1} \sum_{k=1}^{M} u_i'(\boldsymbol{x}, t_k) u_j'(\boldsymbol{x}, t_k), \end{aligned} \tag{3.3}$$

where U_i is the time-averaged/mean velocity, $u_i(\boldsymbol{x}, t_k)$ the instantaneous velocity, $u_i'(\boldsymbol{x}, t_k)$ the

[1]The volumetric flow rate measured through each channel was 8.4 Gallons Per Minute (GPM).

turbulent fluctuations, and $\overline{u_i' u_j'}$ the Reynolds stresses. Here, the subscripts i and j can have values $n = 1, 2, 3$ which indicate the x, y, and z directions based on the coordinate system shown in Figure 3.2a. The velocity components u, v, w correspond to the directions x, y, z, respectively.

To estimate variations in our measurements, uncertainty bands were constructed by considering various sources of uncertainty. The propagation of uncertainty for a variable $R(x_1, x_2, ..., x_N)$ can be calculated by [67]:

$$\sigma(R) = \sqrt{\sum_{n=1}^{N} \left(\frac{\partial R}{\partial x_i} \sigma(x_i) \right)^2}, \tag{3.4}$$

where $\sigma(R)$ is the overall uncertainty in R, N the number of sources considered, and $\sigma(x_i)$ is the uncertainty in each variable x_i. Uncertainties due to drag of the seeding particles, due to the correlation functions used for vector calculations, and statistical/random[2] uncertainties are considered.

The statistical uncertainty of the time-averaged velocities (population mean) $\sigma_{Stat}(U_i)$ were calculated by [68]:

$$\sigma_{Stat}(U_i) = t \frac{s(U_i)}{\sqrt{M}}, \tag{3.5}$$

where t is the Student's t-distribution, $s(U_i)$ the standard deviation of the mean velocity component U_i, and M the total number of samples. On the other hand, the lower (L) and upper (U) bounds of the statistical uncertainty of the Reynolds stresses (population variance) is estimated by [68]:

$$\sigma_{Stat,L}(\overline{u_i' u_j'}) = \frac{\sqrt{M-1}}{\chi_L} \overline{u_i' u_j'}, \tag{3.6}$$

$$\sigma_{Stat,U}(\overline{u_i' u_j'}) = \frac{\sqrt{M-1}}{\chi_U} \overline{u_i' u_j'}, \tag{3.7}$$

where χ_L and χ_U are the lower and upper bounds of the χ^2 distribution. The difference in formulations arise from the fact that the sampling distribution of the Reynolds Stresses (sample

[2]Uncertainties that arise from random fluctuations in a measurement.

variance) is not normal. As a results, this gives rise to asymmetric uncertainties bands for the Reynolds stresses.

3.2.2 Time-Averaged Statistics

3.2.2.1 Mean Streamwise Velocity

The time-averaged velocities of two, four, and six jets were analyzed to provide a brief description of the flow fields and to point out similarities and differences between the different configurations. The flow fields and profiles (along the streamwise direction y/L_1) of the mean streamwise velocity V for the three configurations with Reynolds number $Re = 13,800$, are provided in Figure 3.3. From these flow fields, similar jet merging characteristics are noticeable. In the two jet configuration (Figure 3.3a), the jets tend to merge towards the symmetry plane due to entrainment, thus the inner shear layers eventually meet and interact with one another. The case with four jets (Figure 3.3b) also indicates that the jets tend to merge; however, the two leftmost and two rightmost jets merge separately. This behavior indicates that the level of entrainment in the middle of all jets (i.e., $x/L_1 = 0$) is lower than that of the middle of the two leftmost and two rightmost jet pairs. Furthermore, the field of the six jets (Figure 3.3c) indicates that a weaker merging region is present in this configuration (i.e., the merging pattern observed for the other configurations is not as evident).

The velocity profiles of the inner middle jets (i.e., same jets as in the two jet configuration) provide additional perspectives. The velocities with their corresponding uncertainty bands at several streamwise locations are provided in Figures 3.3d and 3.3e. The profiles at $y/L_1 = 1$ indicate that the maximum velocities are essentially equal for all configurations (i.e., equal within the uncertainty bands) and suggests that the flow conditions were replicated for the two inner jets. At locations $y/L_1 \geq 2$ some differences arise. The jets begin merging earlier in the two jet configuration, with the four and six jet configurations following after. That is, the distance between the peaks of the profiles is shortest for the case with two jets, and longest for the six jet configuration. At locations $y/L_1 \geq 4$, the highest and lowest maximum velocities correspond to

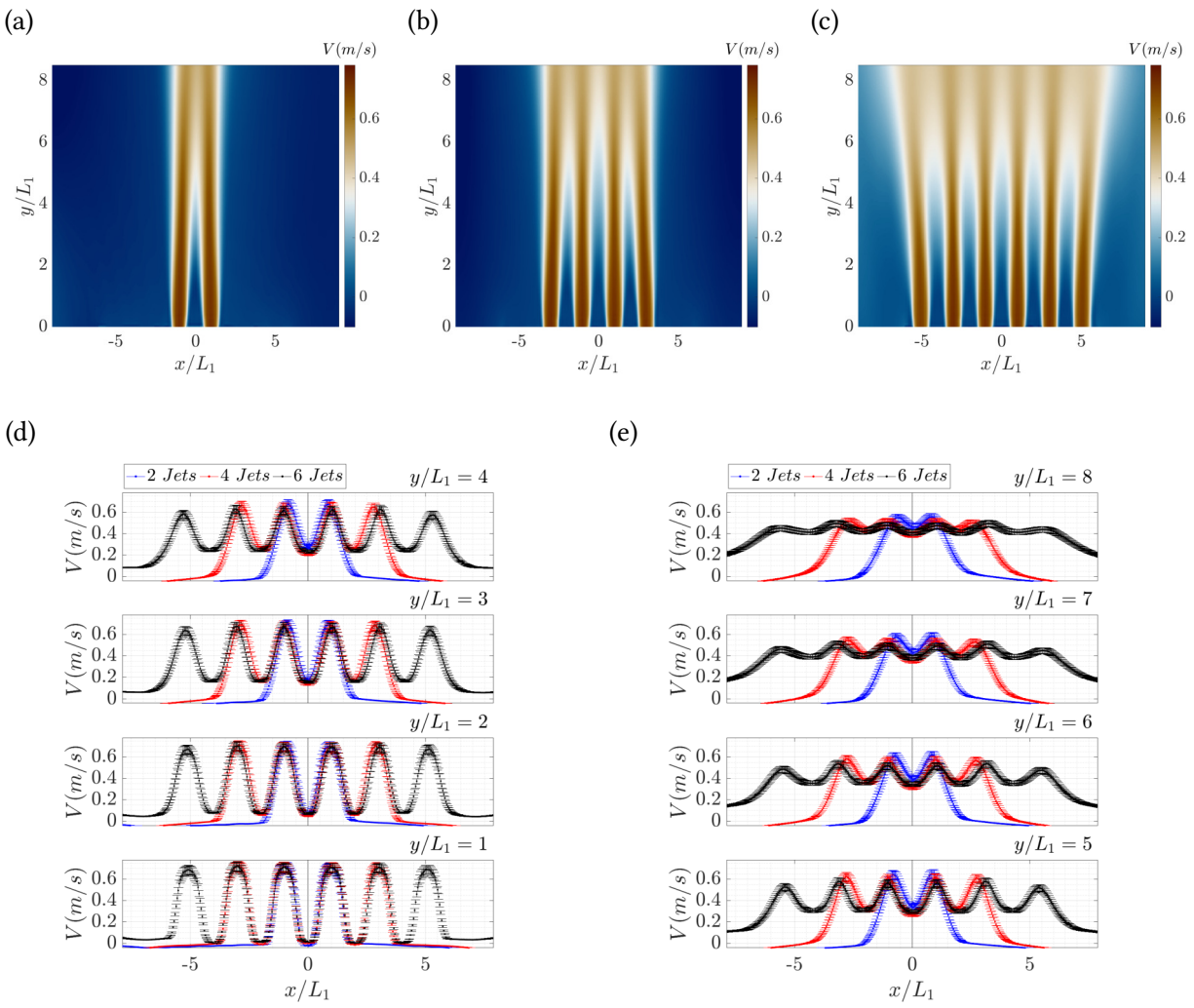

Figure 3.3: Mean streamwise velocity V fields: a) 2 Jets; b) 4 Jets; c) 6 Jets, and profiles at various axial locations: d) $y/L_1 = 1 - 4$; e) $y/L_1 = 5 - 8$ for $Re = 13,800$.

the cases with two and six jet configurations, respectively. This can be explained by the fact that as the volumetric flow rate increases, the jets tend to curve towards the outlets [69]. Furthermore, the overall entrainment in the regions near the walls increases as the number of jets increase. This is displayed as lighter blue regions near the walls in the fields of the six jet configuration.

3.2.2.2 Reynolds Stresses

The Reynolds normal stresses give information about turbulent intensity along each direction of the flow and about the contributions to the TKE $k = \frac{1}{2}\left(\overline{u'u'} + \overline{v'v'} + \overline{w'w'}\right)$. The flow fields and profiles of the Reynolds normal stresses $\overline{u'u'}$ and $\overline{v'v'}$ are reported in Figures 3.4 and 3.5,

respectively. The $\overline{u'u'}$ and $\overline{v'v'}$ profiles at $y/L_1 = 1$ indicate high turbulence intensity near the shear regions (i.e., outside the jet core). As expected, the streamwise component $\overline{v'v'}$ exhibits larger amplitudes because the velocity field is dominant in the streamwise direction. As shown in Figures 3.4d and 3.4e, the profiles of cross-stream stresses $\overline{u'u'}$ for all configurations exhibit the same behavior; however, the spread along x/L_1 and the magnitude of the $\overline{u'u'}$ profiles in the regions near the walls increases as the number of jets increase. Furthermore, the profiles of the $\overline{v'v'}$ component are shown in Figures 3.5d and 3.5e. At $y/L_1 = 1$, the amplitude of $\overline{v'v'}$ is approximately the same at the inner and outer layers. At regions $y/L_1 \geq 3$ the magnitudes are larger in the regions near the side walls for all cases, with the largest occurring in the case with six jets as seen in the $\overline{u'u'}$ profiles.

The Reynolds shear stress $\overline{u'v'}$, shown in Figure 3.6, provides information about the circulation in the flow, where positive and negative values indicate clockwise and counter-clockwise rotations, respectively. In this case too, the magnitude of the profiles are in good agreement at $y/L_1 = 1$, while for $y/L_1 \geq 2$ the amplitudes of these profiles and the spread along x/L_1 varies between the different configurations. For all jet configurations, the profiles near the inner shear layers reach a maximum at $y/L_1 = 4$ and start decaying from then on. In the case for six jets, in the outermost shear layers (regions not enclosed by the jets), this maximum remains constant but shifts towards the side walls for increasing y/L_1. The increase and shift of the Reynolds shear stresses near the wall regions occur due to the overall expansion of the combined jets shown in the Figure 3.3, where the broader expansion is exhibited in the six jet case.

In this section, we provided high-resolution experimental data with their corresponding uncertainties. Based on the inspection of the fields and profiles of the mean velocity and Reynolds stresses, we obtained a general description of the similarities between the different configurations. While these measurements contain data with high spatial resolution, and the velocity fields and profiles appear to be promising results, it is of great importance to investigate if these measurements can be replicated. To ensure the reliability of these data, we investigate the repeatability and reproducibility of the PIV measurements in Section 3.3.

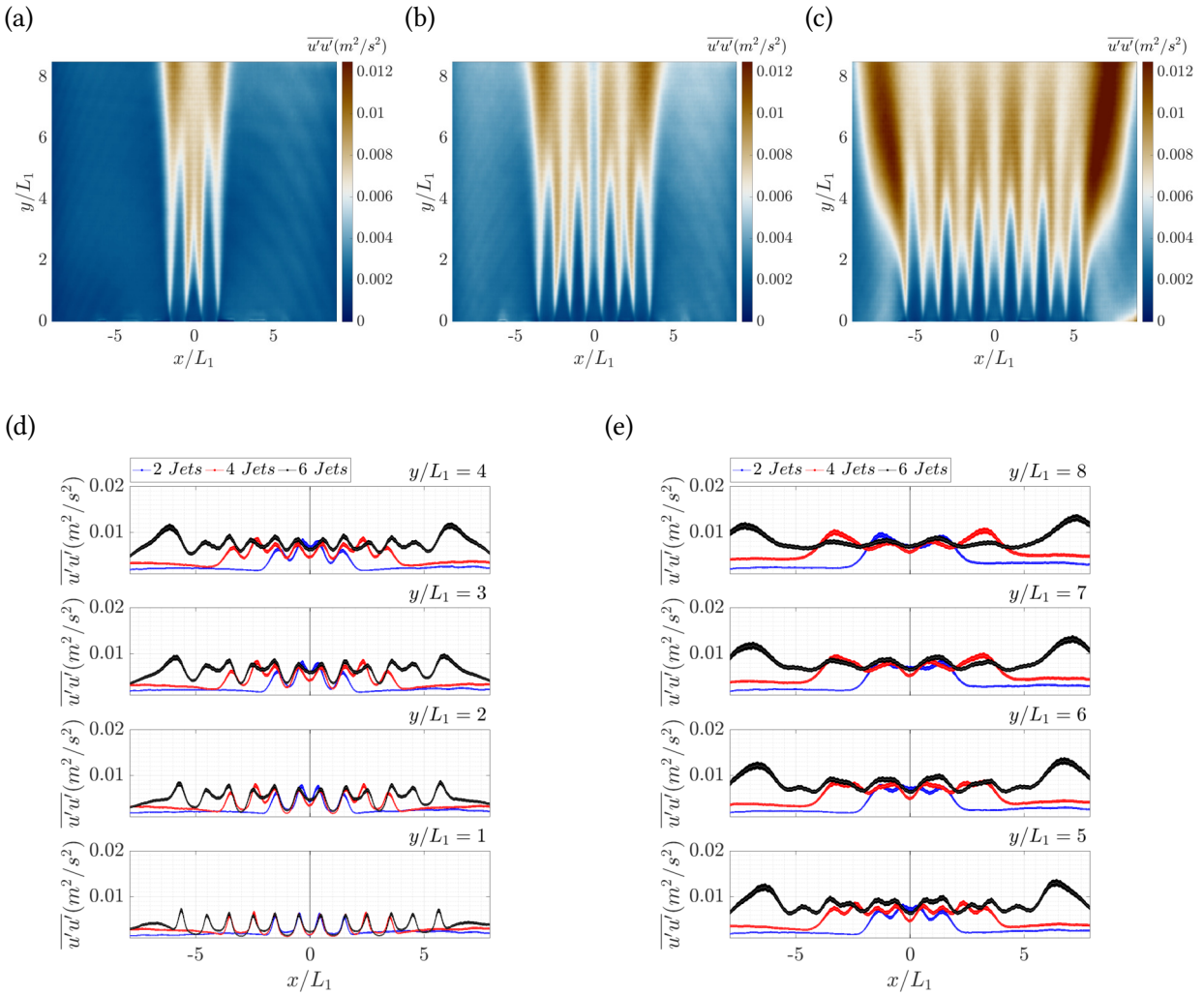

Figure 3.4: Reynolds normal stress $\overline{u'u'}$ fields: a) 2 Jets; b) 4 Jets; c) 6 Jets, and profiles at various axial locations: d) $y/L_1 = 1 - 4$; e) $y/L_1 = 5 - 8$ for $Re = 13,800$.

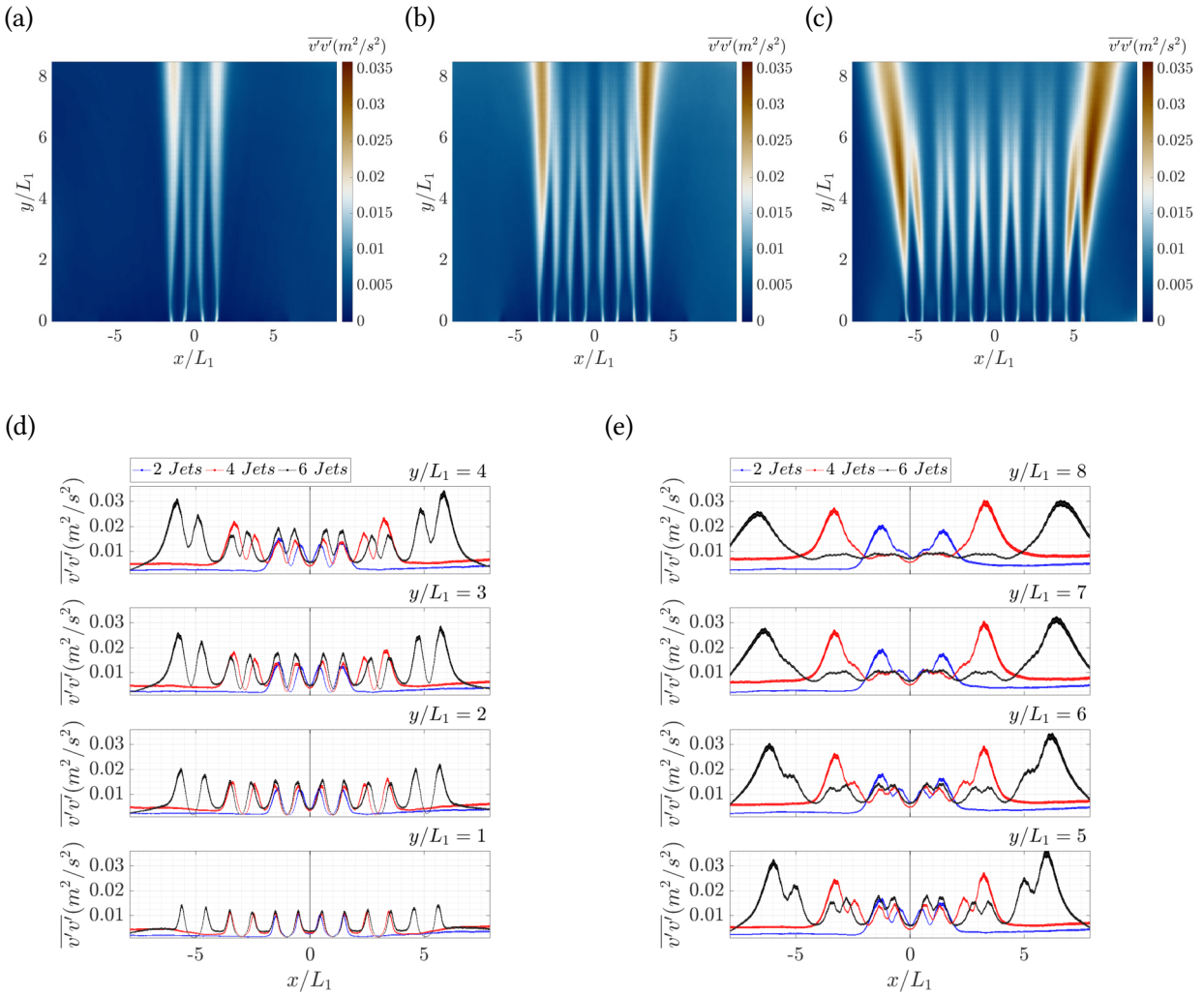

Figure 3.5: Reynolds normal stress $\overline{v'v'}$ fields: a) 2 Jets; b) 4 Jets; c) 6 Jets, and profiles at various axial locations: d) $y/L_1 = 1 - 4$; e) $y/L_1 = 5 - 8$ for $Re = 13,800$.

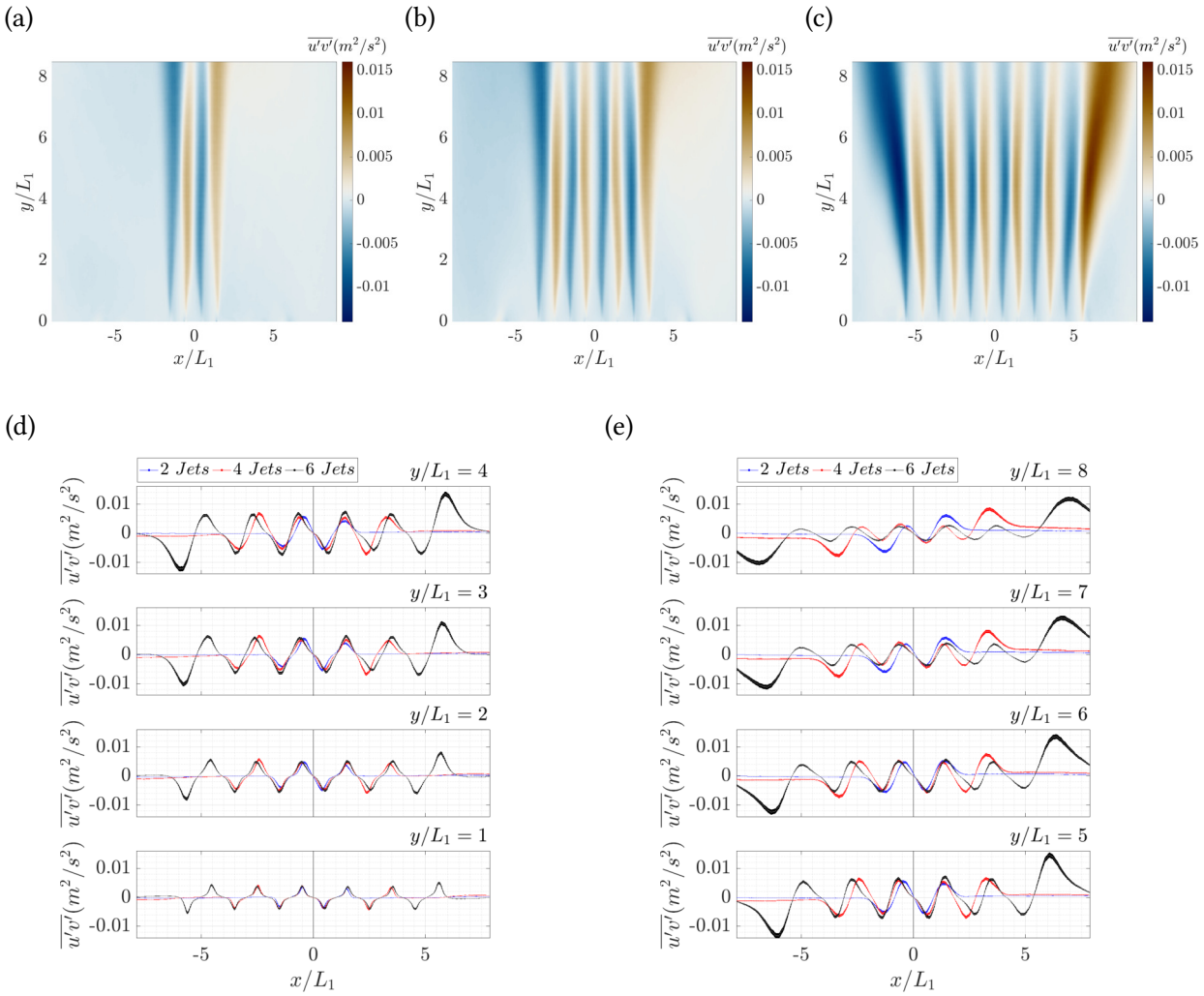

Figure 3.6: Reynolds shear stress $\overline{u'v'}$ fields: a) 2 Jets; b) 4 Jets; c) 6 Jets, and profiles at various axial locations: d) $y/L_1 = 1 - 4$; e) $y/L_1 = 5 - 8$ for $Re = 13,800$.

3.3 Repeatability and Reproducibility of PIV Measurements

3.3.1 Motivation

PIV has been utilized over several decades for flow visualization. Technological advances have made this tool more accessible, and as a result, large quantities of PIV data are constantly being generated. Because of the complexity of PIV systems, user errors occasionally become a source of uncertainty in the data, which is infrequently quantified in the literature. For this reason, PIV experiments should be held to rigorous standards, and experimentalists should be able to demonstrate the accuracy and precision of the their measurements based on their setups [70]. While the experimentalist community attempts to produce reliable PIV data, standardized practices should be followed to improve the fidelity of the data. A very simple, yet effective way to decrease discrepancies in PIV data is by checking how well the PIV results can be replicated. To do so, we can check the repeatability (i.e., the ability to obtain the same results by conducting the same experiment with the same equipment) and the reproducibility (i.e., the ability to obtain the same results with different instrumentation or in a replica of the facility at some other location) of the PIV results. By assessing these two quantities, we can provide PIV results with information about the variations between experiments. The incorporation of these variations are essential when compiling CFD-grade databases whose purpose is to help with code development and validation.

Over the past decade, several benchmark exercises have used PIV results as reference data for CFD simulations [71–74]. These benchmarks provide essential insight into how well experiments can be predicted with CFD. An interesting outcome of these reports is that there are large variations between the CFD results obtained by different users. Similarly, if an experiment were to be conducted at separate facilities, some differences would appear between the results. By the nature of experiments, additional variations can occur even when the experiments are repeated in the same facility, and these differences should be accounted for in the uncertainty bands of the PIV data.

Many efforts have been made to assess the quality and significance of PIV results through uncertainty quantification of PIV measurements [66, 75–78]. These efforts include but are not limited to estimating the uncertainty in the PIV algorithms affected by peak-locking, warping of images, particle densities, out-of-plane motion, use of different PIV software, etc. While these contributions are very important, we also need to consider the contribution to the uncertainties from changes in the system's behavior and user error. With this being said, it is important to check if we can reproduce the same results using the same equipment and facility on separate occasions.

3.3.2 Test Matrix

To investigate the repeatability and reproducibility of PIV results in the RCCS facility, five experiments with the six jet configuration were conducted on separate dates. The experiments were conducted at constant density conditions with jet Reynolds numbers $Re = 13,800$. To verify the repeatability, we conducted three measurements with the pulsed laser (P1, P2, and P3). To verify the reproducibility, we used a Continuous Wave (CW) laser. An additional measurement with the pulsed laser (P4) was also executed to understand discrepancies caused by laser misalignment. The recording frequencies for the PIV measurements with the continuous wave and pulsed lasers were 50 and 10 Hz, respectively. Additional information about the experiments is provided in Table 3.3.

Table 3.3: PIV recording information for the repeatability and reproducibility measurements.

	P1	P2	P3	CW	P4
Reynolds Number	13,800	13,800	13,800	13,800	13,800
Temperature (°C)	21.62	21.25	20.84	23.19	16.35
Recording Rate (Hz)	10	10	10	50	10
Total Number of Image Pairs Recorded (–)	18,000	18,000	18,000	30,000	32,800

In this section, we will refer to each experiment with the following abbreviations:

- P1: First measurement with the pulsed laser. This measurement is used as the reference case.

- P2: Second measurement with the pulsed laser. This measurement was conducted a day after P1 without making any changes to the location of the PIV system. This test aimed to capture the variations that might arise from changes in the system behavior (e.g., behavior of pumps).
- P3: Third measurement with the pulsed laser. This measurement was taken to check for differences in the results from realigning the laser system.
- CW: This measurement uses a continuous wave laser to check for the reproducibility of the PIV data with another laser system.
- P4: Fourth measurement with the pulsed laser. This measurement was taken to gauge the differences caused by the misalignment of the laser sheet.

The time-averaged fields for case P1 are provided in Figure 3.7. These flow fields resemble the results from Section 3.2.2; however, the goal is to understand how different experimental situations affect the measurement results. First, we investigate the statistical convergence of the time-averaged quantities in Section 3.3.3 to illustrate the effects of insufficient image pairs for time-averaging. Then, in Section 3.3.4, we proceed with an investigation of the precision of these different data sets.

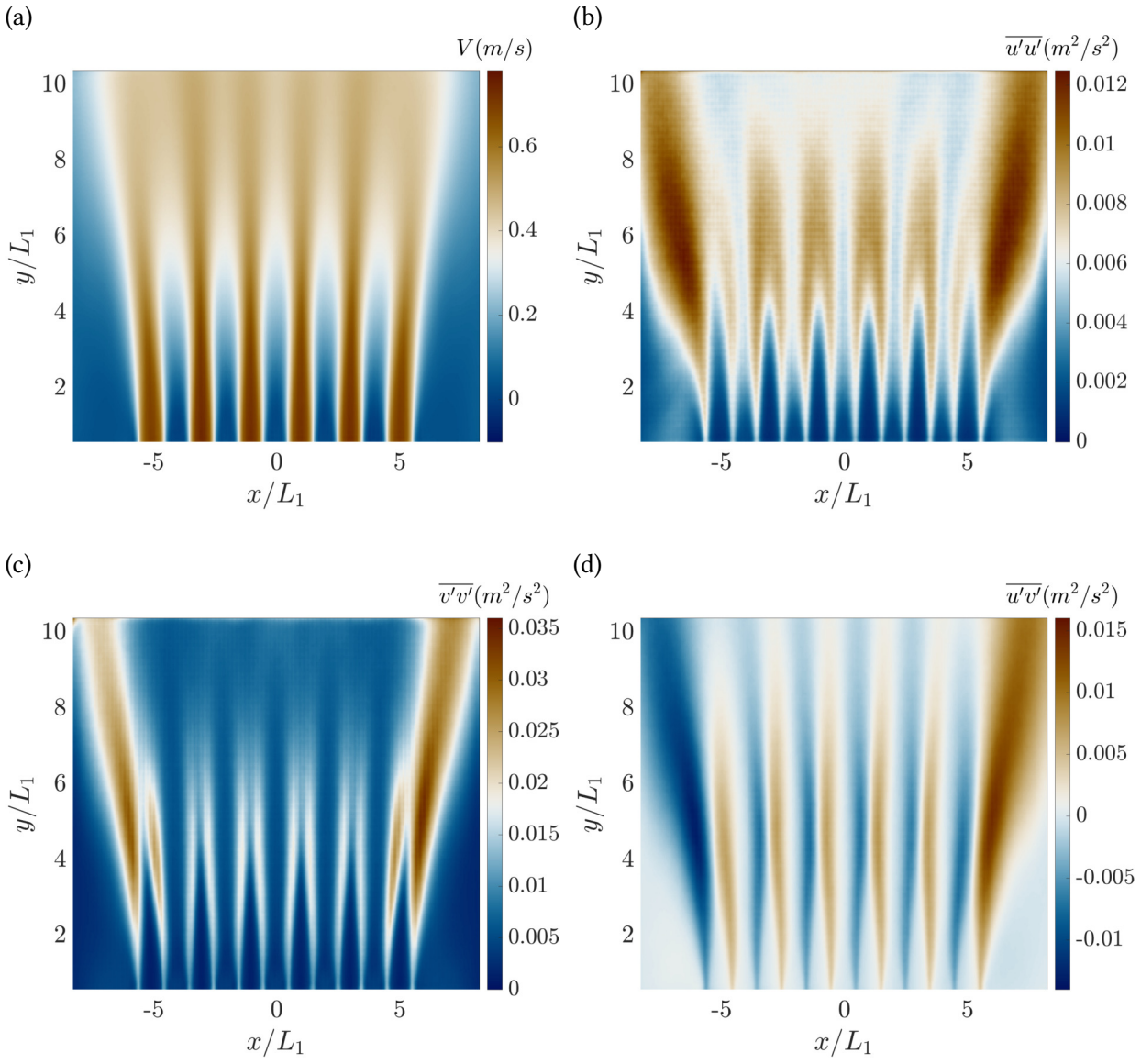

Figure 3.7: PIV results from experiment P1: a) Mean streamwise velocity V; and Reynolds stresses: b) $\overline{u'u'}$; c) $\overline{v'v'}$; d) $\overline{u'v'}$.

3.3.3 Convergence of Time-Averaged Statistics

In this section, we investigate the statistical convergence of the mean velocities and Reynolds stresses in two ways: by random sampling m velocity vectors from the complete time-series (at a given location) to compute the time-averages, and by averaging m velocity vectors from the initial recording time. The convergence plots of the mean streamwise velocity and Reynolds stresses with a range of $\pm 5\%$ of the converged values are provided in Figure 3.8. In these plots, the results

from random sampling are labeled as “Random” (black curves) and from the continuous averaging as “Continuous”(red curves). The “Converged” blue curves are the final values obtained by using all the vector fields available. Continuous averaging is what is often used in the computational community to indicate convergence of averaged quantities. This can provide the means to explain the rate of convergence as well as the magnitude of the contributions over time; however, the curves from random sampling represent the spread of the quantity of interest. For example, the spread of the mean streamwise velocity (Figure 3.8a) is narrower than that of the Reynolds stresses (e.g., Figure 3.8b). This indicates that the Reynolds stresses are more sensitive to variations in the flow, and that a larger number of samples are needed to calculate the Reynolds stresses compared to the mean velocities. For example, as shown in Figure 3.8a, with about 20% of the samples, the variation about the “Converged” value is approximately one percent; however, these variations are about three to four percent for the Reynolds stresses with the same number of vector fields used.

The verification of the convergence of statistical quantities is very important to ensure that the results are independent of the number of images obtained, and it should become common practice in the experimental community. This brief description of convergence was made to point out its importance in the uncertainty of PIV results. However, convergence does not imply accuracy in the results. For example, if the laser plane of the PIV system is slightly misaligned, and you capture the same number of images, the results will still converge, but to a different value. For this reason, it should become common practice to repeat the experiments on separate occasions to ensure that the measurements are reliable. In Section 3.3.5, some common issues with the reproducibility of PIV data including laser misalignment.

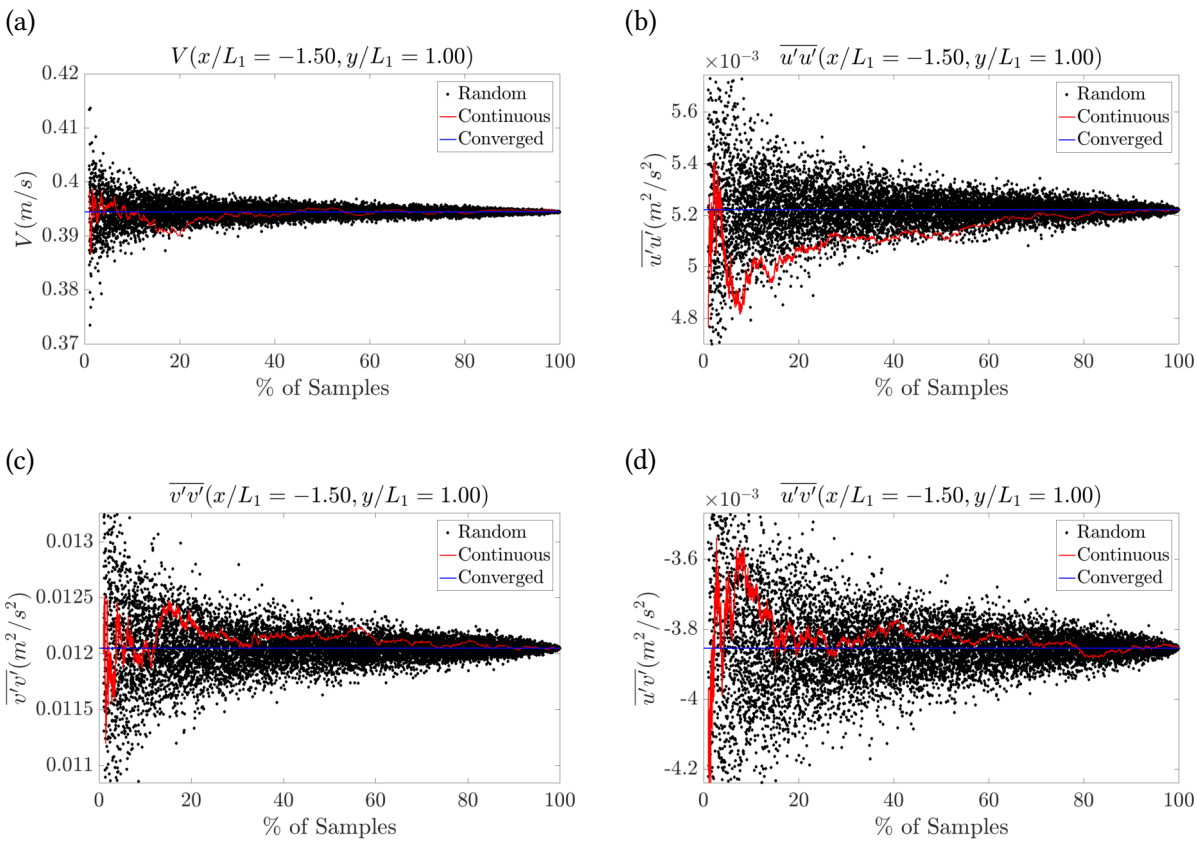

Figure 3.8: Convergence plots from experiment P1: a) Mean streamwise velocity V; and Reynolds stresses: b) $\overline{u'u'}$; c) $\overline{v'v'}$; d) $\overline{u'v'}$.

3.3.4 Quantifying the Repeatability and Reproducibility of Separate Measurements

There are several ways to quantify the differences between separate measurements. The relative differences can be calculated locally, over a line, or as an integral value for each measurement. Each of these methods might be preferred for different reasons, but to calculate the relative differences in the profiles along several streamwise locations, we calculate a vector norm of the difference between the profiles of separate measurements. We want to note that in the calculation of the relative difference of two profiles, some regions of the profiles will contribute more than others, and to penalize the large differences more than the small differences, we use the L2-norm.

Vector norms provide a bound on the magnitude of the vector and are calculated by

$$\|\boldsymbol{z}\|_p = \left[\sum_{i=1}^{n} |z_i|^p\right]^{\frac{1}{p}}, \tag{3.8}$$

where $\boldsymbol{z}$ is a vector, z_i is the ith element in the vector, n is the total number of elements, and p is the order of the vector norm.

For a value of $p = 2$, this expression is known as the L2 norm which is used to measure the length of the input $\boldsymbol{z}$ vector. If $\boldsymbol{z}$ is defined as the difference between two vectors $(\boldsymbol{z} - \hat{\boldsymbol{z}})$ a quantitative measure of the differences between the two can be obtained by:

$$\|\boldsymbol{z} - \hat{\boldsymbol{z}}\|_2 = \left[\sum_{i=1}^{n} |z_i - \hat{z}_i|^2\right]^{\frac{1}{2}}. \tag{3.9}$$

This form of the L2-norm is nothing more than the root-mean-square error times a factor of $\sqrt{n}$. Furthermore, if $\boldsymbol{z}$ is the reference data, and $\hat{\boldsymbol{z}}$ is an approximation, the relative error/difference in $\hat{\boldsymbol{z}}$ can be calculated by:

$$\frac{\|\boldsymbol{z} - \hat{\boldsymbol{z}}\|_2}{\|\boldsymbol{z}\|_2} = \sqrt{\frac{\sum_{i=1}^{n} |z_i - \hat{z}_i|^2}{\sum_{i=1}^{n} |z_i|^2}}. \tag{3.10}$$

To quantify the repeatability of and reproducibility of separate measurements, we plotted the results of each measurement and calculated the relative L2-norm (relative to P1) using Equation 3.10. To test the repeatability of the PIV measurements, we first focused on the plots and relative difference of measurements of P2 and P3 (measurements with the Pulsed laser). The P2 measurement was conducted a day after P1, without making any changes to the PIV setup and using the same calibration image as P1. The only changes that were made were to regulate the flow rate by adjusting valves and the pump's frequency drives. In this manner, we tested if we could replicate the results of experiment P1 by avoiding changing the alignment of the PIV system. These two experiments were recorded with an acquisition frequency of $10\ Hz$ for a total of 30 minutes. The mean streamwise velocity profiles of the four experiments (P1-Blue, P2-Red, P3-

Black, and CW-Green curves) without and with uncertainty bands are shown in Figures 3.9a and 3.9b, respectively. These profiles show very good agreement at these axial locations; however, some portions of the profiles exhibit larger variations than others. For this reason, we refer to the relative differences over the whole profile. As shown in Table 3.4, the relative difference for the profiles of P2, range between 1 and 2%. Even though this is a very simple test, this result demonstrates that even in the best-case scenario (without changing the laser alignment), slight variations in the measurements exist.

Furthermore, the results of experiment P3, in which the PIV system was taken down and realigned on a different day, also show very good agreement with experiment P1; however, the relative norms are larger (between 2 and 7%), especially at $y/L_1 = 1$. While the differences are larger, they still fall under 5% on average for the different axial locations. Last but not least, to check if the experimental results are reproducible with a different laser system, we take a look at the results obtained with a CW laser (green curves). Here too, the relative differences between the measurements indicate that the results are reproducible with a different laser system. Overall, from these few experiments, the repeatability and the reproducibility of the measurements appears to be reasonably good. However, we note that by making changes to the setup (whether it is the position of the laser or the laser system itself), the level of uncertainties observed are larger. One important feature to note is that while the relative differences are larger, the profiles generally fall within the uncertainty bands, as shown in Figure 3.9b. Despite the fact that these differences are captured by the uncertainty bands, they must be accounted for when providing PIV results.

Table 3.4: Relative L2-Norm (%) of the mean streamwise velocity for profiles at several streamwise locations.

$y/L_1 =$	1	2	3	4	5	6	7	8	Average
P2	1.72	1.22	1.17	1.38	1.62	1.70	1.51	1.22	1.44
P3	6.23	4.88	3.98	3.49	2.77	2.73	2.52	2.36	3.62
CW	7.36	6.32	5.48	4.98	3.72	3.15	2.66	2.31	4.50

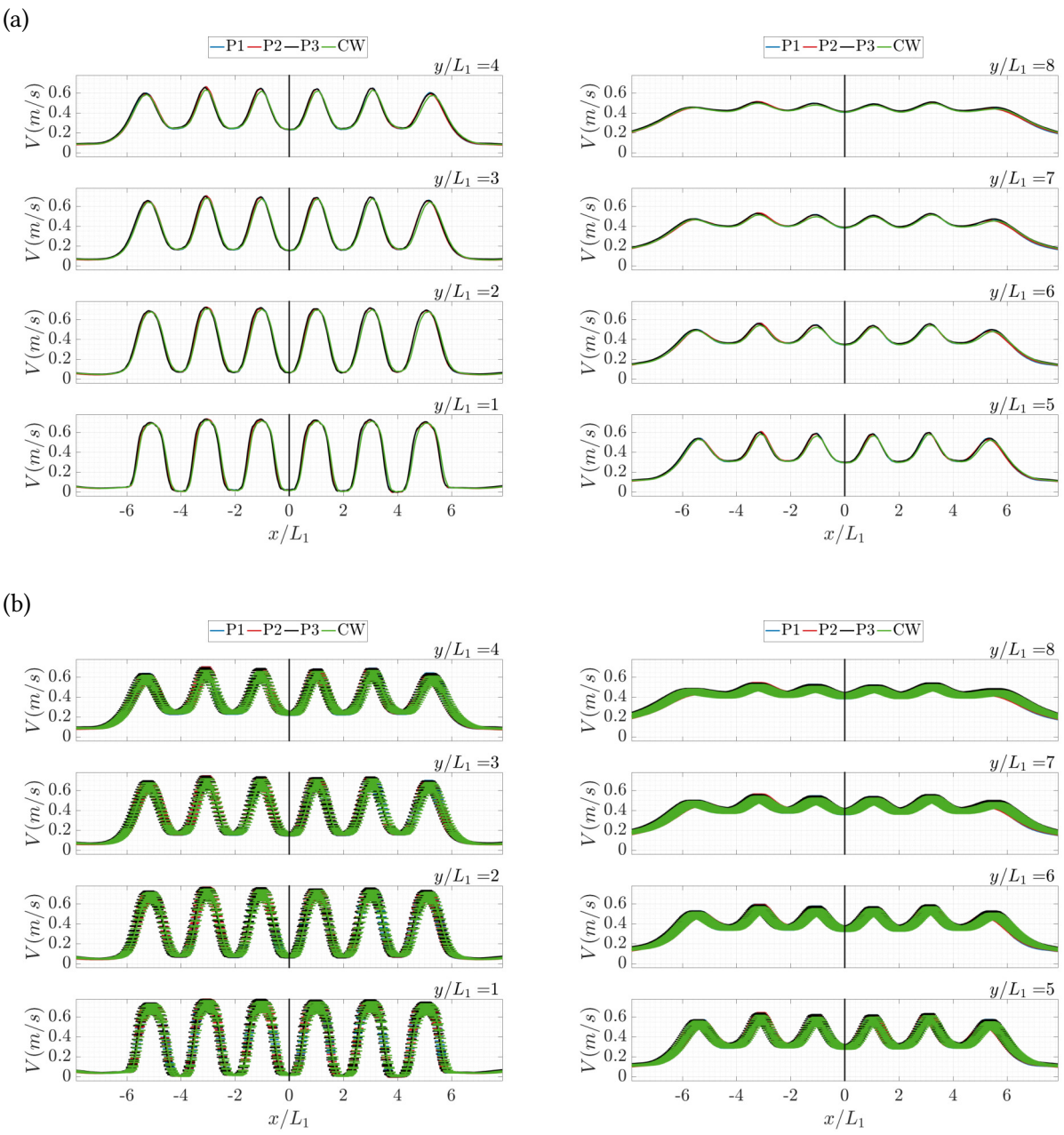

Figure 3.9: Streamwise mean velocity profiles for experiments P1, P2, P3, and CW: a) Without uncertainty bands; b) With uncertainty bands.

In the same manner, we compare the Reynolds stresses. The plots of the Reynolds normal stresses $\overline{u'u'}$ and $\overline{v'v'}$ are shown in Figures 3.10 and 3.11, respectively. From the profiles of the Reynolds normal stresses without the uncertainty bands (Figures 3.10a and 3.11a), we notice that the differences between experiments are larger than those of the mean velocity profiles. In the

profiles without the uncertainty bands, the differences between the plots are clear; however, in the plots with the uncertainty bands, there is a lot more overlap between the results, especially in the $\overline{v'v'}$ profiles. The $\overline{u'u'}$ profiles of the CW laser are notably larger in magnitude compared to those of the pulsed laser, but there are some regions of overlap with the uncertainty bands. On the other hand, the $\overline{v'v'}$ profiles of the CW laser are in very good agreement with and without the uncertainty bands.

The relative differences between the profiles of the normal stresses are given in Tables 3.5 and 3.6. Since the Reynolds stresses are higher order statistics, the relative differences of $\overline{u'u'}$ and $\overline{v'v'}$ for the experiments P2 and P3 are, on average, larger than those of the mean velocities (4 to 8%). These larger variations are in agreement with findings discussed in Section 3.3.3, where larger variations between different measurements were observed in the convergence plots of the Reynolds stresses. The more prominent differences occur with the CW results, which are least twice as large (16.18% and 11.05% on average) compared to those of the velocity measurements (4.5% on average). Therefore, the Reynolds stresses are significantly more different between separate measurements on average, even when the same equipment is used.

Table 3.5: Relative L2-Norm (%) of the Reynolds normal stress $\overline{u'u'}$ for profiles at several streamwise locations.

$y/L_1 =$	1	2	3	4	5	6	7	8	Average
P2	5.24	3.79	3.34	4.44	3.87	3.54	3.25	3.16	3.83
P3	11.24	6.81	4.70	5.18	5.05	6.54	6.38	6.12	6.50
CW	32.39	26.73	18.91	12.86	10.21	7.30	8.69	12.38	16.18

Table 3.6: Relative L2-Norm (%) of the Reynolds normal stress $\overline{v'v'}$ for profiles at several streamwise locations.

$y/L_1 =$	1	2	3	4	5	6	7	8	Average
P2	5.60	5.36	5.95	6.33	5.91	5.69	5.21	5.60	5.71
P3	14.52	10.80	8.52	7.37	5.89	5.88	5.64	5.14	7.97
CW	18.87	15.68	12.79	10.58	8.13	7.70	7.48	7.16	11.05

Last but not least, the plots of Reynolds shear stresses and their respective relative differences

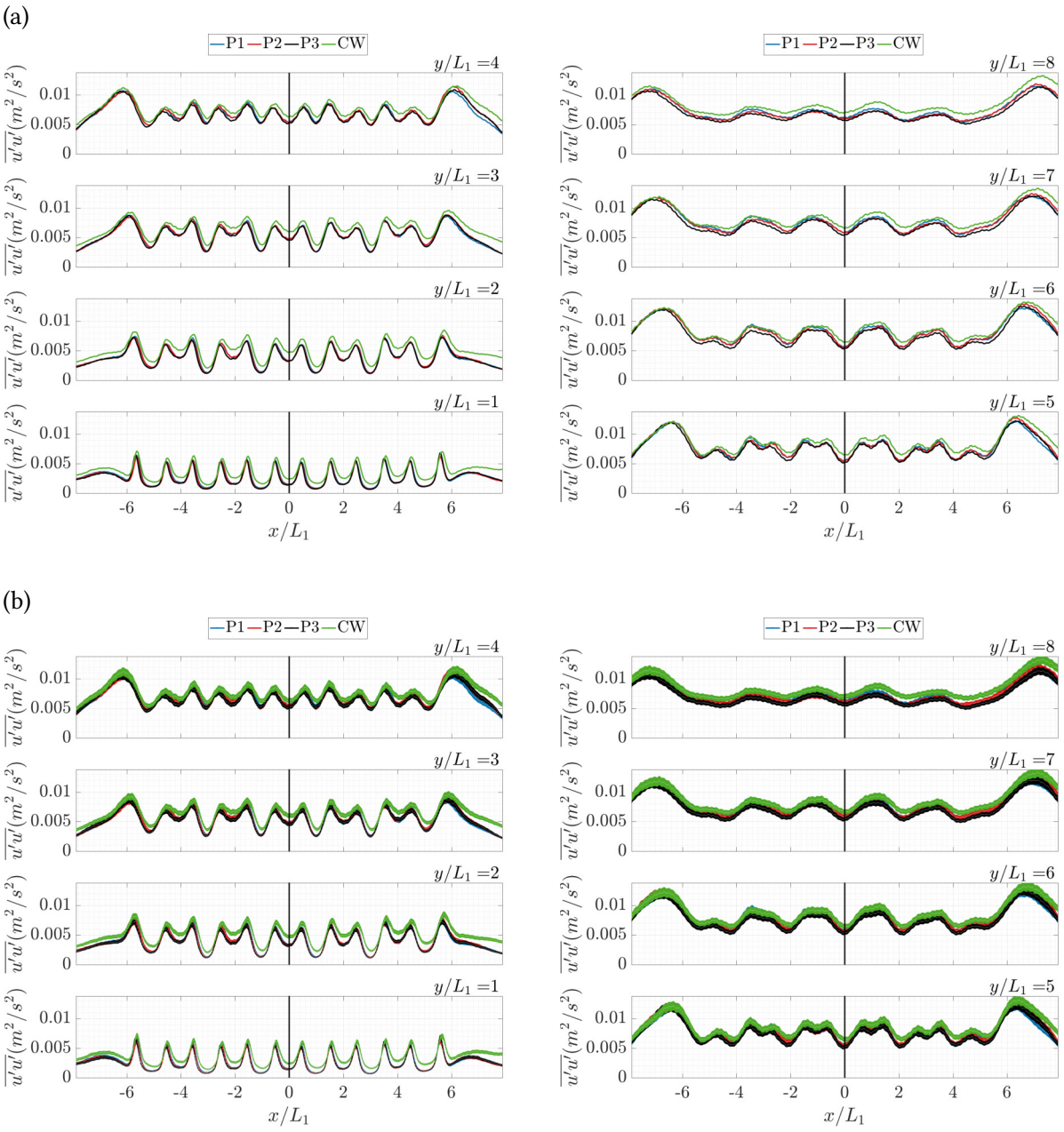

Figure 3.10: Reynolds normal stress $\overline{u'u'}$ profiles for experiments P1, P2, P3, and CW: a) Without uncertainty bands; b) With uncertainty bands.

are given in Figure 3.12 and Table 3.7, respectively. For this case, the relative differences also remain in the same range as the normal stresses on average, with the exception of the comparison with P2, where the differences increased to 8%. As the reader may note, the profiles of the shear stresses for the different experiments appear nearly identical; however, the relative differences

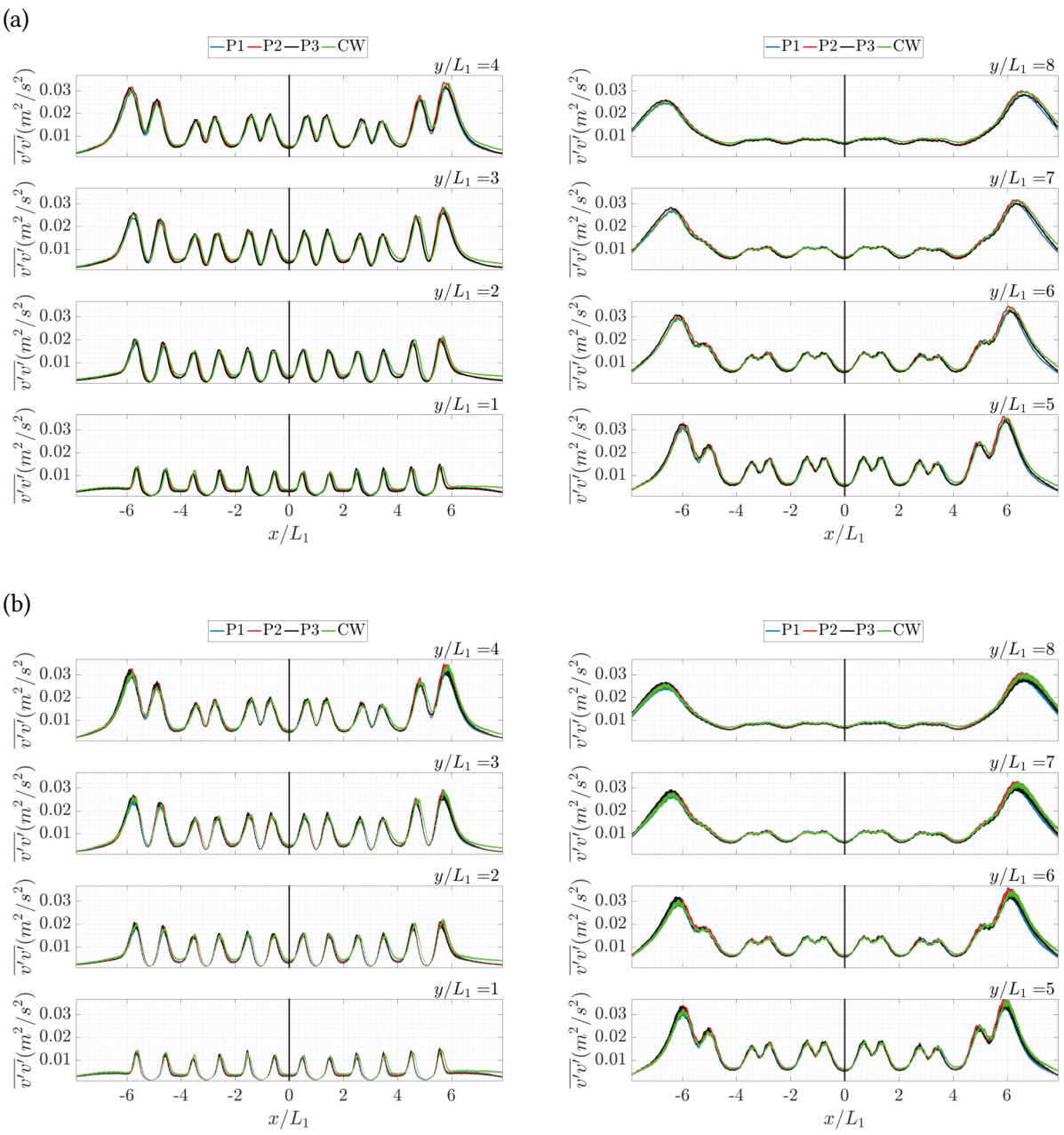

Figure 3.11: Reynolds normal stress $\overline{v'v'}$ profiles for experiments P1, P2, P3, and CW: a) Without uncertainty bands; b) With uncertainty bands.

indicate otherwise. This implies that the differences not only arise from the variations in magnitudes at the given locations, but also from small spatial offsets (in the order of 0.1mm) in the measurements caused by small differences between alignments of different measurements.

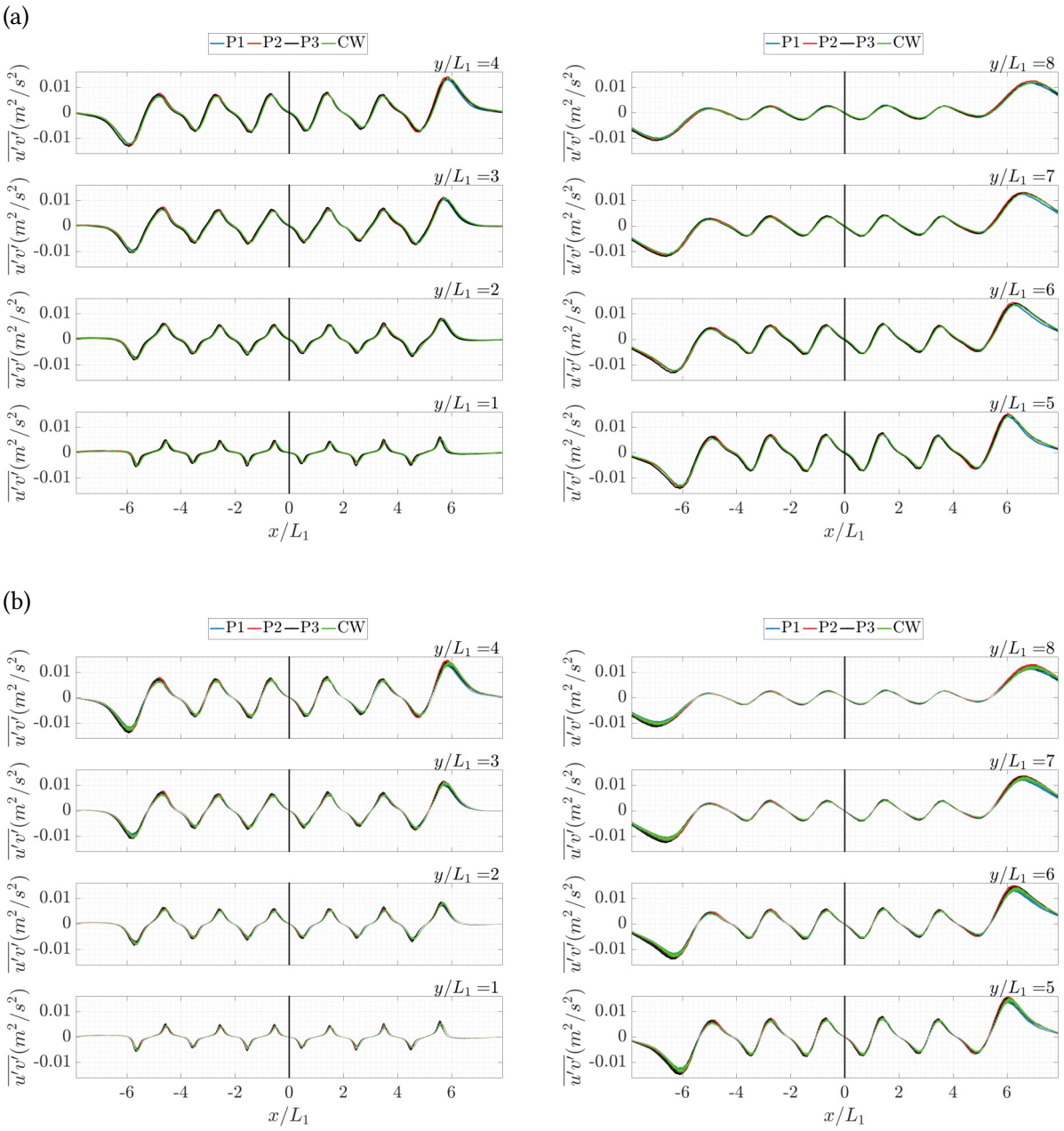

Figure 3.12: Reynolds shear stress $\overline{u'v'}$ profiles for experiments P1, P2, P3, and CW: a) Without uncertainty bands; b) With uncertainty bands.

Table 3.7: Relative L2-Norm (%) of the Reynolds normal stress $\overline{u'v'}$ for profiles at several streamwise locations.

$y/L_1 =$	1	2	3	4	5	6	7	8	Average
P2	7.84	7.62	8.19	8.24	7.73	8.64	8.14	8.91	8.16
P3	25.15	16.16	12.99	11.77	10.17	9.83	8.21	7.56	12.73
CW	21.72	15.85	12.53	12.11	10.31	9.98	8.75	7.90	12.39

3.3.5 Common Issues with the Reproducibility of PIV Data

In this section, we mention a couple of common issues that may affect the reproducibility of PIV data. One common issue that might be encountered, especially when dealing with large regions of interest, is having a slight laser misalignment. While the extent to which this might be a problem is facility dependent, it could cause under- or over-estimation of the quantities of interest. To illustrate this, we ran a CFD simulation of this facility, in which we compare the velocity profiles at locations offset from the midplane (where the measurements were taken). Figure 3.13 shows the velocity profiles to illustrate the laser misalignment of up to $6\ mm$. We would like to note that while a 6mm misalignment could be too exaggerated for this facility, it is certainly not too exaggerated for larger facilities. Here, the largest differences occur in the inner shear layers (between jets). If the laser were misaligned by $6\ mm$, the local relative differences in the mean velocities could lead to 20-30% disagreements in the inner shear layer regions. However, these effects are not as dominant in the jet core regions, where we observe up to a 1% difference (locally) in the mean velocity.

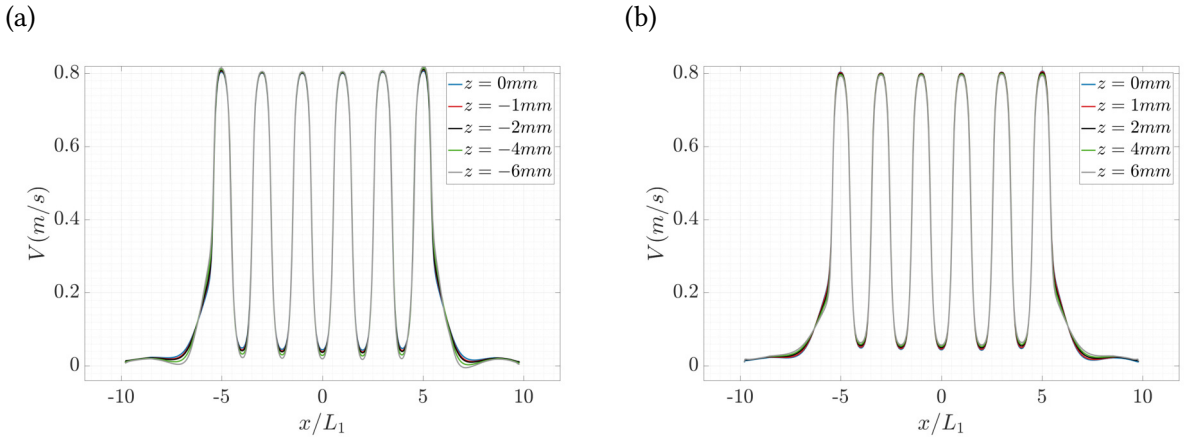

Figure 3.13: Effects from laser misalignment on the mean velocity profiles: a) closer and b) farther away from the front of the facility. Note: all profiles are for $y/L_1 = 1$.

To further illustrate this issue, we misaligned the laser sheet in one the experiments by two millimeters and took one measurement. The velocity profiles for the misaligned PIV measurement (P4, gray curve) are shown in Figure 3.14. In Figure 3.14a, we observe large differences in the

velocity profiles in the inner shear regions; however, smaller yet noticeable differences occur in the jet core regions. When the uncertainty bands are included, as shown in Figure 3.14b, some regions, especially those in between the jets are not covered by the uncertainty bands. While these profiles do not appear much different from those shown in Figure 3.9b, these results could certainty lead to different conclusions about the flow characteristics. For example, the location of the merging regions could be under- or over-predicted.

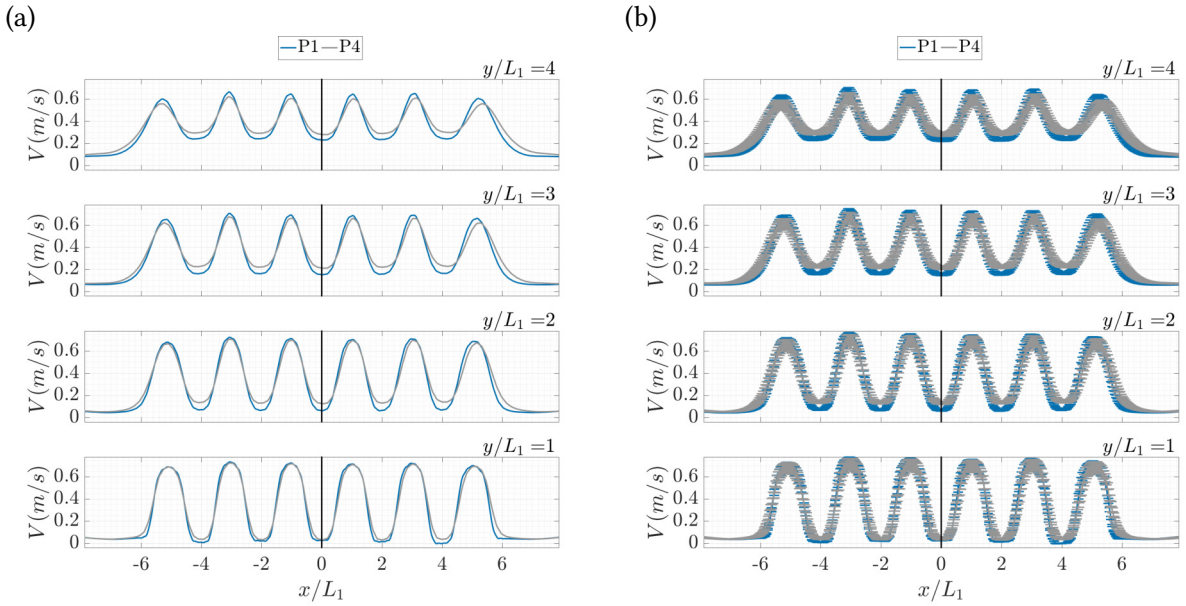

Figure 3.14: Mean velocity profiles from measurement with laser misalignment: a) Without, and b) With uncertainty bands.

Another parameter that can contribute to discrepancies in PIV measurements are fluctuations in fluid temperature. First, differences in the temperatures can lead to variations of the fluid properties, and hence the Reynolds numbers. For example, we can focus on the differences between measurements P1 and P4, where we observe a temperature difference of about 5 °C. With this temperature difference, the changes in density are less than 1%, but the changes in dynamics viscosity are about 14%. This could lead to some differences in the flow structures for low Reynolds numbers, where viscous effects are dominant. While the differences in viscosities are about 14% with water, the differences could be larger for other fluids. Furthermore, variations in tempera-

tures can lead to larger uncertainties in PIV measurements when different fluids are being mixed. Small changes in temperatures lead to significant differences in index of refraction between the two fluids. This leads to unsuitable focus of the seeding particles, and therefore, large discrepancies in the measurements. These examples illustrate the importance of monitoring the fluid properties to understand the possible sources of uncertainties between different measurements. While the changes in fluid properties do not cause significant changes in the flow fields, they should be monitored and become part of the standard guidelines when generating experimental databases for CFD .

3.3.6 Evaluation of RANS Models

The intrinsic variations between separate PIV measurements were discussed in Section 3.3.4. This type of verification is necessary when developing a CFD-grade database. In this section we provide a brief evaluation of RANS-based models to illustrate how the acquired data can be used to gain an insight for further code development. For simplification, we conduct our evaluations for the two jet configuration.

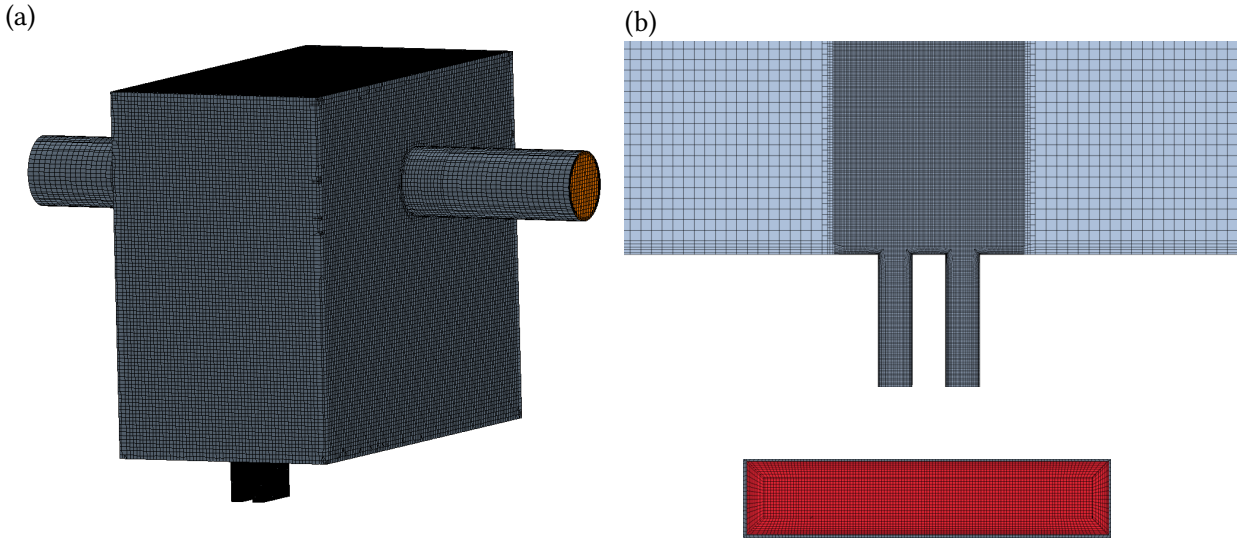

Figure 3.15: CADs of the RCCS facility: a) Complete geometry; b) Mesh cross-sections (midplane of jets and inlet).

RANS simulations were carried out in Siemen's STAR-CCM+ 12.06. The mesh used for the

simulations in this chapter is shown in Figure 3.15. This mesh consists of 7.7 million hexahedron cells. To save computational resources without compromising the results, the regions covering the jets' path consist of smaller cells (fine region) than those everywhere else (coarse region). The cells sizes were $0.039L_1$ in the fine region and $0.31L_1$ in the coarse region. The simulations executed were unsteady simulations. The grid resolution was determined based on the convergence of the time-averaged Reynolds stresses. Convergence of the time-averaged Reynolds stresses was also used for the time convergence studies. Through time step convergence studies, a time step of 0.1 seconds was regarded as a sufficiently small time for these simulations. A fully developed velocity boundary condition was imposed at the inlet, a pressure outlet at the outlet, and non-slip walls at all the walls. The RANS models that were tested are the Reynolds Stress Model (RSM) with Elliptic Blending, and the Realizable (Real.) and the Standard (Std.) $k\epsilon$ models with the linear eddy viscosity model. For these simulations, the following STAR-CCM+ submodels were chosen: an implicit unsteady solver, all y+ wall treatment, gravity, exact wall distance, turbulent, constant density, gradients, segregated flow, liquid, and three dimensional. Furthermore, the default model coefficients provided by STAR-CCM+ were used for these simulations.

Cell quantity data was extracted from the simulations for our analyses. The results from a total of 800 seconds were time-averaged for our comparisons. A comparison between the RANS and PIV mean streamwise velocity profiles is provided in Figure 3.16. The PIV data consists of one experiment with a pulsed (P) and another with a continuous wave (CW) laser. At regions near the inlet ($y/L_1 = 1$), the jet behavior is well captured except in the vicinity the jet core ($x/L_1 = \pm 1$). At all streamwise locations, the jets' centerline velocities are over-predicted by the RANS simulations, with the largest over-prediction given by the RSM model and the smallest by the Std. $k\epsilon$ model. In the experiments, the rate of decay of the centerline velocity occurs shortly after the departure from the inlet; however, the simulations indicate almost no decay in the centerline velocity.

The Reynolds normal stresses $\overline{u'u'}$ and $\overline{v'v'}$ are shown in Figures 3.17 and 3.18, respectively. The $\overline{u'u'}$ profiles show significant differences in the profiles across all streamwise locations. At

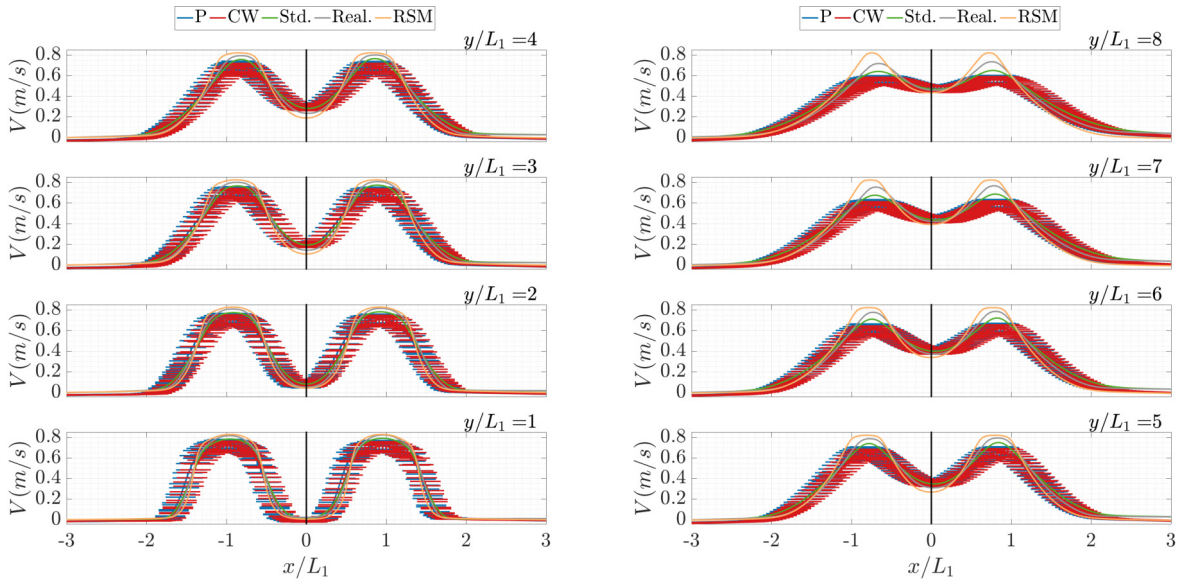

Figure 3.16: Comparison between experimental and simulation results. Streamwise velocity V at various streamwise locations y/L_1.

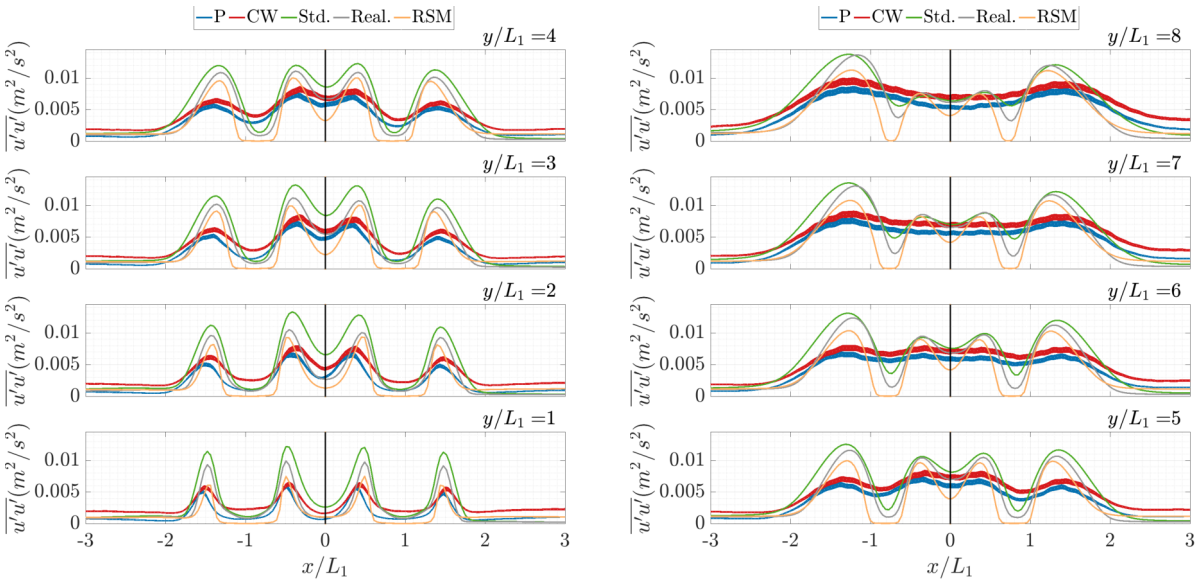

Figure 3.17: Comparison between experimental and simulation results. Reynolds normal stress $\overline{u'u'}$ at various streamwise locations y/L_1.

the inner ($x/L_1 = \pm 0.5$) and outer ($x/L_1 = \pm 1.5$) shear layers, $\overline{u'u'}$ is over-predicted by these simulations; however, at the jets' centerlines ($y/L_1 = \pm 1$), the models under-predict $\overline{u'u'}$, with the RSM model under-predicting the the most. In the work by Li et al. [64], discrepancies between the shapes of the profiles also occur; however, they encountered that the Realizable $k\epsilon$

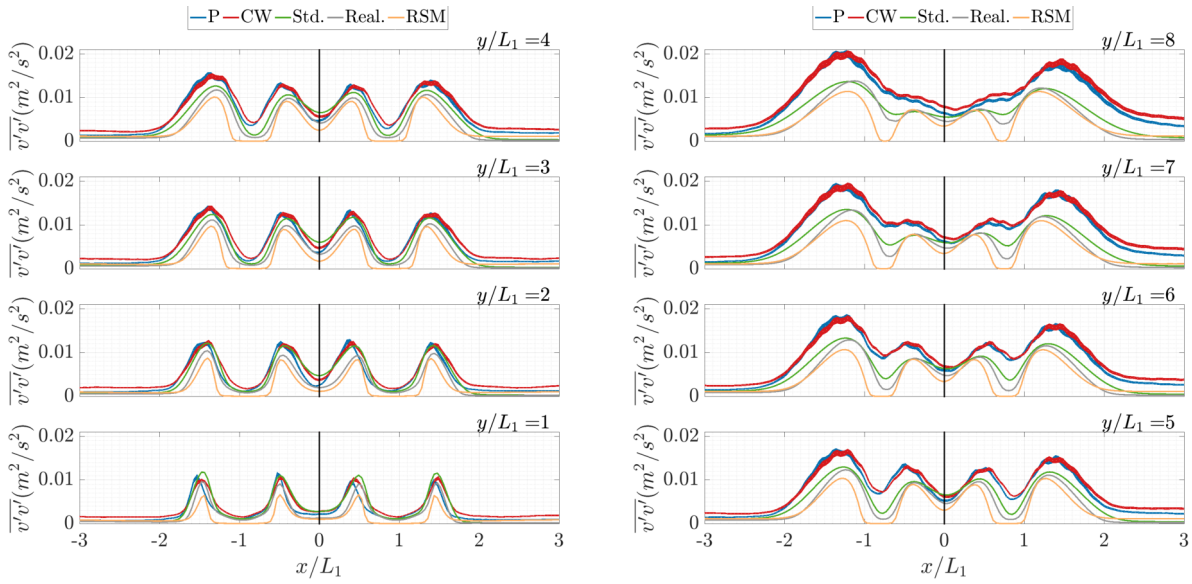

Figure 3.18: Comparison between experimental and simulation results. Reynolds normal stress $\overline{v'v'}$ at various streamwise locations y/L_1.

model over-predicts the $\overline{u'u'}$ profiles at all streamwise locations. Furthermore, in our case, the RANS simulations under-predict $\overline{u'u'}$ at the symmetry plane $x/L_1 = 0$ at several streamwise locations. These observations are in agreement with the findings by Anderson and Spall [21], where they observed an under-prediction of the cross-stream component of the normal stresses at the symmetry plane ($x/L_1 = 0$) by the RSM model.

In the $\overline{v'v'}$ profiles, the magnitude of the profiles from the RANS simulations are in good agreement with the experiments for $y/L1 \leq 4$. At these locations, the RSM model tends to under-predict the profiles the most at the jets' centerlines as well. For locations $y/L_1 \geq 5$, the trends in the profiles from the RANS models become significantly different. In the experiments, the rate of increase of $\overline{v'v'}$ is larger for the experiments in the outer shear layers, while the decay in the inner shear layers is slower than in the RANS simulations. These are the opposite observations made by Li et al. [64]. In their comparisons, they showed larger discrepancies between the profiles near the inlet, while in our comparison, we observe relative good agreement at these locations. On the other hand, the work by Anderson and Spall [21] indicated good agreement of the streamwise stresses at the symmetry plane, which also agrees with our observations. Lastly, Figures 3.19 shows the comparison between the Reynolds shear stresses. These profiles show

very good agreement between the experiments and simulations at all axial locations. The better agreement in the shear stress profiles was also observed by Li et. al [64], regardless of the larger discrepancies observed in the normal stresses. This behavior could be caused by the inadequate redistribution of energy along the streamwise and cross-stream directions. Furthermore, these discrepancies could be attributed to differences in the geometry, specially the jet spacing to jet width ratio S/L_1, and differences in the Reynolds number, which will require further investigation.

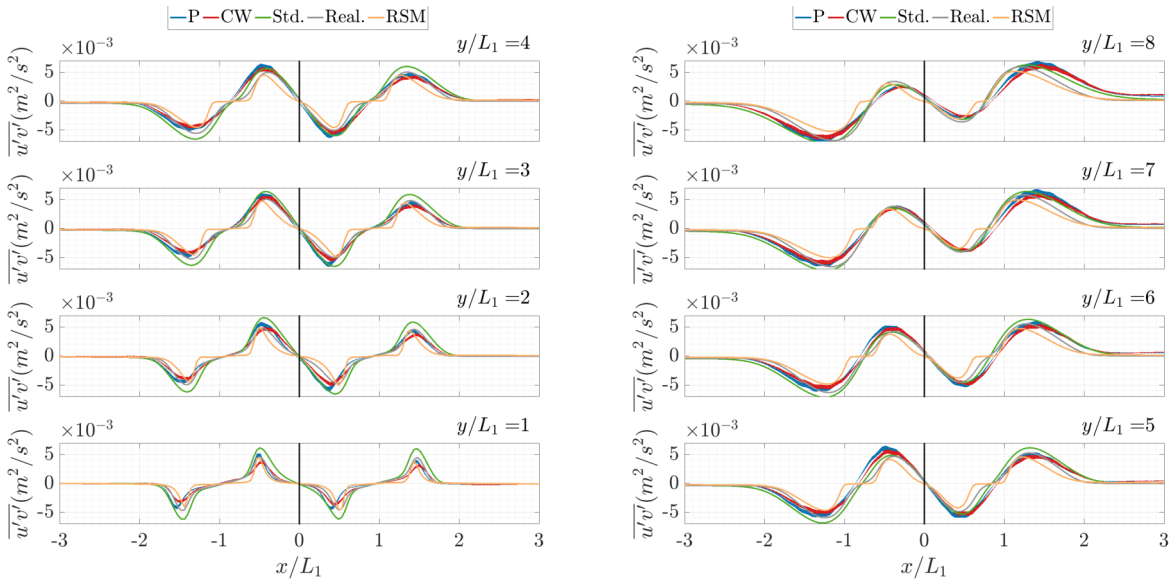

Figure 3.19: Comparison between experimental and simulation results. Reynolds shear stress $\overline{u'v'}$ at various streamwise locations y/L_1.

The over- and under-prediction of both normal stresses are indications of the incorrect prediction TKE and possibly the incorrect redistribution of energy along each direction. The observed discrepancies in these profiles are the causes for the over-prediction of the streamwise velocity at the jets' centerlines. To investigate the over- and under-prediction of the TKE, we inspect the rate of production of TKE due to shear G_k. In the TKE equation, this term is often expressed as

$$G_k = -\overline{u_i' u_j'} \frac{\partial U_i}{\partial x_j}. \tag{3.11}$$

For planar measurements, the contributions can be written as follows:

$$G_k = -\overline{u'u'}\frac{\partial U}{\partial x} - \overline{v'v'}\frac{\partial V}{\partial y} - \overline{u'v'}\left(\frac{\partial U}{\partial y} + \frac{\partial V}{\partial x}\right). \tag{3.12}$$

The profiles of the turbulence shear production G_k are provided in Figure 3.20. Here, G_k is well predicted by the simulations at the symmetry plane ($x/L_1 = 0$), while it is over-estimated by all models in the inner ($x/L_1 = \pm 0.5$) and outer ($x/L_1 = \pm 1.5$) shear layers. The over-prediction of G_k at those locations are the reasons for the narrowing of the jet width seen in the mean velocity profiles. On the other hand, at the jets' centerlines, the magnitude of the profiles are in reasonable agreement with the experiments (considering the shifts in the location of the centerlines). Because of the good agreement in the magnitude of G_k between the simulations and experiments, and because the magnitude of the mean velocity profiles are predicted incorrectly at the jets' centerlines, we speculate that the third velocity component is responsible for the lack of decay in the mean velocity at the jet centerlines. Through investigations of the sources of TKE, we can gain physical insight into which models contribute to the under- or over-prediction of certain flow fields, and investigations like this could provide the basis for future explorations.

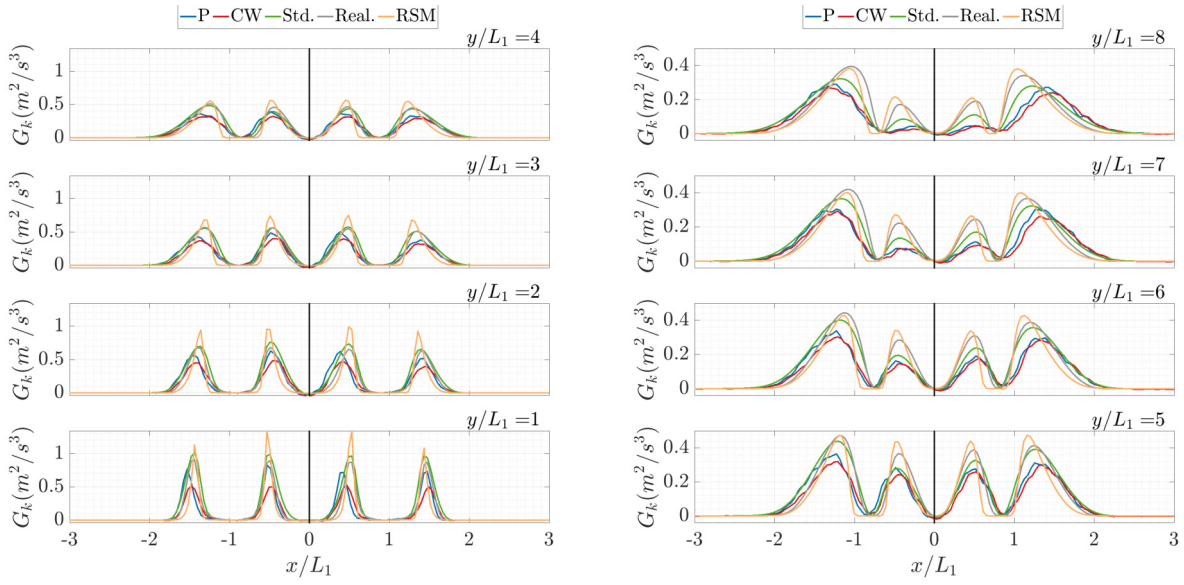

Figure 3.20: Comparison between experimental and simulation results. Shear production of TKE G_k at various streamwise locations y/L_1.

3.4 Time-Resolved Measurements

In the previous sections, PIV measurements with relative low sampling rates were used to extract time-averaged quantities, representative of the mean flow field. In this Section, we discuss the results obtained with time-resolved PIV measurements characterized by high spatial and temporal resolution. These measurements are suitable for frequency analyses and the investigation of fast evolving time dynamics. The experimental data on the time-resolved flow fields are analyzed through PSD and SPOD methods described in Sections 1.2.2.3 and 1.2.2.4, respectively.

3.4.1 Test Matrix

Time-resolved experimental PIV data of two, four, and six jets with jet Reynolds number $Re = 13,800$ were obtained in the RCCS facility. The experiments were also conducted at constant-density conditions utilizing tap water with a temperature of 21°C. The flow fields consisted of recordings acquired at a sampling frequency of $400\ Hz$. Due to the limitations of our acquisition equipment at this frequency, multiple short recordings were combined to capture several realizations of the flow fields. Additional information about the length of the recordings can be obtained in Table 3.8.

Table 3.8: PIV recording information.

	Two Jets	Four Jets	Six Jets
Recording Rate (Hz)	400	400	400
Temperature (°C)	21	21	21
Total Number of Image Pairs Recorded (–)	40,832	30,702	30,296
Length of Short Recordings (s)	6.38	2.74	2.71
Total Length of Recordings (s)	102.08	76.75	75.74

The time-averaged streamwise and cross-stream velocity fields (V, U) for the configurations with two, four, and six jets are shown in Figure 3.21. These velocity fields are also in agreement with the previous measurements discussed in Section 3.2.2. It is important to note that the measurement field of view is not the same for all measurements. This because the fields of view were adjusted to include only the region of interest surrounding the jets and not the areas closer to

the walls of the plenum (i.e. a larger field of view was needed to cover a 6 jet experiments with respect to a 2 jet experiment). Additionally, in Figure 3.21, an outline where the streamwise flow velocity equals half of the nominal inlet velocity $V = \frac{V_0}{2}$ is shown as well, superimposed to the velocity contour plots. This is used to help with the description of the coherent structures in Section 3.4.4.

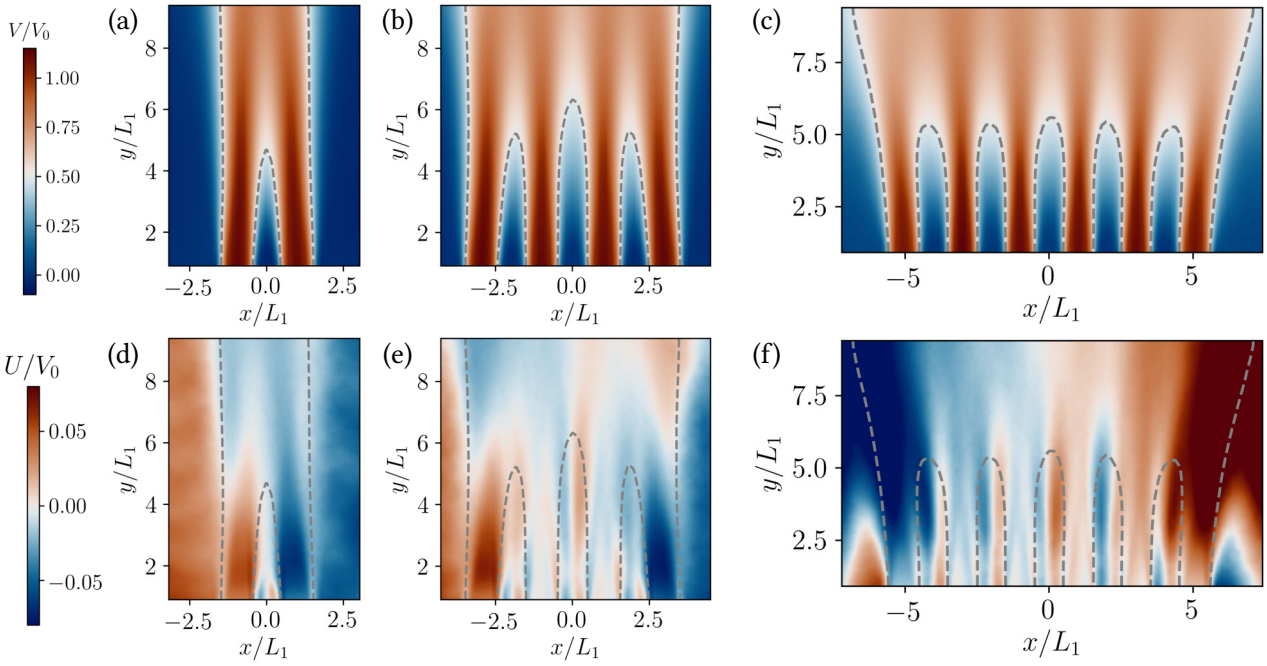

Figure 3.21: Mean streamwise and cross-stream velocity fields (V, U) for different jet configurations: (a,d) Two jets; (b,e) Four jets; (c,f) Six jets. The dashed lines are located where $V = \frac{V_0}{2}$.

3.4.2 PSD Analysis of the Streamwise Velocity Field

We begin the investigation of the flow dynamics through PSD analysis. We first analyze the velocity field in the streamwise direction v of the two-jets experiment, and then we expand our discussions to the cases with four and six jets. The PSDs are calculated for several $(x/L_1, y/L_1)$ locations, and for ease of reference, we have included color-coded pictures indicating these locations for each set of plots. The PSDs at locations $y/L_1 = 1, 4$, and 8 for $x/L_1 = -1.5$ to 1.5 are shown in Figures 3.22(a-c), respectively. Figure 3.22d indicates the locations of investigation for the different y/L_1 distance. Note that the axis of symmetry of the upper plenum is located at

$x/L_1 = 0$, as shown in Figure 3.2a. In Figure 3.22, the brown curve represents the characteristic $-5/3$ slope proposed by Kolmogorov that identifies the inertial subrange [37] of the energy cascade. Furthermore, the black, red, green, blue, and orange curves in each plot of Figure 3.22 correspond to the PSD at different x/L_1 for the given y/L_1. At $y/L_1 = 1$ (Figure 3.22a), no dominant frequencies are apparent, and the power contained at all locations except $x/L_1 = 0$ are similar. One interesting feature is that the overall power contained in the frequency spectrum at $x/L_1 = 0$ is significantly lower than that observed at the other locations.

At $y/L_1 = 4$ (Figure 3.22b), in the locations near the shear layers ($x/L_1 = \pm 0.5$), an increase in the PSD amplitude for $0.35 < St < 0.55$ is observed. The clear peak in the PSD plot indicates the existence of a periodic oscillatory interaction between the two inner shear layers at $St = 0.47$. This observation is in agreement with the investigations by Ko and Lau [59], where they observed pronounced spectral peaks in the inner shear layers. Furthermore, the low pressure region created from the entrainment between the two jets causes the jets to converge, as shown in Figure 3.21(a,d), and induces an oscillatory behavior between the two jets. Conversely, the spectra at the outer shear layers ($x/L_1 = \pm 1.5$) do not exhibit these dominant peaks in the frequency spectrum; however, an increase in the overall amplitudes of the spectra in the lower frequency range is observed. As expected, the PSD indicates that the same general structures are present on the left and right jets (i.e., the spectra at $\pm x/L_1$ locations display the same features). Further downstream from the inlet at $y/L_1 = 8$ (Figure 3.22c), the same peaks at $St = 0.47$ appear, and the same general trends occur: a slight decrease in the magnitude of the peaks and a slight increase in the lower frequency range occurs. From these plots, we can distinguish the areas where the inertial subrange is dominant and follow the $-5/3$ curve. This subrange becomes apparent in the regions further downstream from the jets inlet ($y/L_1 = 4$ and 8) because the structures are formed at the inlet and decay into smaller structures further downstream.

Now we investigate how the PSD varies as the distance along the streamwise direction y/L_1 increases. The plots at $x/L_1 = 0, 0.5, \; and \; 1.5$ are shown in Figure 3.23. Because of the symmetry in our results, we chose to only plot the spectra along the positive x/L_1. In these plots, the brown

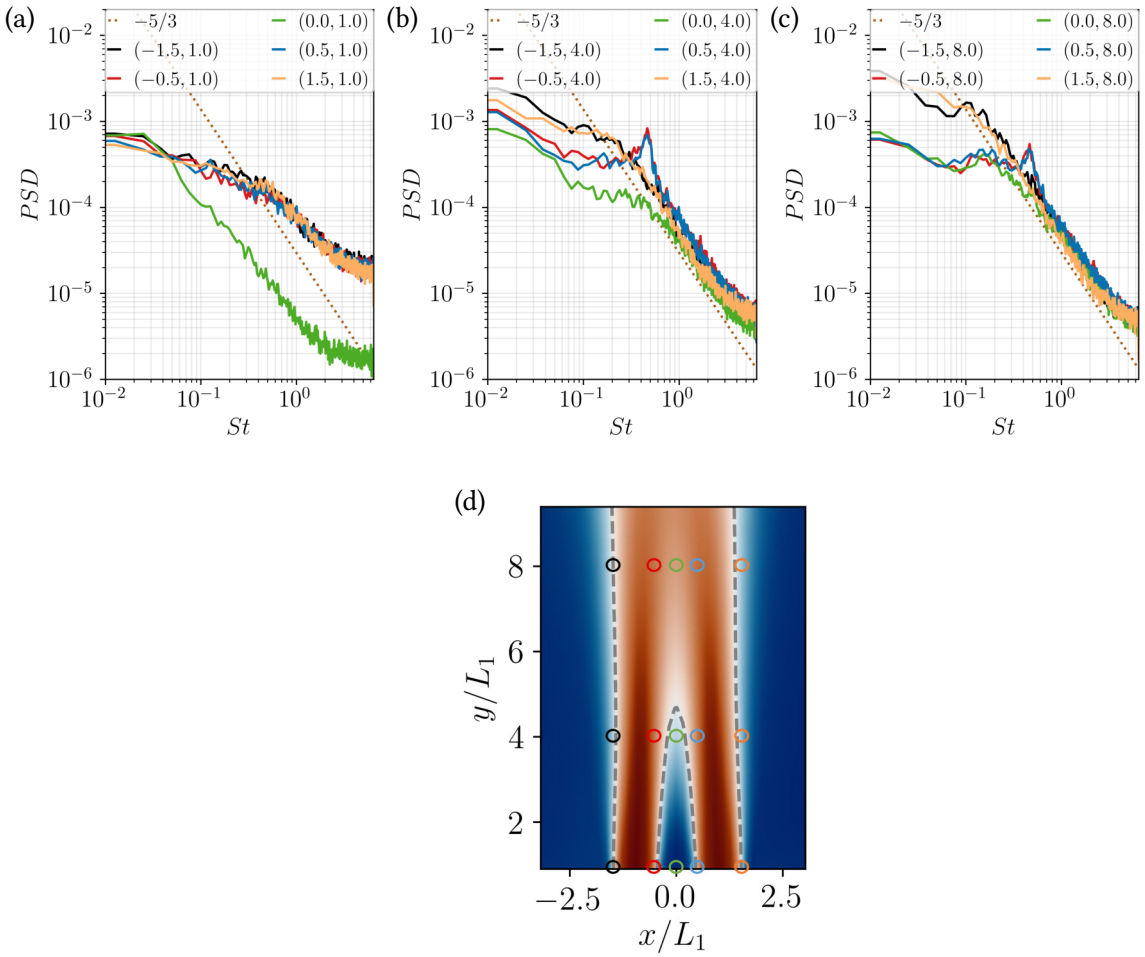

Figure 3.22: Two Jets – PSD of the streamwise velocity $v(t)$ at several $(x/L_1, y/L_1)$ locations: (a) $y/L_1 = 1$; (b) $y/L_1 = 4$; (c) $y/L_1 = 8$; d) Color-coded locations for PSD analysis along the jet flow.

curve is the $-5/3$ Kolmogorov curve, while the black, red, green, blue, and orange curves are the spectra of the velocities at $y/L_1 = 1, 2, 4, 6, \ and \ 8$, respectively. As shown in Figure 3.23a, in the middle of the jets, an increase in the amplitude of the PSD occurs as y/L_1 is increased. This is indicative of the presence of larger length scales in the regions away from the inlet. The curves for $y/L_1 \geq 4$ follow $-5/3$ slope, indicating the presence of the inertial subrange in this region. No strong dominant peaks appear at these locations. At $x/L_1 = 0.5$ (Figure 3.23b), all of the curves, exhibit the same dominant peak at $St = 0.47$; however, the peak at $y/L_1 = 1$ has a lower amplitude compared to the other locations. This lower amplitude in the $St = 0.47$ peak can be associated with the lower level of interactions in the converging region. Moreover, at $x/L_1 = 1.5$

(Figure 3.23c) no dominant peaks were observed. The presence of dominant frequencies in the inner shear layers indicate that there is a strong locking mechanism confined between the parallel jets, and this mechanism is not translated to the outer regions of the shear layer.

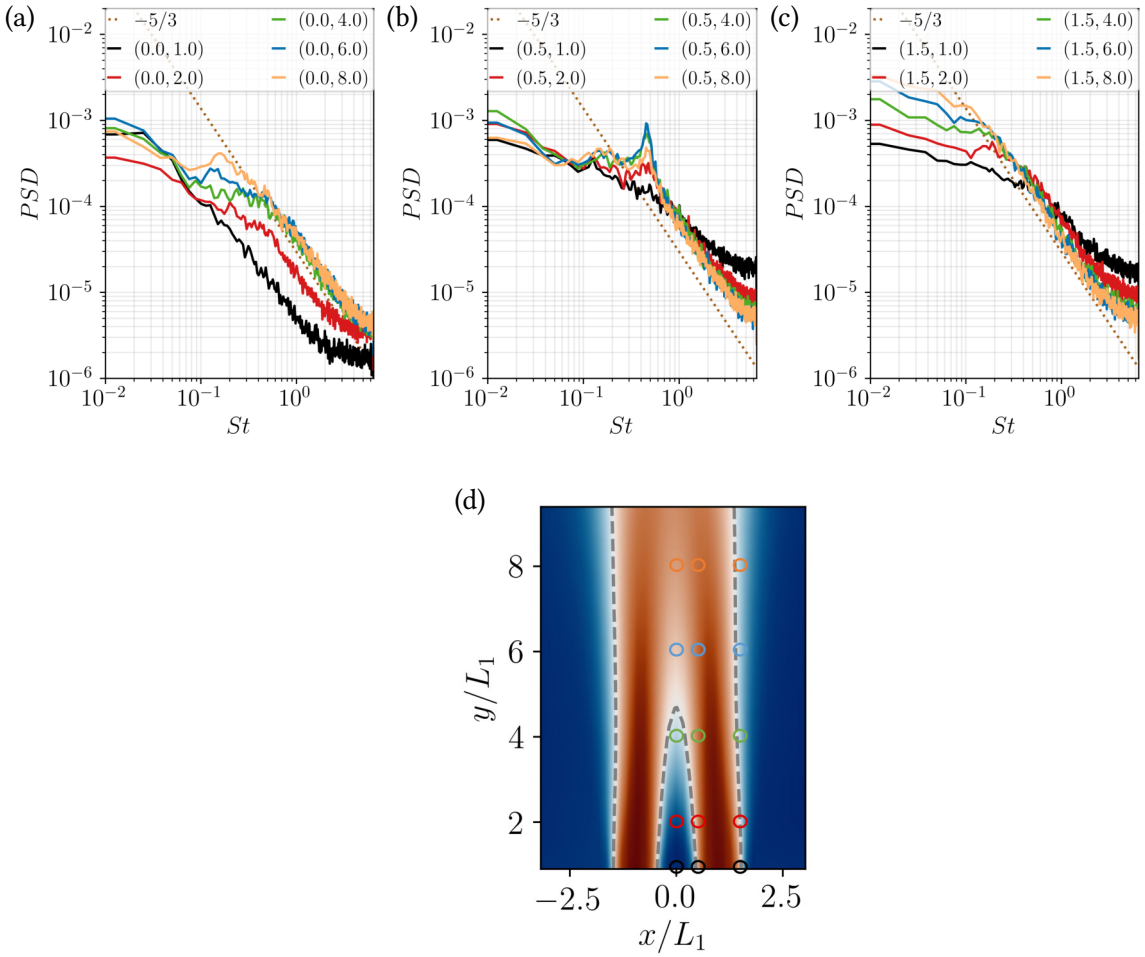

Figure 3.23: Two Jets – PSD of the streamwise velocity $v(t)$ at several $(x/L_1, y/L_1)$ locations: (a) $x/L_1 = 0$; (b) $x/L_1 = 0.5$; (c) $x/L_1 = 1.5$; d) Color-coded locations for PSD analysis along the jet flow.

3.4.3 PSD Analysis of the Cross-stream Velocity Field

We follow the same procedures to analyze the cross-stream velocity u. The spectra for the u component for fixed y/L_1 are shown in Figure 3.24. The same color scheme as that used for the v component is used here: the black, red, green, blue, and orange curves correspond to the spectra at $x/L_1 = -1.5, -0.5, 0.0, 0.5$, and 1.5, respectively. At $y/L_1 = 1$, two dominant peaks appear

at $x/L_1 = 0$ (in the range of $0.35 < St < 0.55$), while all other x/L_1 curves appear to show a distinct peak at about $St = 1.27$. In Section 3.4.4, we will determine that the $St = 1.27$ peaks are not significant. The spectra at these locations also indicate a clear inertial subrange regions for $y/L_1 \geq 4$. As seen in the spectra of the v component, a dominant peak at $St = 0.47$ is also present in the inner shear layer regions ($x/L_1 = \pm 0.5$) at $y/L_1 = 4$ (Figure 3.24b). Moreover, unlike in the results of the v component, a dominant peak at the center between the jets ($y/L_1 = 0$, green curve) is present. This peak has equal strength as the other peaks, indicating equal significance for this velocity component. Furthermore, as shown in Figure 3.24c, the dominant peak is still present at the centerline between the two jets; however, there is an increase in the energy spectra amplitude at the lower frequencies. The increase in the spectrum amplitude is more distinct at locations $x/L_1 = \pm 0.5$ (blue and red curves).

The spectra shown in Figure 3.25a for $x/L_1 = 0$ also indicates that the strength of these dominant peaks increases for increasing y/L_1, and again starts decreasing for locations $y/L_1 \geq 8$. At $x/L_1 = 0.5$ (Figure 3.25b) the peaks at $St = 0.47$ are also present, but with lower amplitude than at $x/L_1 = 0$. In the outer shear layer region (Figure 3.25c), the spectra does not indicate any more prominent peaks for this component. Having an understanding of the power spectra, we now proceed with the SPOD modal analysis technique to associate these frequencies to structures in the flow field.

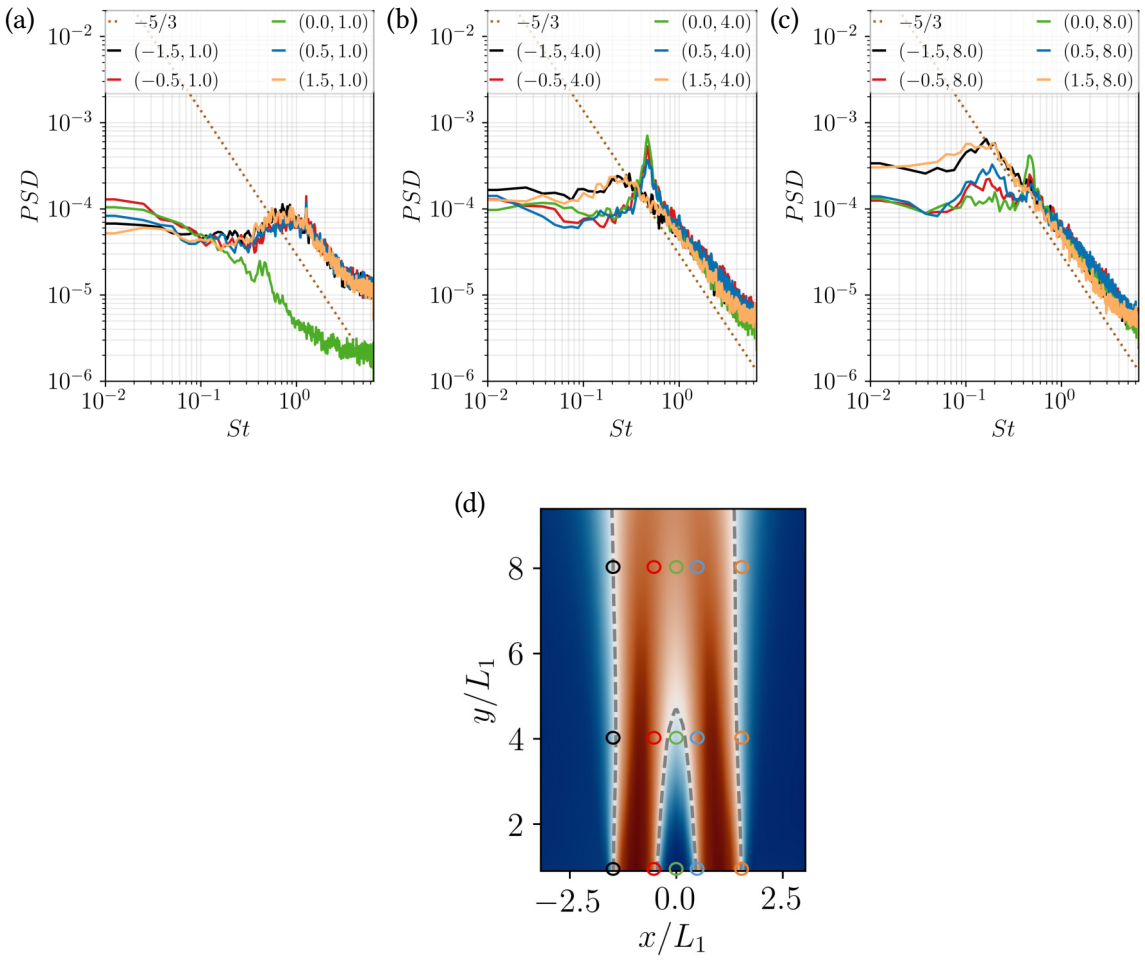

Figure 3.24: Two Jets – PSD of the cross-stream velocity $u(t)$ at several $(x/L_1, y/L_1)$ locations: (a) $y/L_1 = 1$; (b) $y/L_1 = 4$; (c) $y/L_1 = 8$; d) Color-coded locations for PSD analysis along the jet flow.

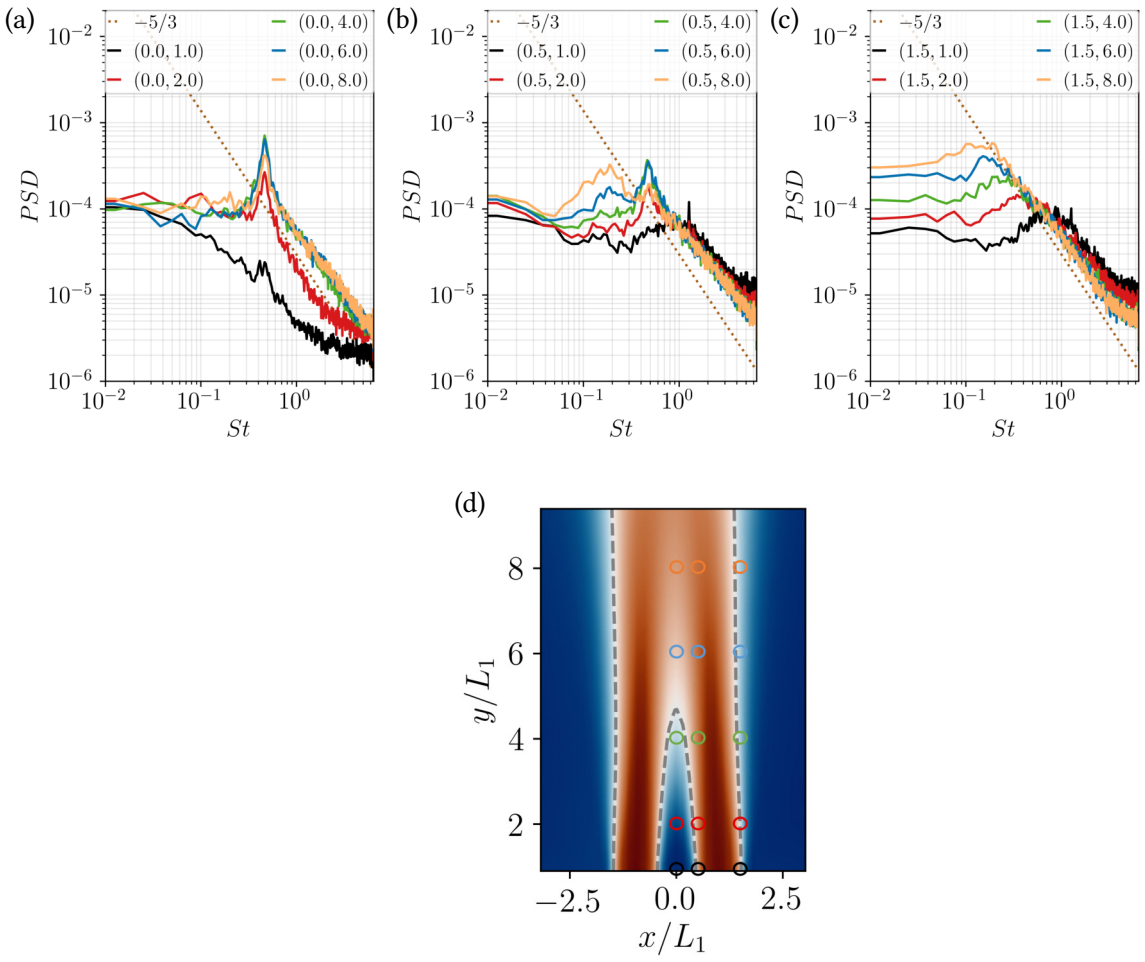

Figure 3.25: Two Jets – PSD of the cross-stream velocity $u(t)$ at several $(x/L_1, y/L_1)$ locations: (a) $x/L_1 = 0$; (b) $x/L_1 = 0.5$; (c) $x/L_1 = 1.5$; d) Color-coded locations for PSD analysis along the jet flow.

3.4.4 Modal Analysis

3.4.4.1 Modal Analysis of the Configuration with Two Jets

Complementary to the PSD analysis, we identify the coherent flow structures by means of the SPOD procedures described in Section 1.2.2.4. SPOD is used to decompose the flow field into energy-ranked modes (coherent structures) which evolve coherently in space and time. We first obtain the SPOD modes for the streamwise velocity v, and then proceed with the same analysis for the cross-stream component u. In the following plots, we refer to the SPOD eigenvalue spectra as SPOD Spectra. The SPOD spectra showing the five most dominant modes, with mode one (black curve) being the most energetic, are reported in Figure 3.26a. The black, red, green, blue, and orange curves correspond to modes one through five, respectively. The SPOD spectra resembles the local PSD spectra shown in Figures 3.22 and 3.23, and consistently also exhibits a dominant peak at $St = 0.47$. Each spectrum of SPOD eigenvalues ranges from $St = 0$ up to $St = f_{Nyquist}L/V_0$, where the Nyquist frequency for these measurements is $f_{Nyquist} = 200\ Hz$. Consequently, we can obtain modes that each oscillate at a single frequency within this range.

For example, the SPOD modes one and two, which oscillate with a frequency of $St = 0.47$ are shown in Figures 3.26b and 3.26c, respectively. These modes illustrate the flow structures that oscillate at the single frequency of $St = 0.47$. Mode one (Figure 3.26b) shows the coherent flow structure enclosed by the inner shear layers. The blue and red circular areas indicate that there are a series of patterns occurring, in- and out-of-phase. Therefore, along the streamwise direction, there are two wave–like fronts propagating over time, and each of these two fronts are connected to their respective inner shear layer. These patterns are characteristic to the Kelvin–Helmholtz instability of the shear layers. The second mode at this frequency (shown in Figure 3.26c) indicates the presence of a secondary coherent structure; however, its amplitude (shown in Figure 3.26a) is almost an order of magnitude smaller, indicating that this mode is less significant at this frequency. In the vicinity of the maximum peak, there are other dominant frequencies; however, these dominant frequencies with lower amplitudes appear to be artifacts of the nature of

experimental data. That is, these oscillatory coherent structures occur at a range of frequencies. For example, the coherent flow structure exhibited by mode one at frequency $St = 0.36$ (Figure 3.26d) is ultimately the same coherent structure present at $St = 0.47$. Furthermore, as determined by the local PSD analyses, there is growth and decay of the flow structures with increasing y/L_1. This is manifested as a change in the red and blue areas along the flow direction.

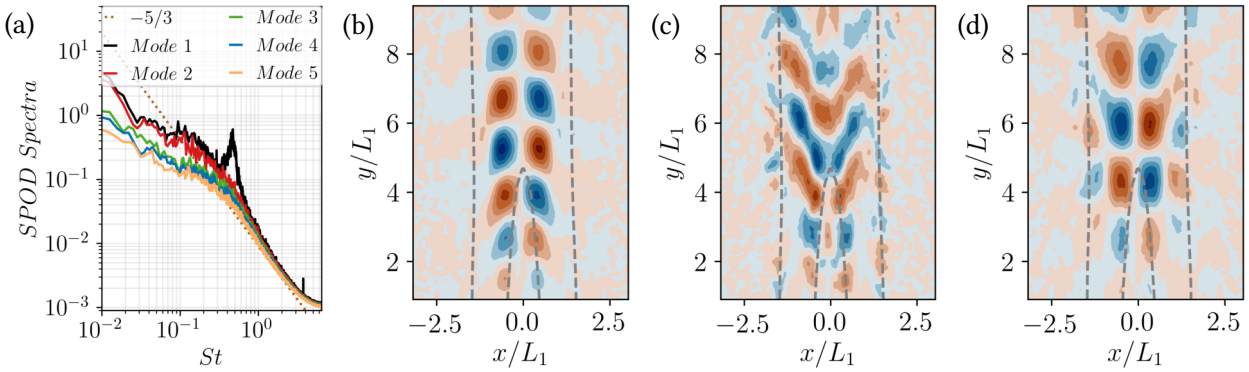

Figure 3.26: Two Jets – SPOD of $v(t)$: a)SPOD energy spectra; b) Mode one, $St = 0.47$; c) Mode two, $St = 0.47$; d) Mode one, $St = 0.36$.

We now follow the same procedure of the SPOD analysis for the cross-stream velocity component u. The SPOD mode spectra, shown in Figure 3.27a, exhibit a very similar shape to that of the streamwise component. For this component, the dominant frequency is present at $St = 0.47$. In addition to the dominant frequency at $St = 0.47$, there appears to be another dominant frequency band in the range of $St = 0.10$ and $St = 0.30$. This dominant frequency band is exhibited in the first and second modes (black and red curves). Mode one at $St = 0.47$ is shown in Figure 3.27b. This coherent structure is very different from that encountered for the v component; however, it is due to the same Kelvin–Helmholtz instability. This structure is the one responsible for the back and forth lateral oscillation between the two jets. This structure spans from the left to the right inner shear layers, which links the two jets together. Similar to the coherent structures for v, this structure exhibits a wave–like pattern as well, indicating the progression of this mode over time in the streamwise direction. The second mode at this frequency (Figure 3.27c) exhibits similar features to the v component structures (but at a lower amplitude) – further supporting

our hypothesis of the connection between the two modes from the two components. Last but not least, while the second band of dominant frequencies does not exhibit a distinct peak, we chose to plot the dominant mode associated with the peak at $St = 0.15$, as shown in Figure 3.27d. This mode contains large coherent structures in the regions of the outer shear layers. This is indicative of a lateral oscillatory behavior which occurs simultaneously at the outermost regions of the jets. While this band of frequency appears to be dominant, further investigation will be carried out to ensure that these are significant coherent flow structures.

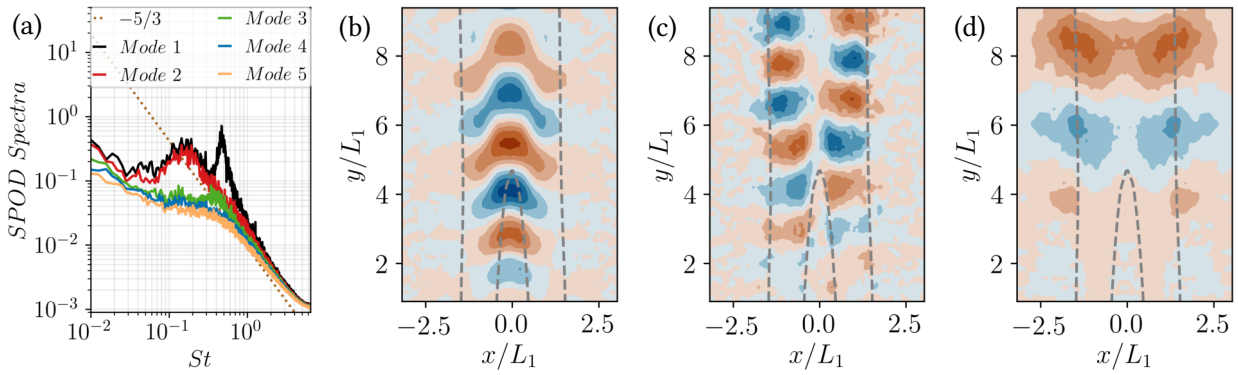

Figure 3.27: Two Jets – SPOD of $u(t)$: a)SPOD energy spectra; b) Mode one, $St = 0.47$; c) Mode two, $St = 0.47$; d) Mode one, $St = 0.15$.

In addition, we conducted experiments with Reynolds numbers ranging from $Re = 6,900$ to $Re = 48,500$ to investigate the influence of the flow speed on the coherent structures and the associated Strouhal numbers. The conditions of these experiments, including the Strouhal numbers, is summarized in Table 3.9.

Table 3.9: PIV measurements for various Reynolds numbers.

Mass Flow Rate (GPM)	$Re(-)$	$V_0\ (m/s)$	$St(-)$
4.2	6,931	0.328	0.48
5.5	9,076	0.430	0.48
8.4	13,862	0.657	0.47
12.6	20,793	0.985	0.47
16.8	27,725	1.314	0.49
21.0	34,656	1.642	0.49
25.2	41,587	1.971	0.46
29.4	48,518	2.300	0.48

In Figure 3.28 the SPOD spectra for the streamwise velocity components are reported for increasing Reynolds numbers. For this range of Reynolds numbers, the dominant frequencies also occur about $St = 0.47$. These profiles also show a total increase of energy across the various scales (higher magnitudes in the spectrum) with increasing Reynolds number, as expected. In addition, the dominant peaks become more defined for increasing Reynolds numbers. The Strouhal number at which these peaks occur is reported in Table 3.9. The corresponding coherent structures at $St \approx 0.47$ are illustrated in Figure 3.29. Here, the coherent structures appear to be independent of Reynolds number. This is indicative of an inviscid instability mechanism. The SPOD spectra and their corresponding modes at $St \approx 0.47$ are shown in Figures 3.30 and 3.31. Here too, the SPOD energy spectra exhibit peaks at $St \approx 0.47$, with the peaks becoming more dominant, and the coherent structures associated with them remain about the same regardless of Reynolds numbers.

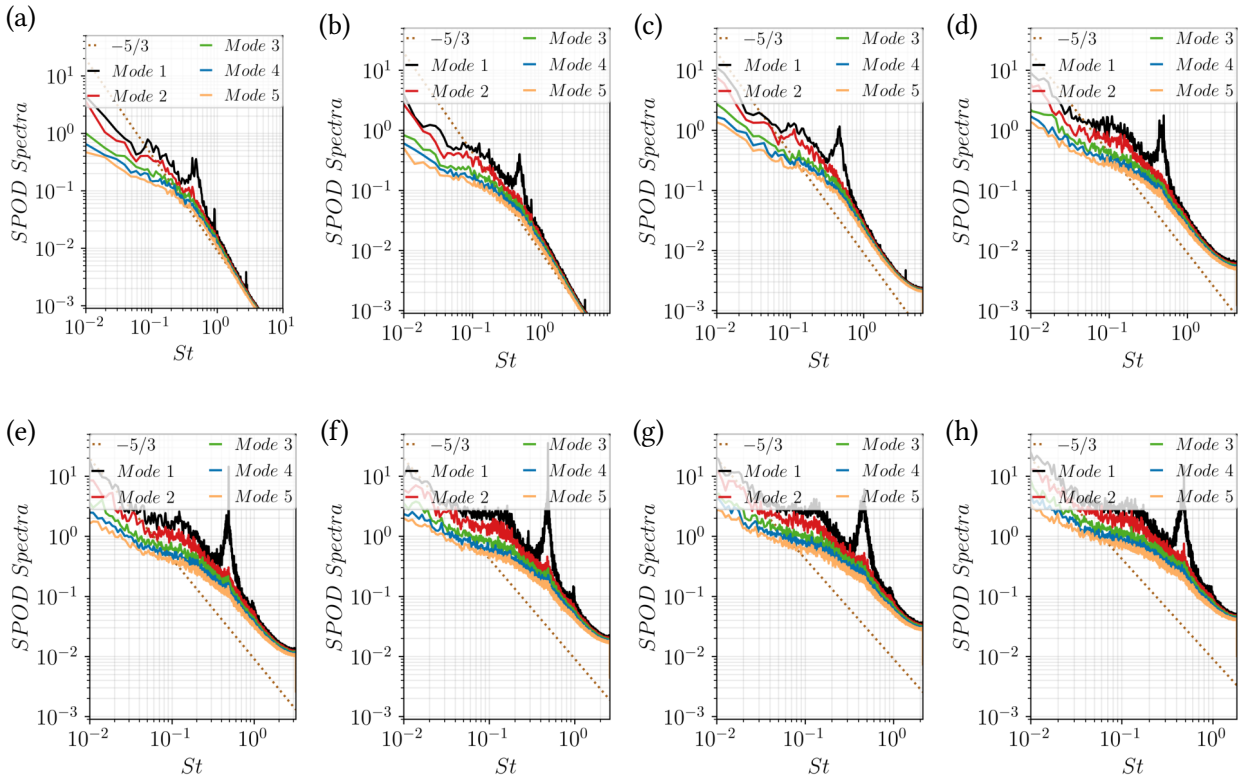

Figure 3.28: Two Jets – $v(t)$: SPOD energy spectra for various Reynolds numbers $Re =$ a) $6,900$; b) $9,000$; c) $13,800$; d) $20,800$; e) $27,700$; f) $34,700$; g) $41,500$; h) $48,500$.

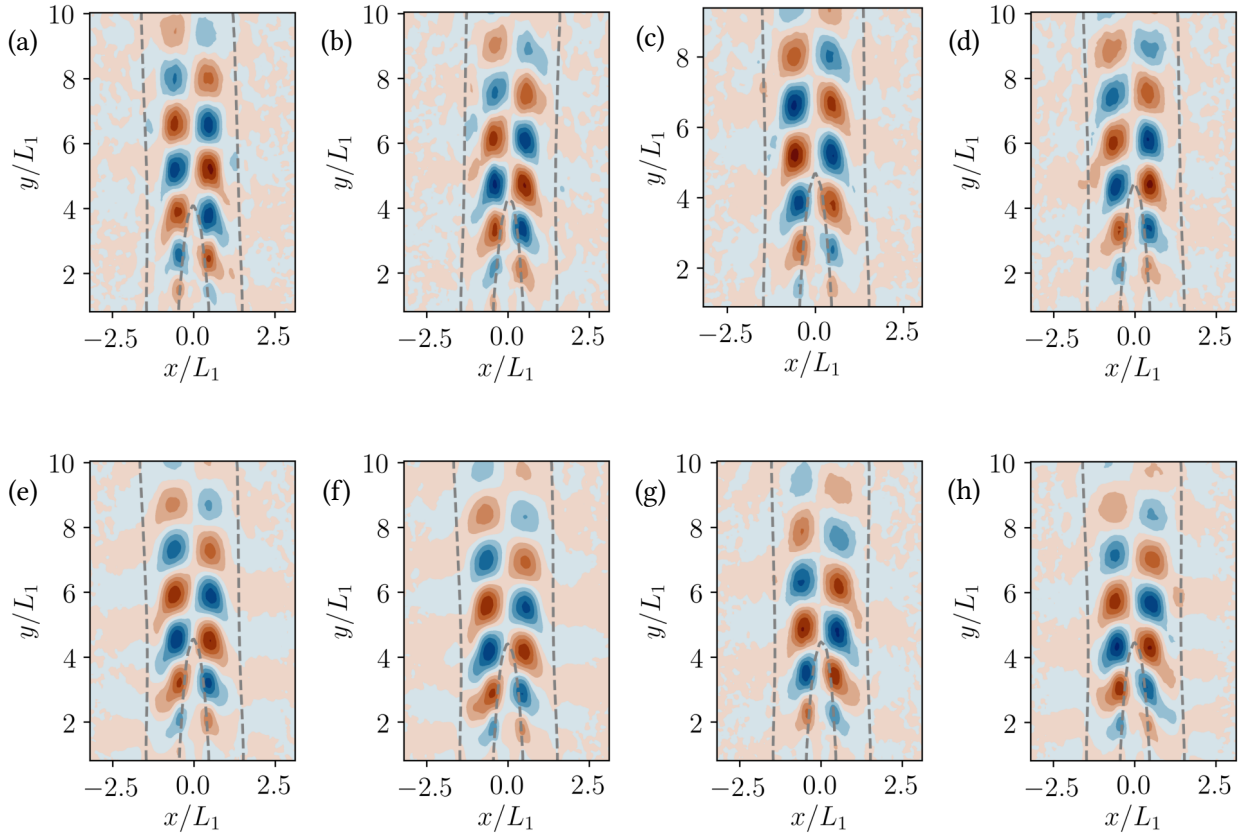

Figure 3.29: Two Jets – $v(t)$: SPOD Mode one at $St \approx 0.47$ for various Reynolds numbers $Re =$ a) $6,900$; b) $9,000$; c) $13,800$; d) $20,800$; e) $27,700$; f) $34,700$; g) $41,500$; h) $48,500$.

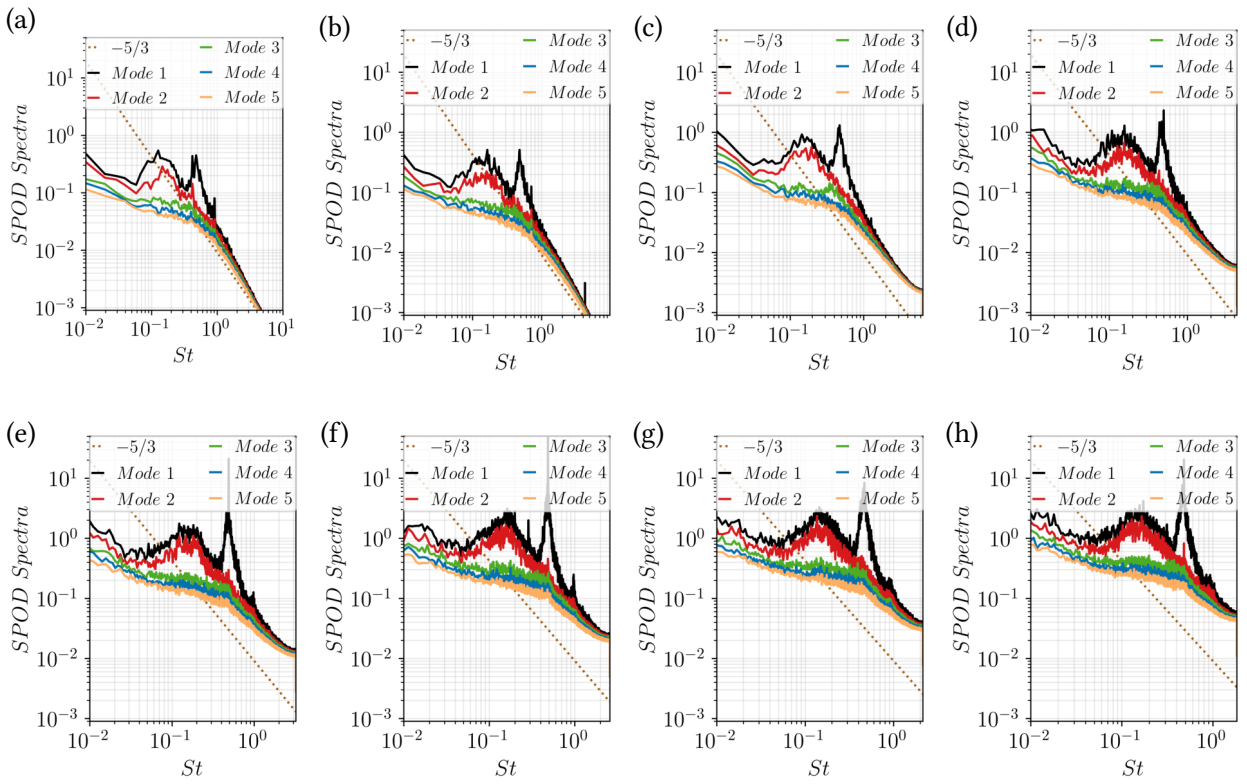

Figure 3.30: Two Jets – $u(t)$: SPOD energy spectra for various Reynolds numbers $Re =$ a) $6,900$; b) $9,000$; c) $13,800$; d) $20,800$; e) $27,700$; f) $34,700$; g) $41,500$; h) $48,500$.

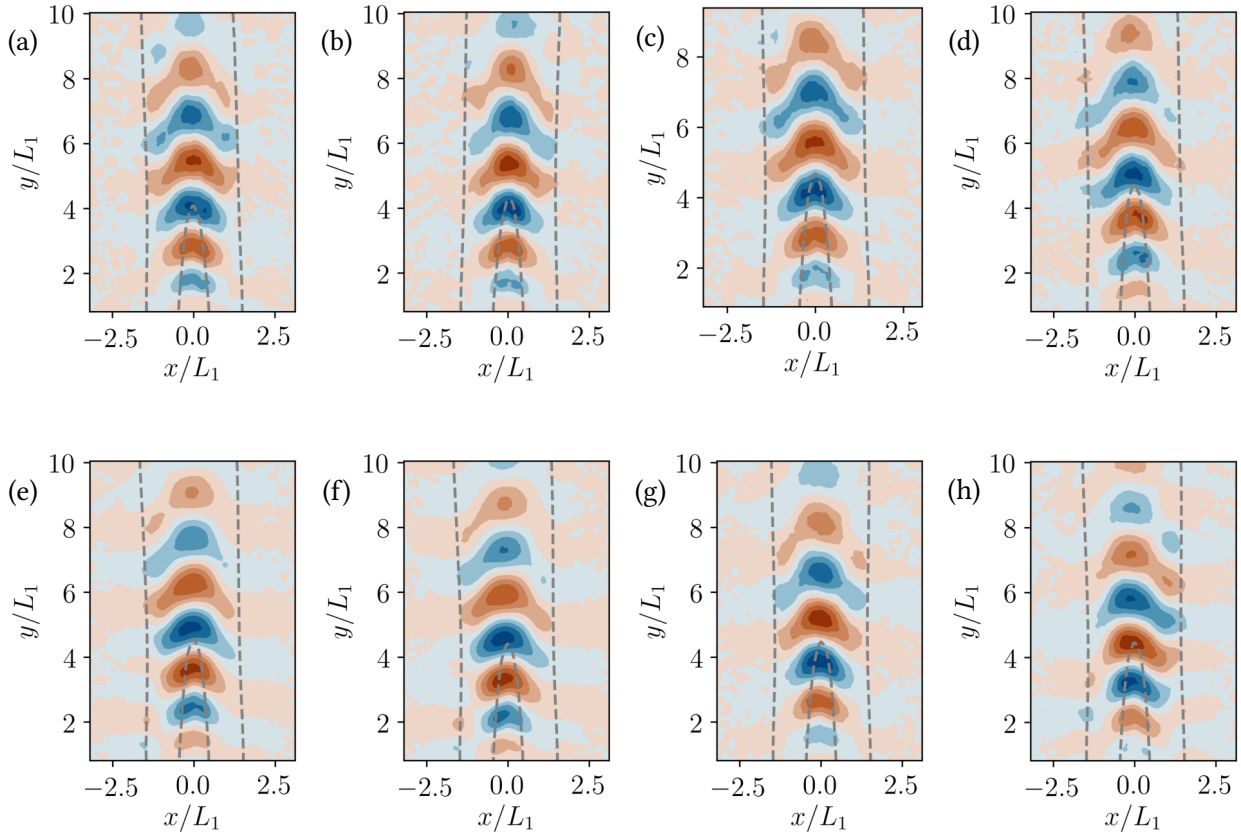

Figure 3.31: Two Jets – $u(t)$: SPOD Mode one at $St \approx 0.47$ for various Reynolds numbers $Re =$ a) $6,900$; b) $9,000$; c) $13,800$; d) $20,800$; e) $27,700$; f) $34,700$; g) $41,500$; h) $48,500$.

3.4.4.2 Modal Analysis of the Configuration with Four and Six Jets

We proceed here with the SPOD analysis for the flow fields of four and six parallel jets. The mean streamwise velocity field, SPOD mode energy spectra, and coherent structures for the four and six jet configurations are provided in Figures 3.32 and 3.33, respectively. The mean streamwise velocity field for four jets is shown in Figure 3.32a. The SPOD spectra for the four jets, shown in Figure 3.32b, exhibits a broader band of peaks with the most dominant peaks occurring at $St = 0.39$ and $St = 0.47$. We speculate that this broader band occurs because of the larger back and forth feedback experienced between the four jets. For the four jet configuration, the SPOD mode at $St = 0.39$ (Figure 3.32c) exhibits the same features present in the case with two jets. The first mode shows two instances of the modes observed in the two jet configuration: one set of structures in between the inner shear layers created by the two leftmost jets, and another for the two rightmost jets. This indicates that the two jets in the left interact with one another separately from the two jets on the right (as predicted from the mean flow quantities), and that the frequency of oscillation in the inner layers is the same. This oscillation is not present at the center between the two jet pairs at $x/L_1 = 0$, which indicates no strong reoccurring interactions between the two inner jets at this frequency. Furthermore, there is a very distinct mode at $St = 1.03$; however, this dominant peak was determined to not be related to the flow structures. Furthermore, the six jet configuration exhibits similar characteristics. The mean streamwise velocity field for six jets is reported in Figure 3.33a. The SPOD spectra, illustrated in Figure 3.33b, show an even broader band of dominant peaks. This broader band can be explained by the larger local Reynolds number, and larger feedback arising from more jets interacting. As result, the coherent structures from the six jet configurations (Figure 3.33c) are not as well defined as those observed in the two or four jet configurations. Due to the spectra being more complex, further investigation will need to be carried out to further expand on the flow structures from the six jet configuration.

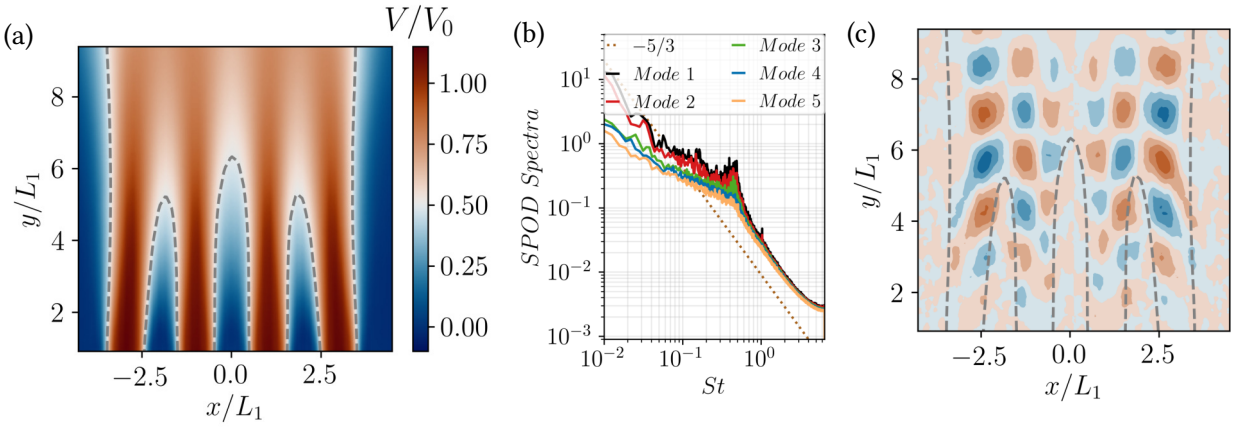

Figure 3.32: Four Jets – SPOD of $v(t)$: a) Mean velocity field; b)SPOD energy spectra; c) Mode one, $St = 0.47$.

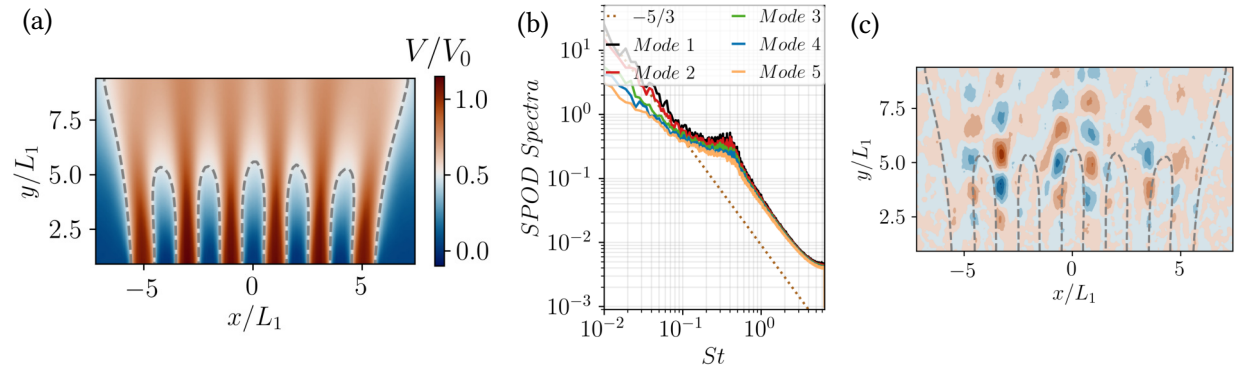

Figure 3.33: Six Jets – SPOD of $v(t)$: a) Mean velocity field; b)SPOD energy spectra; c) Mode one and two, $St = 0.47$.

3.5 Summary of Findings

In this chapter, we presented CFD-grade experimental data with their corresponding uncertainties for the investigation of multiple jet interactions in a plenum. We described the similarities of the interactions between two, four, and six jets by inspecting the time-averaged fields, and we have demonstrated the convergence, repeatability, and reproducibility of these measurements through various tests. Through our convergence study we determined, as expected, that the convergence of higher order statistics, such as the Reynolds stresses, as function of acquired image pairs is more sensitive to variations in the flow fields. Through the repeatability and reproducibility studies, we exposed the challenges of obtaining reproducible profiles through PIV,

even in the best case scenarios. Because of the complexity of PIV systems, slight laser misalignment or the use of different equipment can lead to large variations in the flow fields, especially for higher order statistics (e.g. Reynolds stresses). Through brief comparison between experimental and simulation results, we discerned differences in the velocity and Reynolds stress profiles, and investigated the causes for the over- and under-prediction of these quantities. Through these comparisons, we aim to provide the basis for different approaches that can be taken to improve the performance of RANS based models for nuclear engineering applications.

In the last section, we provided time-resolved experimental data for the two, four, and six jet configurations. We analyzed the flow fields of two parallel rectangular jets by means of PSD and SPOD techniques. The PSD analyses provided us with insight about how the flow structures and length scales evolved in the flow field. We educed dominant frequencies present in the flow fields of the streamwise and cross-stream velocity components. Through SPOD we identified the coherent flow structures responsible for conjunction between the inner shear layers. The structure linking the inner shear layers appeared in the cross-stream velocity component. The structures obtained from the streamwise velocity, indicated wave-like patterns which only occurred in the inner shear layer regions. While the dominant frequencies were not identical, they did not differ by a large amount. We then investigated the influence of the Reynolds number of the coherent structures and determined that the mixing mechanisms were independent of Reynolds numbers for ranges of $Re = 6,900 - 48,500$. Furthermore, we expanded our analysis to the configuration of four and six jets. While similar coherent structures were discerned in the same frequency range, they were not as distinct as those which appeared in the two jet configuration. We speculate that the broader energy bands of dominant frequencies present in the four and six jet configurations are caused by the increasing local Reynolds number, which induces larger feedback between the jets.

Chapter 4

The HiRJet Facility

The understanding of stratification phenomena is imperative for the development and design of systems where density gradients are present. To estimate the transport of scalar quantities (e.g., temperature, density, species concentration, etc.), CFD RANS-based turbulence models rely on the Gradient-Diffusion Hypothesis (GDH) to model turbulent fluxes in the Reynolds-Averaged Scalar Transport equation, and a simplified model to take into account turbulent kinetic energy production/suppression due to density differences. These two approximations are known to under-perform for buoyancy-driven flows, and for this reason additional high-resolution experimental data is needed for the validation and improvement of these models.

In this chapter, we provide measurements of density distributions obtained in the HiRJet facility by means of a WMS unit. We utilize these data to investigate the propagation of stratified fronts under positive and negative density gradients. These CFD-grade experimental data, for experiments with 1.5% and 3% density differences, were compared with the results from RANS simulations to assess the deficiencies of current turbulence models. Based on our analysis, we determined that two metrics can be used to describe the propagation of stratified fronts: the speed of propagation and the length over which mixing takes place. We determined that when a lighter fluid is injected into a heavier fluid, the mixing region is larger and that the speed of propagation of the front is slower in the simulations. However, when the heavier fluid was injected into the lighter fluid, the opposite trends were observed. Furthermore, we provided a discussion on how one of the coefficients in the turbulence dissipation rate ϵ equation could be the reason for the discrepancies between the experiments and simulations. Lastly, through repeatability tests, we determined these measurements were highly repeatable.

4.1 Overview

As previously discussed, to estimate the transport of scalar quantities (e.g., temperature, density, species concentration, etc.), CFD RANS turbulence models rely on the GDH (Equation 4.1) to model turbulent fluxes in the Reynolds-averaged scalar transport equation (Equation 4.2):

$$-\rho\overline{u_j'\phi'} = \rho\Gamma_t\frac{\partial\Phi}{\partial x_j}, \tag{4.1}$$

$$\frac{\partial(\rho\Phi)}{\partial t} + \frac{\partial(\rho\Phi u_j)}{\partial x_j} = \frac{\partial}{\partial x_j}\left(\rho\Gamma\frac{\partial\Phi}{\partial x_j} - \rho\overline{u_j'\phi'}\right). \tag{4.2}$$

The GDH closure relation is known to underperform in several scenarios [79–82], including but not limited to, cases with large density gradients [25, 26]. Several variations of the GDH model ranging from algebraic to transport models have been developed, and each have their strengths and weaknesses. While no specific model has been regarded as the best, high-fidelity high-resolution data of buoyancy-driven flows is needed for further development and validation of those models [79]. In this section we experimentally investigate the propagation of stratified fronts under positive and negative density gradients, and compare the results with CFD simulations. The comparison between experimental and simulation results is used to assess the deficiencies of current turbulence models. The experimental results presented in this chapter have been conducted at the HiRJet experimental facility described in Chapter 2. Measured boundary conditions include: flow-rate, inlet section velocity profile, and inlet section density distribution as functions of time.

4.2 Results and Discussion

Buoyant flows are typically categorized by the Reynolds Number Re (Equation 4.3) and the Froude Number Fr (Equation 4.4). These dimensionless quantities were calculated by using the

inlet flow conditions according to the following formulas [83, 84]:

$$Re = \frac{\rho_{in} U_0 L_0}{\mu_{in}} = \frac{\text{Inertial Forces}}{\text{Viscous Forces}}, \tag{4.3}$$

$$Fr = \frac{U_0}{\sqrt{g L_0 \frac{\rho_{in} - \rho_a}{\rho_{in}}}} = \frac{\text{Inertial Forces}}{\text{Gravitational Forces}} = \frac{1}{\sqrt{Ri}}, \tag{4.4}$$

where ρ is the density, U_0 the nominal velocity, μ the dynamic viscosity, L_0 the characteristic length (i.e., the jet diameter), g the acceleration due to gravity, Ri the Richardson Number, and the subscripts "in" and "a" indicate inlet and ambient, respectively. Experiments with 1.5% and 3% density differences were conducted in the HiRJet facility, and the time-dependent density field in a cross-section of the HirJet tank was measured with a WMS. At the inlet, a mass flow rate of 2.5 GPM was maintained for all experiments. This allowed for buoyant fronts with Reynolds numbers and Froude numbers (Re; Fr) of (5,015; 1.86) and (4,400; 1.32). To create density differences in the flow, water and sugar solutions were utilized. In the positive density gradient experiments, the lower density fluid was injected into a tank filled with the higher density fluid, which due to buoyancy forces, accumulated at the top of tank and propagated towards the outlet as more fluid was introduced into the tank. For the negative gradient experiments, the heavier fluid was injected at the inlet and sank towards the outlet. The boundary conditions were closely monitored by having a WMS and a flow meter near the inlet. Furthermore, the densities and viscosities of the fluids were measured to provide adequate flow properties for the CFD simulations.

4.2.1 Experimental Test Matrix

An experimental test matrix was defined aimed at investigating the speed of propagation of a stratified front and the spread (i.e. degree of mixing) of the stratified layer. The test matrix is reported in Table 4.1, where $\dot{V}_0$ is the volumetric flow rate, and U_0 is the average inlet velocity. The corresponding Re, Fr and Ri numbers are also reported in the table. Two sets of experiments were performed, case 1a and 1b at a density difference of 1.5% and case 2a at a density difference of

3%. In the test cases labeled with "a", low density fluid was injected into the test section previously filled with high density fluid (negative density gradient). In the test case labeled with "b", high density fluid was injected into a tank of low density fluid instead (positive density gradient).

Table 4.1: Test matrix for the positive and negative density gradient experiments.

Case	$\frac{\rho_{in}-\rho_a}{\rho_{in}} \times 100(\%)$	$\dot{V}_0$(GPM)	$U_0(m/s)$	$Re(-)$	$Fr(-)$	$Ri(-)$	Density gradient
1a	1.5	2.5	0.1391	5,015	1.86	0.29	< 0
1b	1.5	2.5	0.1391	5,015	1.86	0.29	> 0
2a	2.9	2.5	0.1391	4,400	1.32	0.58	< 0

As mentioned previously, the time-dependent density fields in the inlet cross-section and in the test section are measured by means of wire-mesh sensors. Since the measurement principle of wire-mesh sensors is based on the fluid electrical conductivity, we used tap water and Deionized (DI) water as our base fluids. This is because the electrical conductivity of tap water is sufficiently higher than DI water for the wire-mesh sensors to distinguish between the two fluids, and both tap water and DI water are readily available in our laboratory.

Tap water and sugar aqueous solutions (made with DI water) with concentrations of 4 and 8 weight percent (wt%) were used to achieve 1.5% and 3% density differences, respectively. As a consequence of utilizing sugar, the dynamic viscosities increased by 9% and 35% percent, respectively. The fluid properties are provided in Tables 4.2 and 4.3, together with the temperature at which the properties were measured.

Table 4.2: Fluid properties of sugar solution with a 1.5% density difference.

	Tap Water	Sugar Solution (4wt%)	$\frac{X_{Sugar}-X_{Water}}{X_{Water}} \times 100(\%)$
$\rho(kg/m^3)$	999	1014	1.50
$\mu(mPa \cdot s)$	1.05	1.15	9.19
$\nu(m^2/s)$	1.05E-06	1.13E-06	7.57
$T(^{\circ}C)$	17.8	17.5	-1.69

Table 4.3: Fluid properties of sugar solution with a 3% density difference.

	Tap Water	Sugar Solution (8wt%)	$\frac{X_{Sugar} - X_{Water}}{X_{Water}} \times 100(\%)$
$\rho(kg/m^3)$	999	1028	2.90
$\mu(mPa \cdot s)$	1.05	1.23	35.57
$\nu(m^2/s)$	1.05E-06	1.20E-06	31.49
$T(^{\circ}C)$	17.8	24	34.83

WMS data was acquired for approximately 20 minutes at a sampling rate of $100Hz$, and the measurement spatial resolution for the test section sensor was $6.35mm$. To describe the operational procedures, we refer to the simplified schematic of the HiRJet facility shown in Figure 4.1.

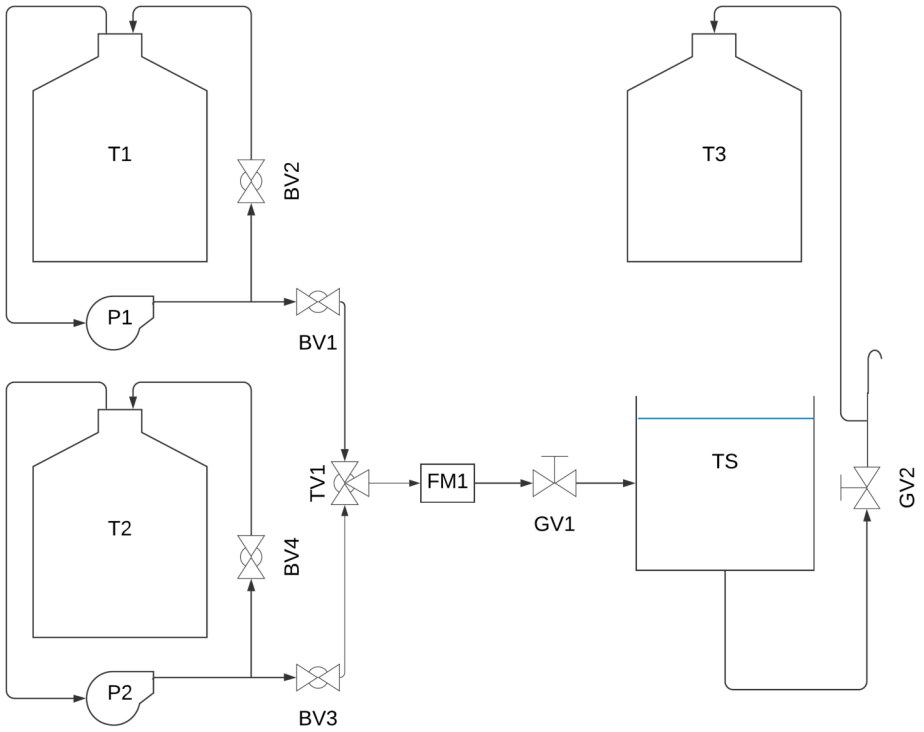

Figure 4.1: Simplified schematic of the HiRJet facility. The black arrows indicate the flow direction.

The experiments were executed in the following manner:

1. Obtain calibration measurements for the fluid in tank one (T1) and then for the fluid in tank two (T2). This is carried out by first filling up the test section (TS) and taking separate

measurements with the WMS to have the reference measurements of the two fluids.

2. Close valves BV2 and BV3 and turn on pumps P1 and P2. Maintain all other valves open. This allows for the fluid in tank two (T2) to recirculate within T2 and allows the fluid from tank one (T1) to flow towards the test section (TS). The test section is then filled up to a height of $54.61\ cm$ with the first solution (tap water for positive gradient experiments and sugar solution for negative gradient experiments, respectively), and the fluid flow is maintained to reach steady state with a volumetric flow rate of 2.5 GPM.
3. Start data acquisition with the WMS unit. The measurement is started before injecting the second fluid.
4. Close valve BV1 and open valves BV2 and BV3. By closing the valve (BV1) leading to the first solution reservoir (T1) and opening the valve leading to the second fluid reservoir (BV3), the second solution is injected into the test section, which was previously filled with the first solution. BV2 was opened to allow recirculation within T1.

Following these steps, the propagation of stratified fronts is captured by the large WMS located inside the tank as shown in Figure 4.2. Additionally, to obtain well defined boundary conditions, the inlet WMS is used simultaneously to measure the density distributions at the inlet. For further details about the facility and the WMS unit, we refer the reader to Chapter 2.

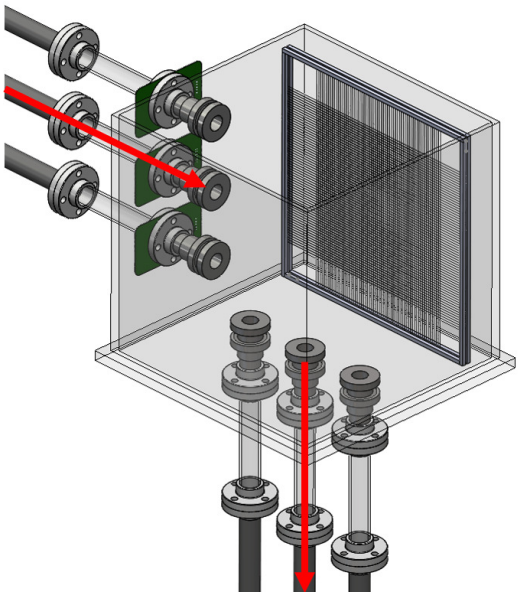

Figure 4.2: CAD of the HiRJet facility with the large WMS located near a wall. The red arrows indicate the flow direction. All other nozzles were kept closed.

4.2.2 Computational Domain

A CFD model was developed to perform simulations and assess the performance of current CFD models against the experimental results obtained at the HiRJet facility. In this section, the mesh development and associated mesh convergence study are discussed, together with the specification of the inlet boundary conditions.

4.2.2.1 Geometry, Mesh, and Initial and Boundary Conditions

The computational fluid domain was created using the CAD module embedded in Siemen's STAR-CCM+ version 12.06. Taking advantage of the symmetry of the geometry, only half of the tank was modeled. The geometry is shown in Figure 4.3. The middle nozzle on the side of the tank was used as the inlet, while the middle nozzle on the bottom was used as the outlet. The nozzles that remained closed during the experiments were not modeled in the simulation. These two simplifications helped reduce the computational costs for the transient simulations without compromising the accuracy of the results. Figure 4.3 indicates the locations of the inlet and outlet, as well as the coordinate system used for the analysis reported in this chapter.

Figure 4.3: CAD of the HiRJet facility used for CFD simulations: a) Side View; b) Angled view.

In the negative density gradient simulation, the tank is initially filled with the sugar solution. This solution is circulated until a steady state is reached, which is used as the initial condition of the transient simulation. At time $t = 0s$, the tap water is injected into the tank at the inlet boundary. The boundary conditions imposed for the simulation were as follow:

1. A velocity profile corresponding to fully develop flow was imposed at the inlet (with tap water properties).
2. A pressure outlet was set at the outlet nozzle.
3. Slip wall conditions were imposed at the top boundary of the tank.
4. No-slip wall boundary conditions were imposed at every other wall.

4.2.2.2 Grid and Time Step Independence Study

The Standard $k\epsilon$ turbulence model with the linear eddy viscosity model was used for all of the simulations presented in this chapter. The following STAR-CCM+ submodels were chosen: an implicit unsteady solver, two-layer all y+ wall treatment, gravity, exact wall distance, turbulent, constant density, segregated species, gradients, segregated flow, non-reacting, multi-component liquid, Standard K-Epsilon turbulence, Reynolds-Averaged Navier-Stokes, and three dimensional. The default model coefficients provided by STAR-CCM+ were used for these simulations.

Grid and time step sensitivity analyses were conducted to ensure that the CFD results were not dependent on the mesh size or on the integration time step. Due to the rectangular geometry of

the fluid domain, trimmer (hexahedron) volume cells were utilized. The grid sensitivity analysis was carried out by comparing the velocity magnitude and the TKE profiles for different grid sizes Δx. Tap water was considered to be the working fluid in the facility, with a constant inlet mass flow-rate. The velocity field for this scenario along the xz-plane at $y = 0$ is shown in Figure 4.4a. Three meshes were used for the sensitivity analysis, a coarse mesh with a base size Δx of 3mm, an intermediate mesh with a base size of 4 mm, and a fine mesh with 5mm base size. Each mesh was divided into three regions with increasing degree of refinement: the highest refinement, with mesh size Δx_f, was used along the jet core and shear regions to resolve the largest velocity gradients, followed by an intermediate refinement region with mesh size Δx_m. The rest of the flow domain is kept at base size Δx. In Figure 4.4b the three refinement regions can be clearly identified, with the darkest region representing the finest mesh (near the inlet), and the lighter regions indicating the coarser part of the mesh. Information about the three meshes used for the mesh sensitivity analysis are provided in Table 4.4. The inlet cross-section has a diameter of $D = 38mm$. With the coarser mesh, corresponding to an inlet mesh refinement of $\Delta x_f = 1.25mm$, a total of 30 cells discretize the inlet boundary.

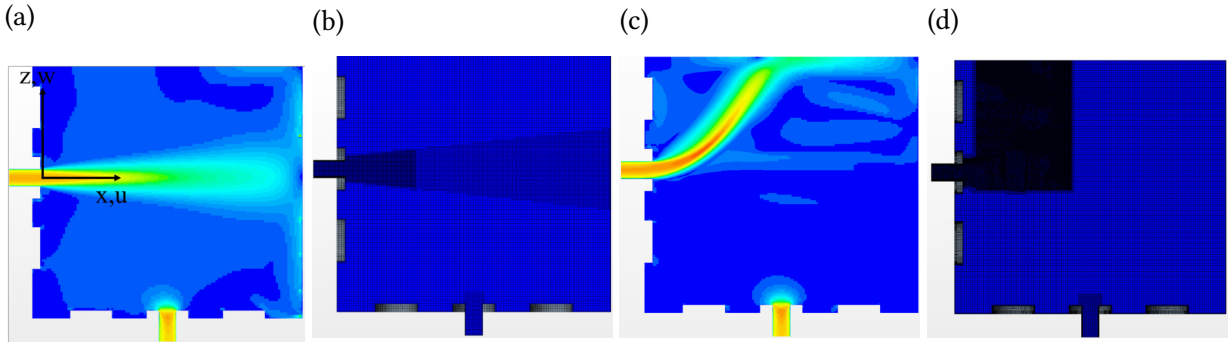

Figure 4.4: Velocity fields (along the xz-plane at $y = 0$) and meshes: a) Steady state velocity field with tap water; b) Mesh for the steady state simulation; c) Velocity field of the transient simulation; d) Mesh for the transient simulation.

The velocity magnitude $|U_{Avg}|$ and the TKE profiles for the three meshes tested are shown in Figure 4.5. The velocity magnitude profiles at $x/D = 1, 11$ (Figures 4.5a and 4.5b) indicate that the velocity fields do not vary significantly by further decreasing Δx_f. The TKE profiles shown

Table 4.4: HiRJet mesh information.

Mesh Number	$\Delta x(mm)$	$\Delta x_m = \frac{\Delta x}{2}$	$\Delta x_f = \frac{\Delta x}{4}$	Number of Cells (Millions)
1	4	2.0	1.00	2.31
2	5	2.5	1.25	1.21
3	3	1.5	0.75	5.37

in Figure 4.5c, indicate that there is a slightly larger discrepancy between profiles at the peaks at $z/D = \pm 0.5$ (where the largest gradients occur). Furthermore, in Figure 4.5d the discrepancies occur throughout the profile; however, these profiles only differ by at most 3% overall. Taking these differences into account, and the computational cost required for the different meshes, the intermediate grid size ($\Delta x_f = 1.00mm$) was determined to be sufficiently fine to capture the flow dynamics in the system.

The transient simulation for the mesh convergence study is performed in conditions of negative density gradient (lighter fluid entering the tank initially filled with the denser fluid). This leads to an upward jet curvature as shown in Figure 4.4c. Later in the transient, as the inlet fluid mixes with the surrounding environment,and the effect of buoyancy consequently decreases, the jet slowly returns to its original horizontal trajectory. To cover the varying jet trajectory, the mesh refinement in the computational domain was modified as shown in Figure 4.4d. Only the regions where the highest velocity and density gradients occur (i.e., near the inlet) were refined to resolve the largest gradients in the flow field.

Sensitivity studies were carried out to determine the optimum integration time-step as well. Three snapshots at different times of the transient simulation, with the measurement plane located at $y/D = +7.5$ as shown in Figure 2.13a, are reported in Figure 4.6. These density fields illustrate the evolution of the density stratification fronts along the z-axis over time. To compare the propagation of the stratified density fronts over time, we used the scaled density calculated according to Equation 4.5:

$$\rho^* = a + \frac{(\rho - \rho_{min})(b - a)}{\rho_{max} - \rho_{min}}, \tag{4.5}$$

where ρ^* and ρ are the scaled and original densities, respectively, and a and b are arbitrary num-

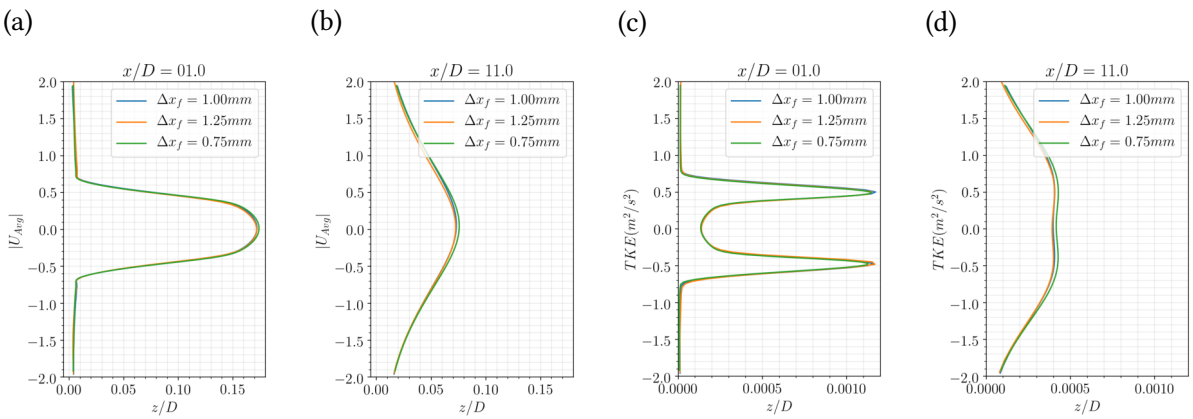

Figure 4.5: Velocity and TKE profiles for different grids: a) Velocity profiles at $x/D = 1$; b) Velocity profiles at $x/D = 11$; c) TKE profiles at $x/D = 1$; d) TKE profiles at $x/D = 11$.

bers to restrict the range of the scaled density to the $[a, b]$ interval. The convention used to indicate a sugar solution (heavy fluid) and tap water (light fluid) is $\rho^* = 0$ and $\rho^* = 1$, respectively. Thus, $\rho^* = 0$ at time $t = 0s$ because the tank is initially filled with the higher density fluid. Furthermore, the spatial axes were scaled by the nozzle diameter D. The propagation of the density fronts for time steps $\Delta t = 0.01, 0.05, 0.25, 1.25s$ at one location below the inlet ($z/D = -5$) and another above the inlet ($z/D = +5$) are shown in Figure 4.7. The stratification fronts for all Δt followed the same trends; however, the largest observable deviations occurred only on the plots for $\Delta t = 1.25s$. Based on these observations, $\Delta t = 0.25s$ was determined to be sufficiently small for the transient simulation. Furthermore, the convergence within the time steps were assessed by verifying that the residuals reached an asymptote (i.e., the residuals do not change further with more inner iterations within the time step). Therefore, to assess the performance of some turbulence models, a time step of $\Delta t = 0.25s$, with the intermediate mesh described in Table 4.4, were utilized. Cell quantity data were extracted from these simulations, and the results are presented in the next section.

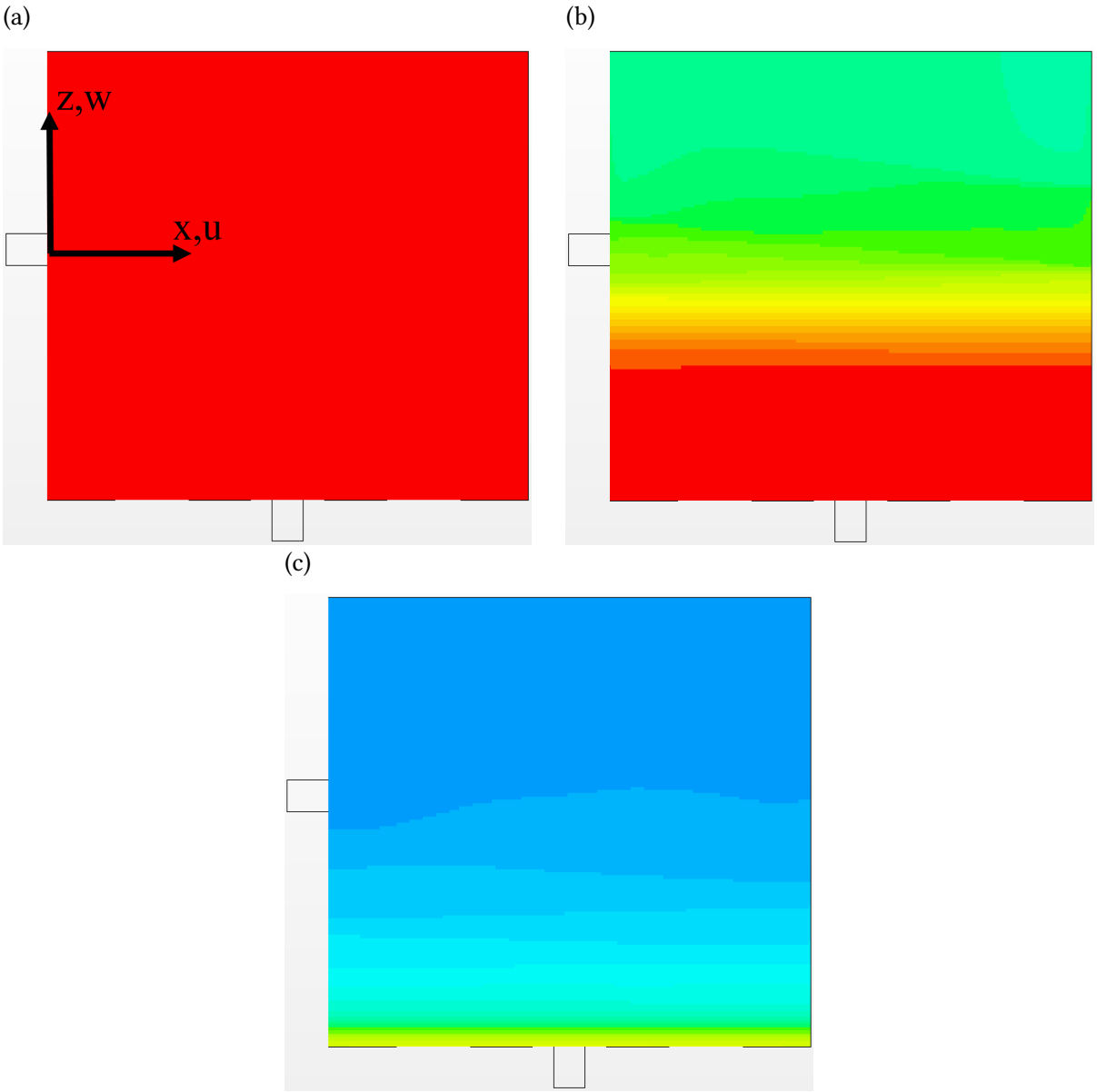

Figure 4.6: CFD Results: Density along the WMS plane at different time steps: a) $t = 0.25s$; b) $t = 400s$; c) $t = 1200s$.

(a)

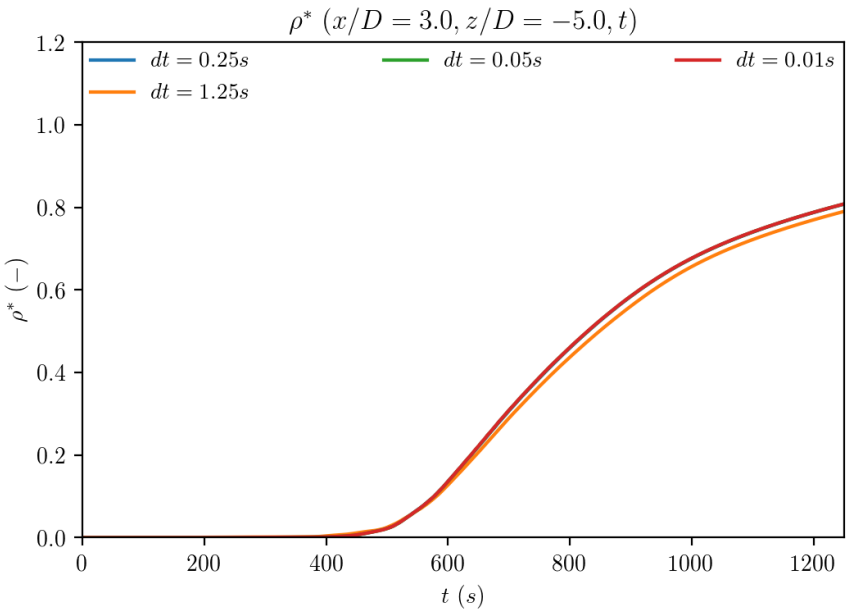

(b)

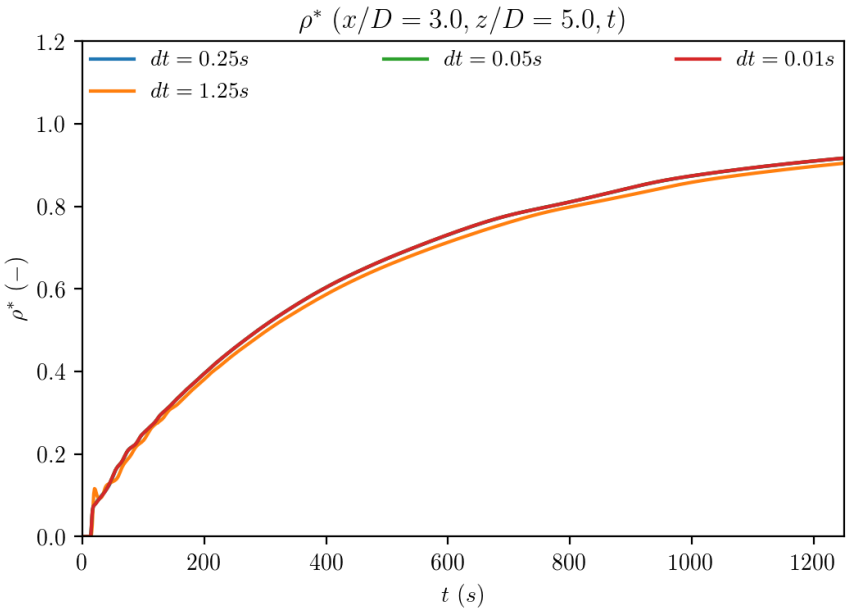

Figure 4.7: Propagation of density fronts over time at two z/D locations: a) $z/D = -5$; b) $z/D = +5$.

4.2.2.3 Experimental and Simulation Results: Inlet Boundary Conditions

With aid of the inlet WMS, the time at which the lower density fluid (tap water) reaches the inlet section can be accurately determined. Three snapshots at different times during the transient are shown in Figure 4.8. The inlet WMS is located at the top right each image. Figure 4.8a shows when the tap water reaches the inlet, and Figures 4.8b and 4.8c are the dimensionless density field 10 and 20 seconds later, respectively. From these density fields, we can observe that at the inlet section, 20 seconds after the tap water arrived, the jet has already stratified, which is important when providing accurate time dependent boundary conditions for the CFD simulations. The stratification in the loop pipe upstream of the inlet to the tank is due to the mixing of the light density fluid with the high density fluid which was present in the system loop at the beginning of the transient.

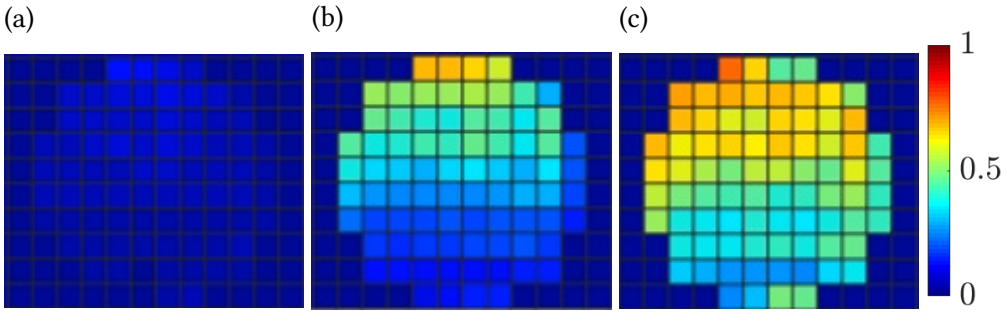

Figure 4.8: WMS data at three different times: a) $t' = 84s$; b) $t' = 94s$; c) $t' = 104s$. A value of zero (blue) indicates the first fluid, and a value of one (red) indicates the second fluid.

The LDV system was used to measure the velocity profile across the inlet pipe diameter (through the acrylic cross-section) at $x/D = -13.1$ upstream of the tank inlet. The LDV probe was displaced in 1mm increments using a translation stage. The velocity profile obtained from a steady state simulation of a fully developed flow with tap water properties (light fluid), and the profile obtained with the LDV system are shown in Figure 4.9. The simulation and experimental results indicate very good agreement — the simulation results fall within the uncertainty bands for the majority of the plot. The agreement between these profiles indicates that the velocity boundary condition in the CFD simulation adequately represents the experiment's inlet

conditions.

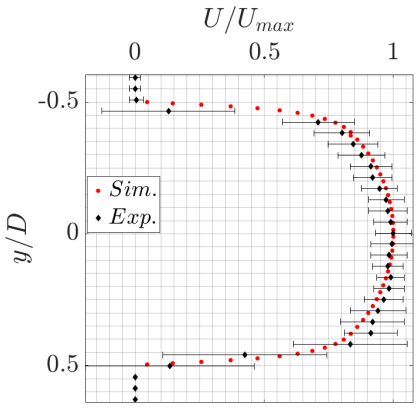

Figure 4.9: Velocity profile at the inlet measurement location: LDV versus CFD results.

4.2.3 Experimental and Simulation Results — Stratified Density Fronts (case 1a)

In this section, the experimental data obtained via the large WMS in the test section is compared to the results from RANS simulations. The propagation of the density fronts and the spread over which mixing occurs is investigated by inspecting the instantaneous density fields. The experimental and simulation results at various time steps are shown in Figure 4.10. Note that the experimental data are available over a smaller area of the tank (i.e., in the region where the WMS is installed). At $t = 100s$, the mixing interface (i.e., the region where the red region changes into yellow) is moderately sharper/thinner in the experiments. At $t = 500s$ and $t = 700s$, the thinner mixing regions are more distinguishable in the experiments. For example, as indicated by the red arrows in Figure 4.10c, the distance from where the red region ends to where the green region ends is broader in the simulations. This is indicative of an over-prediction of turbulent kinetic energy in the simulations, which yields an enhancement of the overall mixing.

We now turn our focus to the local evolution of the fronts over time. The plots of the density front propagation over time at several locations are shown in Figures 4.11 and 4.12. Recall that the x-axis is parallel to the initial jet direction, the z-axis is in the vertical direction, and the y-axis is orthogonal to the xz plane as illustrated in Figure 4.3b. At the given Reynolds number, the

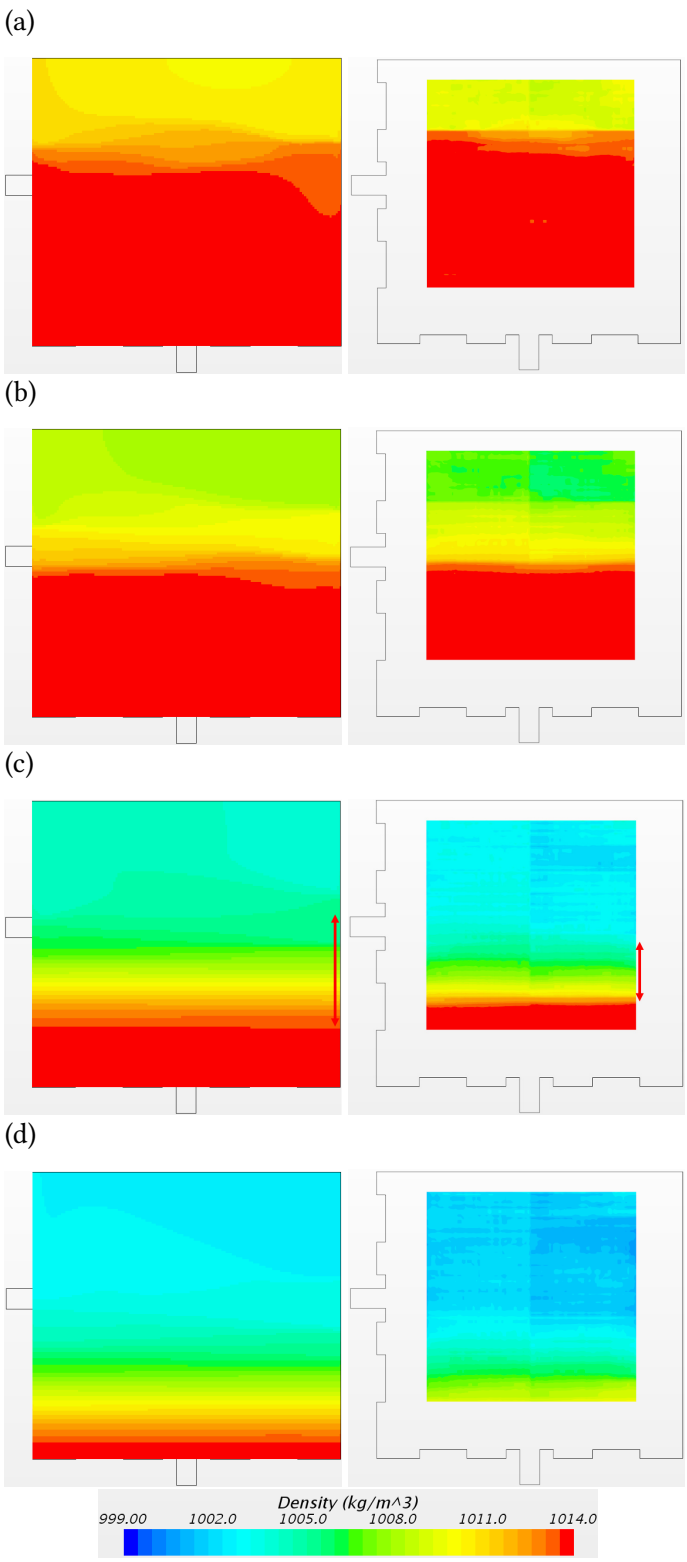

Figure 4.10: Propagation of density fronts at four different times: a) $t = 100s$; b) $t = 200s$; c) $t = 500s$; d) $t = 700s$. Simulations (left) versus experiments (right).

momentum of the jet is strong enough to cause the jet to impinge at the wall farthest from the inlet. For this reason, we separate the discussion based on two regions: Region 1 which covers the first half of the test section ($7.7 > x/D > 0$) and Region 2 which covers the second half ($15.38 > x/D > 7.7$) of the tank. Due to the jet impingement at the wall, larger fluctuations are expected in Region 2 compared to Region 1. The propagation of the density fronts in Region 1 at $x/D = 3$ and $x/D = 7$ and in Region 2 at $x/D = 11$ and $x/D = 13$ are presented in Figures 4.11 and 4.12, respectively. In these plots the solid curves are the CFD results, and the dotted curves are the experimental results. The red curves are for the results at a height above the inlet nozzle ($z/D = +5$), the green curves at a height of the centerline of the nozzle ($z/D = 0$), and the orange and blue curves are at heights below the inlet nozzle ($z/D = -3$) and ($z/D = -5$), respectively.

(a) (b)

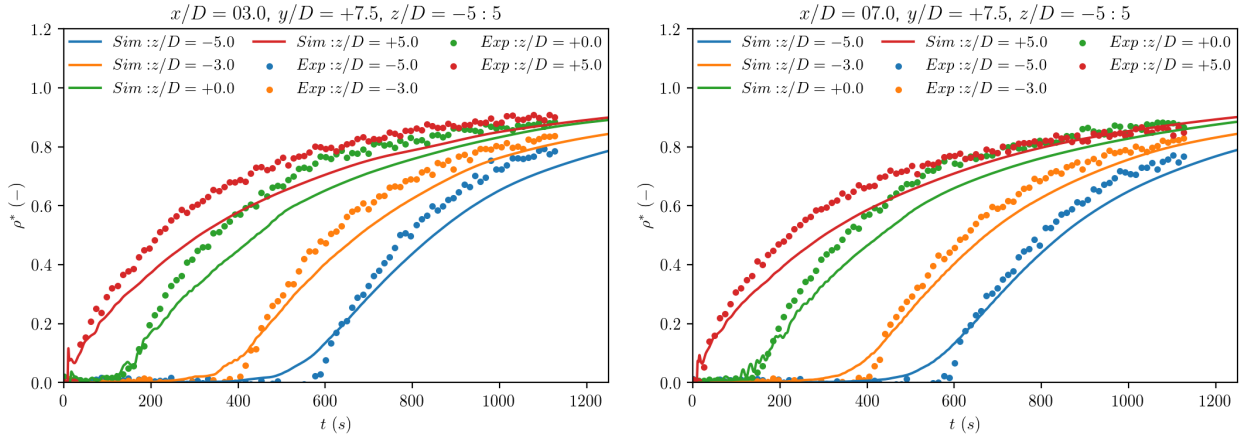

Figure 4.11: Experiments (dots) versus CFD (lines): Propagation of density fronts in Region 1: a) $x/D = 3$; b) $x/D = 7$.

The trends in the propagation of density fronts from our experiments and simulations were very similar to the trends experimentally obtained by Li et al. [51], who used a similar setup. The regions above and at the inlet height $z/D \geq 0$ are concave down throughout the transient (i.e., ρ^* is increasing at a decreasing rate). Additionally, in the regions below the inlet height $z/D < 0$, the initial increase of ρ^* starts with a positive concavity, but later the concavity of the time trace

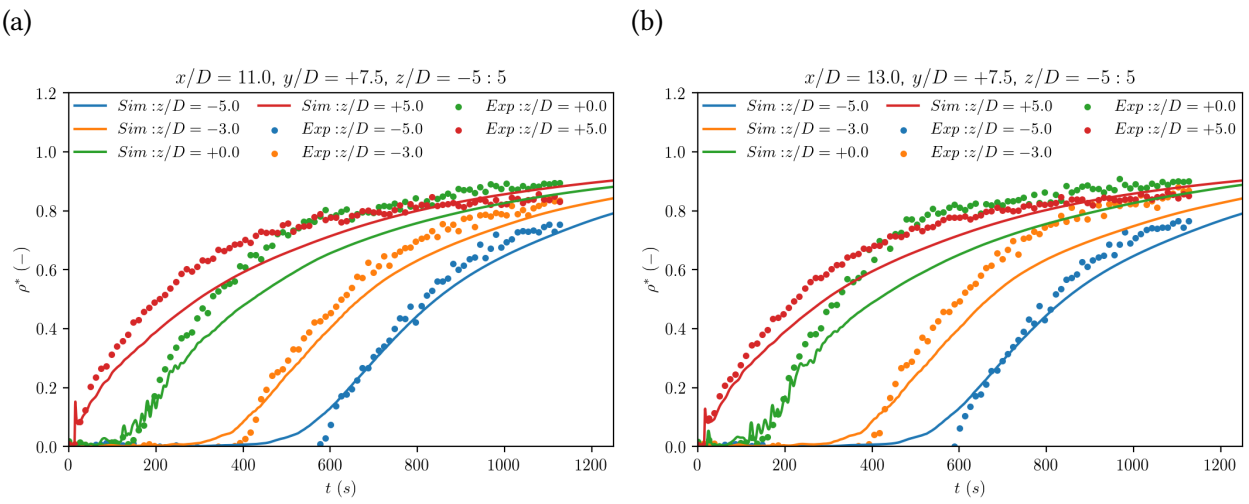

Figure 4.12: Experiments (dots) versus CFD (lines): Propagation of density fronts in Region 2: a) $x/D = 11$; b) $x/D = 13$.

becomes negative, so that the local density keeps increasing but at a slower rate.

As shown in Figure 4.11a, at $x/D = 3$ the density fronts also travel faster in the experiments than in the simulations (i.e., ρ^* increases faster in the experiments). Therefore, there is an indication of over-prediction of stratification by the CFD model. The largest differences occur at the initial increase of ρ^*, and the magnitude of the differences between the experiments and simulations are similar at all other locations. For larger time t, the differences decrease sooner at the locations at and above the inlet ($z/D = 0, +5$). Additionally, at $t \approx 1,000s$ the densities at $z/D = 0$ and $z/D = +5$ are approximately equal in the experiments ($\rho^* \approx 0.8$); however, this does not occur until about 200 seconds later in the simulations.

Farther away from the inlet wall, at $x/D = 7$ (Figure 4.11b), the curves follow the same general trends; however, ρ^* tends to be larger at $z/D = 0$ than at $z/D = +5$ at time $t > 600s$ in the experiments. This indicates that most of the incoming fluid remains at about the inlet height and that the buoyancy forces are not strong enough to rapidly move the lighter fluid upwards in the experiments, therefore, the increase in ρ^* at $z/D = +5$ is slightly slower than at $z/D = 0$. As time increases, there is a larger difference between the curves for $z/D = 0$ and $z/D = +5$ in the experiments. On the contrary, this behavior is not exhibited in the simulations even by

$t = 1250s$. In Region 2, at locations $x/D = 11$ and $x/D = 13$ (Figure 4.12) the plots of the experiments exhibit slightly more frequent fluctuations. In the experiments at $x/D = 13$, an even faster increase of ρ^* occurs for the $z/D = 0$ curve than what was observed at $x/D = 3, 7$. The experimental results at all locations, except at $z/D = +5$, still exhibit a faster traveling speed compared to the simulation results. From these observations, it can be deduced that the CFD model tends to under-predict the speed of the stratification front for the case with a 1.5% density difference. An interesting observation can be made by focusing on the propagation of the density fronts at fixed heights $z/D = -5$ and $z/D = +5$ at several x/D distances from the wall. Below the inlet, at $z/D = -5$ (Figure 4.13a) the spread of ρ^* is small in the experiments and simulations (i.e., ρ^* remains about the same regardless of x/D); however, at $z/D = +5$ (Figure 4.13b) a larger spread is observed in the experiments.

(a) (b)

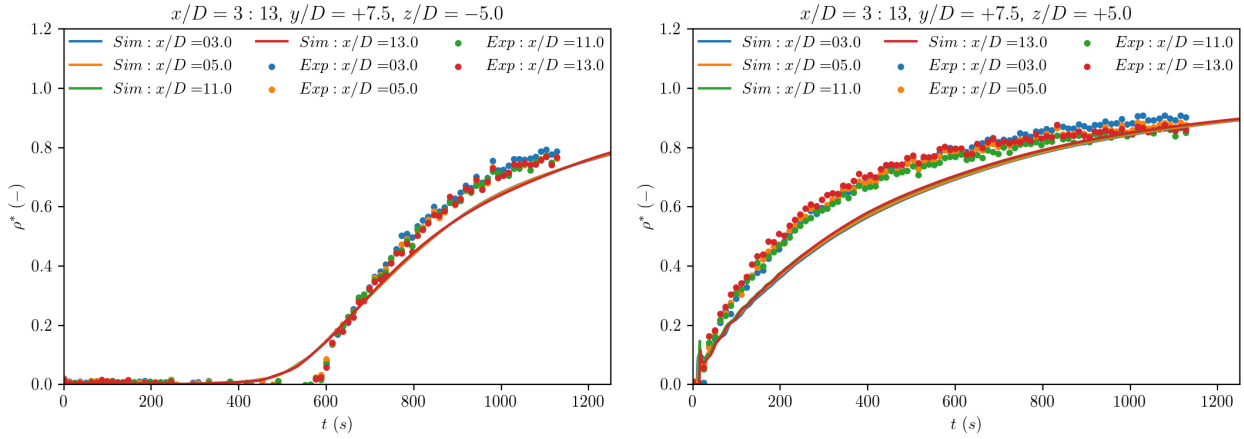

Figure 4.13: Experiments (dots) versus CFD (lines): Propagation of density fronts in Regions 1 and 2: a) $z/D = -5$; b) $z/D = +5$.

Consequently, we can now describe the stratified fronts by their speed of propagation in addition to the length of their mixing regions. While both are simple observations, they are important to understand how well the stratified fronts are predicted locally and globally by CFD simulations.

In a study reported by Dave et al. [26], where results from RANS simulations were compared

to data from experiments with density differences up to 1% (Li et al. [51]), the authors showed that their simulations over-predicted the speed of the stratification fronts. Also, the observed differences between the time histories of the experimental and computational results were much larger in their comparisons than in ours. However, the authors reported that the boundary conditions of the experiments were not described in detail (e.g., the location of the inlet measurements were not disclosed), leading to large uncertainties in the simulation results. One clear example of the importance of having detailed measurements of the boundary conditions is demonstrated in Figure 4.8. The measurement of the inlet density field clearly shows that by the time when the second fluid arrived at the inlet, stratification in the inlet pipe was already present (i.e., the values at the inlet are not uniform). Furthermore, in a study by Petrov and Manera [25], where the predictive capabilities of RANS models were assessed to predict buoyancy-driven mixing in a PWR RPV, it was found that the stratified fronts traveled faster in the simulations than in the experiments. In this case, however, a denser fluid was injected into the lighter fluid. In order to study the effect of the density gradient on the front propagation, an investigation with positive density gradient is given in Section 4.2.6.

4.2.4 Repeatability of Experimental Data

To verify the repeatability of our measurement, we repeated the experiment two additional times on separate days. We refer to the original experiment as Exp. 1 and the two new measurements as Exp. 2 and Exp. 3. The temperatures of the sugar solutions were 20°C and 22°C for Exp. 2 and Exp. 3, respectively. While the density of the new solutions remained the same, the viscosities varied within 2% of the previously measured value. A comparison between the three experiments and the simulation at various heights are given in Figures 4.14 and 4.15. Regardless of the measurement location, the three experiments show very good agreement with one another. On average, ρ^* of Exp. 2 and Exp.3 differed by about 2% from Exp. 1. This small variability between the different experiments indicates that this is a highly repeatable measurement. However, this small variability should be included as part of the uncertainty bands for the measurements. It

is important to note that the discrepancy observed between the CFD results and the experimental data do not fall within the experiments uncertainty band.

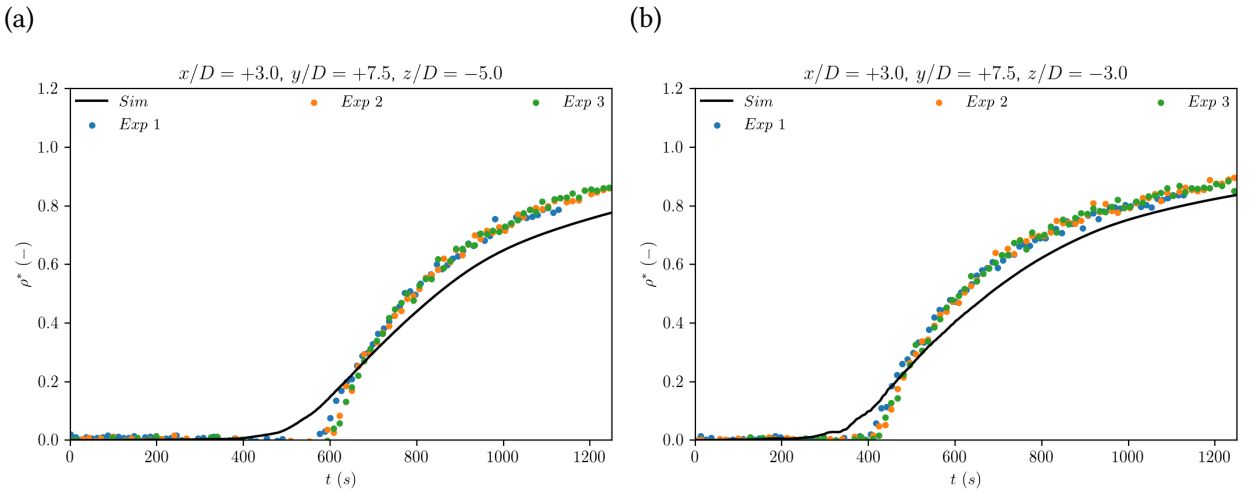

Figure 4.14: Verification of the repeatability of the propagation of stratified fronts. Experiments (dots) versus CFD (lines): a) $z/D = -5$; b) $z/D = -3$.

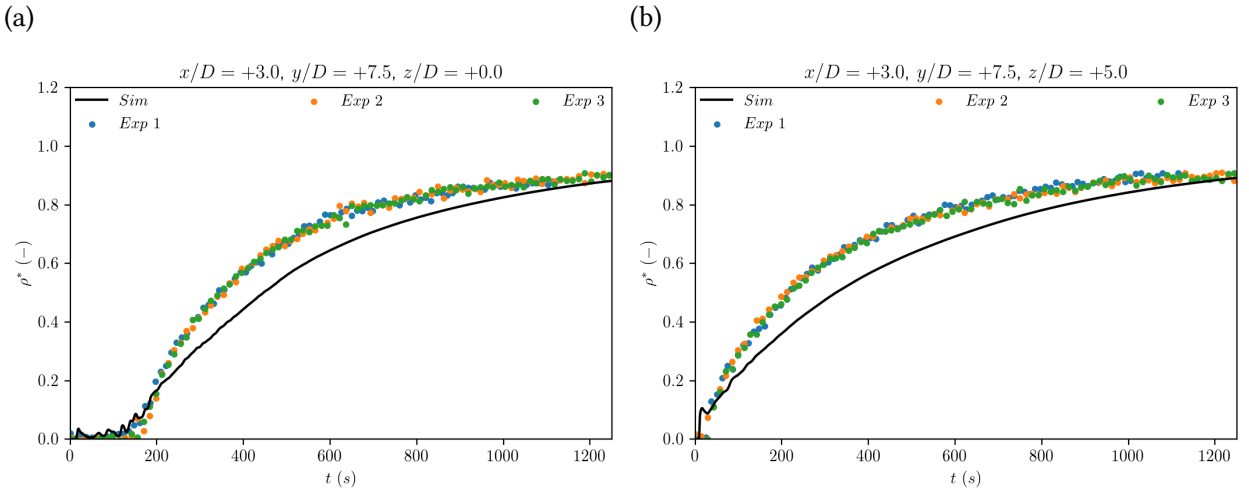

Figure 4.15: Verification of the repeatability of the propagation of stratified fronts. Experiments (dots) versus CFD (lines): a) $z/D = 0$; b) $z/D = 5$.

4.2.5 Stratified Fronts — 3% Density Difference (case 2a)

An experiment with a 3% density difference ($\Delta\rho$) was conducted to investigate any additional differences that may arise from larger density gradients. The density profiles for varying z/D locations are given in Figure 4.16a. These results resemble the profiles from the case with a 1.5% $\Delta\rho$. The RANS profiles for this case also under-predict the speed of propagation of the density fronts, but by a larger margin. Furthermore, the density profiles for varying x/D locations provided in Figure 4.16b, also show small variability as in the previous experiment.

A comparison between the results of the 1.5% and 3% $\Delta\rho$ experiments are shown in Figures 4.17 and 4.18. Above the inlet (Figure 4.17), the profiles from the experiment with 3% $\Delta\rho$ reached their maximum value faster than the case with 1.5% $\Delta\rho$. These significant differences are indicative of higher turbulence mixing in the case with the largest density gradients. The simulation results also indicate more mixing and a faster propagation of the density fronts at the highest measurement location (Figure 4.17b); however this increase is not as significant as what was observed in the experiments. At lower locations (Figure 4.18), the difference in magnitudes between profiles are less drastic. This is indicative of less turbulent mixing in the later stages of the transient event. That is, as the jet becomes less buoyant over time, the rate of mixing induced by the density gradients decreases.

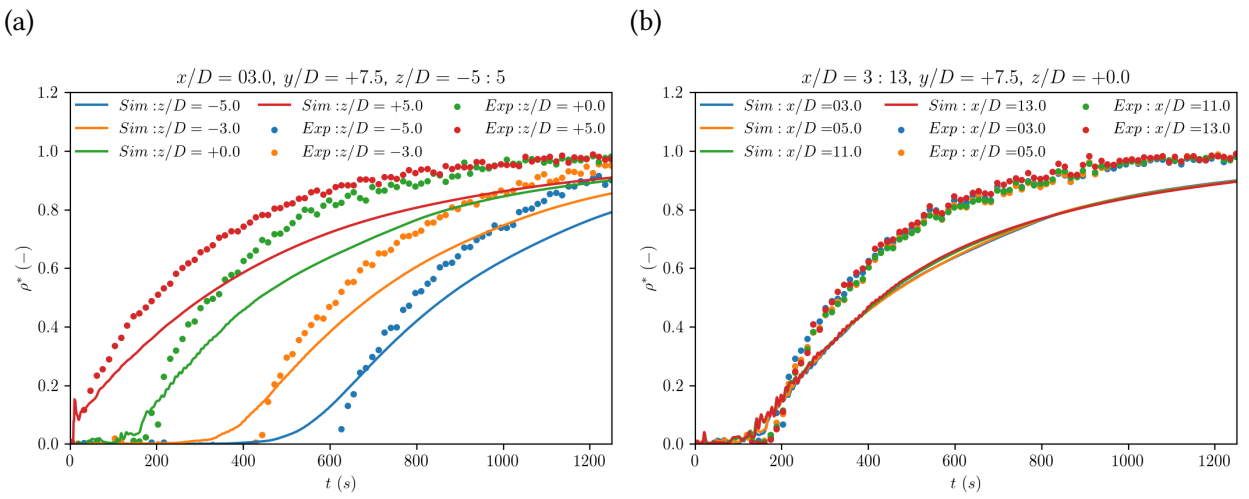

Figure 4.16: Propagation of stratified fronts for a 3% density difference. Experiments (dots) versus CFD (lines): a) At several heights at $x/D = 3$; b) At several distances away from the inlet at $z/D = 0$.

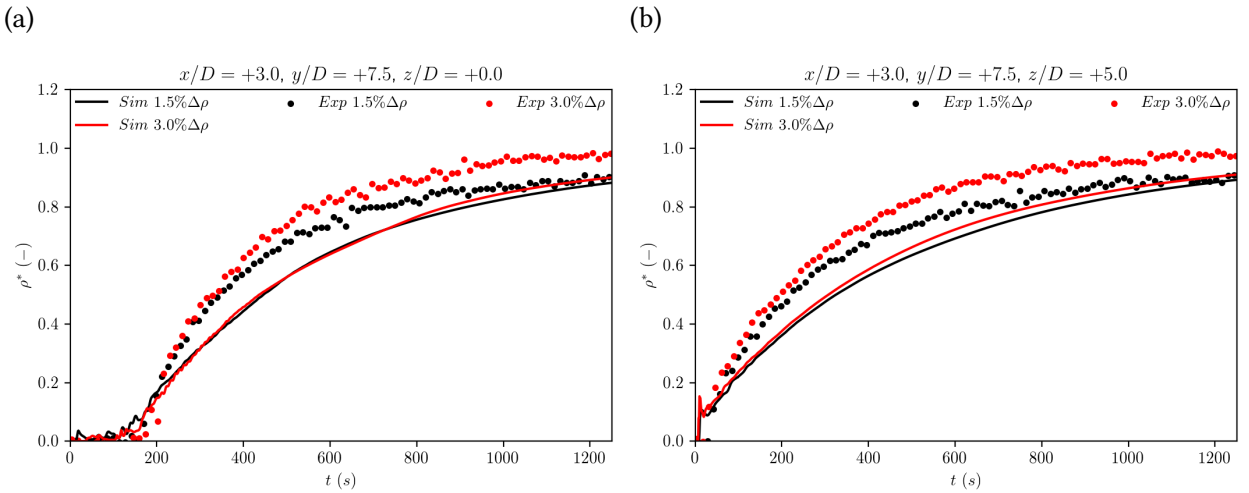

Figure 4.17: Density profile comparison of 1.5% versus 3% density difference. Experiments (dots) versus CFD (lines): a) $z/D = 0$; b) $z/D = 5$.

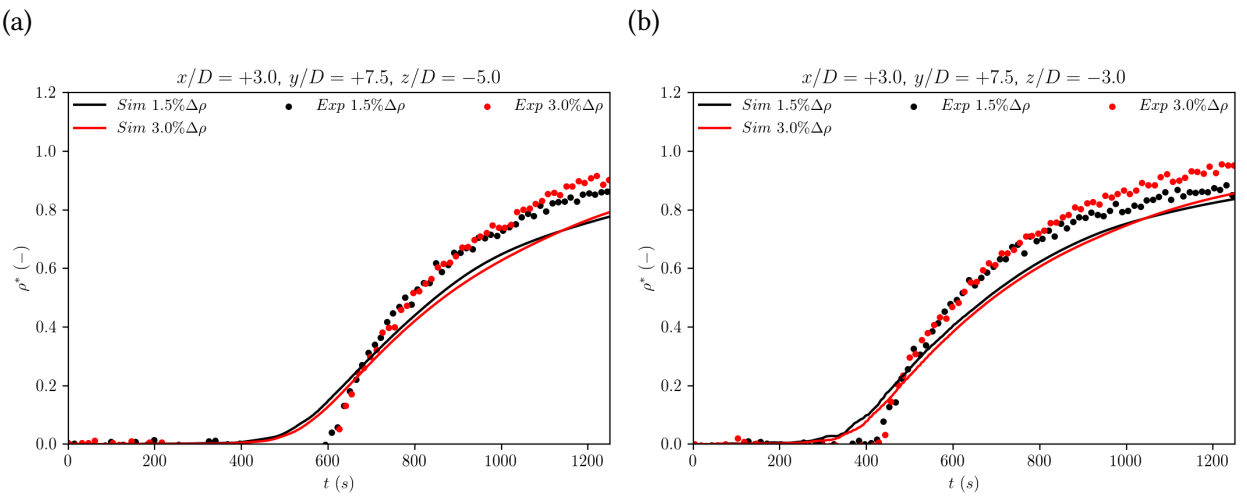

Figure 4.18: Density profile comparison of 1.5% versus 3% density difference. Experiments (dots) versus CFD (lines): a) $z/D = -5$; b) $z/D = -3$.

4.2.6 The Influence of Positive Density Gradients (case 1b)

The propagation of stratified fronts influenced by a positive density gradient was also investigated. In case 1b (see Table 4.1), a jet with 1.5% higher density was injected into the less dense environment. The fluid properties for this experiment were the same as in the experiment with the negative density gradient (see Table 4.2). The computational mesh used for the simulations in Section 4.2.2.2 were modified such that the finer grids followed the downward curvature of the jet. The mesh and velocity field at $t = 50s$ are shown in Figure 4.19.

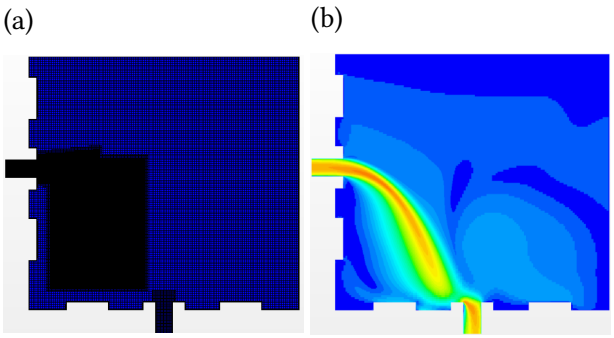

Figure 4.19: Simulation with a negative density gradient: a) Mesh; b) Velocity field of simulation at $t = 50s$.

The density fields at multiple time instants are provided in Figure 4.20. In this case, the spread

of the mixing region is sharper/thinner in the simulations than in the experiments (opposite to what was observed in the presence of a positive density feedback). For example, as marked by the red arrows in Figure 4.20c, the regions from where the green turns into dark blue are smaller in the simulations due to the lower rate of mixing (insufficient TKE).

The time histories of the density fronts in the experiments and simulations are given in Figure 4.21a. In this case, the density fronts travel faster in the simulations regardless of the probe's location. Thus, by inverting the density gradients, an over-prediction in the speed of the front occurs (consistent with the findings by Petrov and Manera [25]). This indicates that density stratification occurs much sooner in the simulation, and that the heavier fluid accumulates at the bottom of the tank. However, the decrease in ρ^* is more gradual in the experiments, and this is indicative of more mixing in the experiments with respect to the simulations (note that the opposite results were obtained in case of a positive density gradient). In comparison with the experimental results, the profiles for $z/D = -5$ and $z/D = -3$ follow the same general trends of the experiments. For example, the propagation speed is faster for $z/D = -5$ than in $z/D = -3$ for both the simulations and experiments, but the speed of the fronts at these locations equalizes at about $t = 500s$. Furthermore, the time histories at the various x/D locations (Figure 4.21b) contained very small variability as seen in the previous experiments.

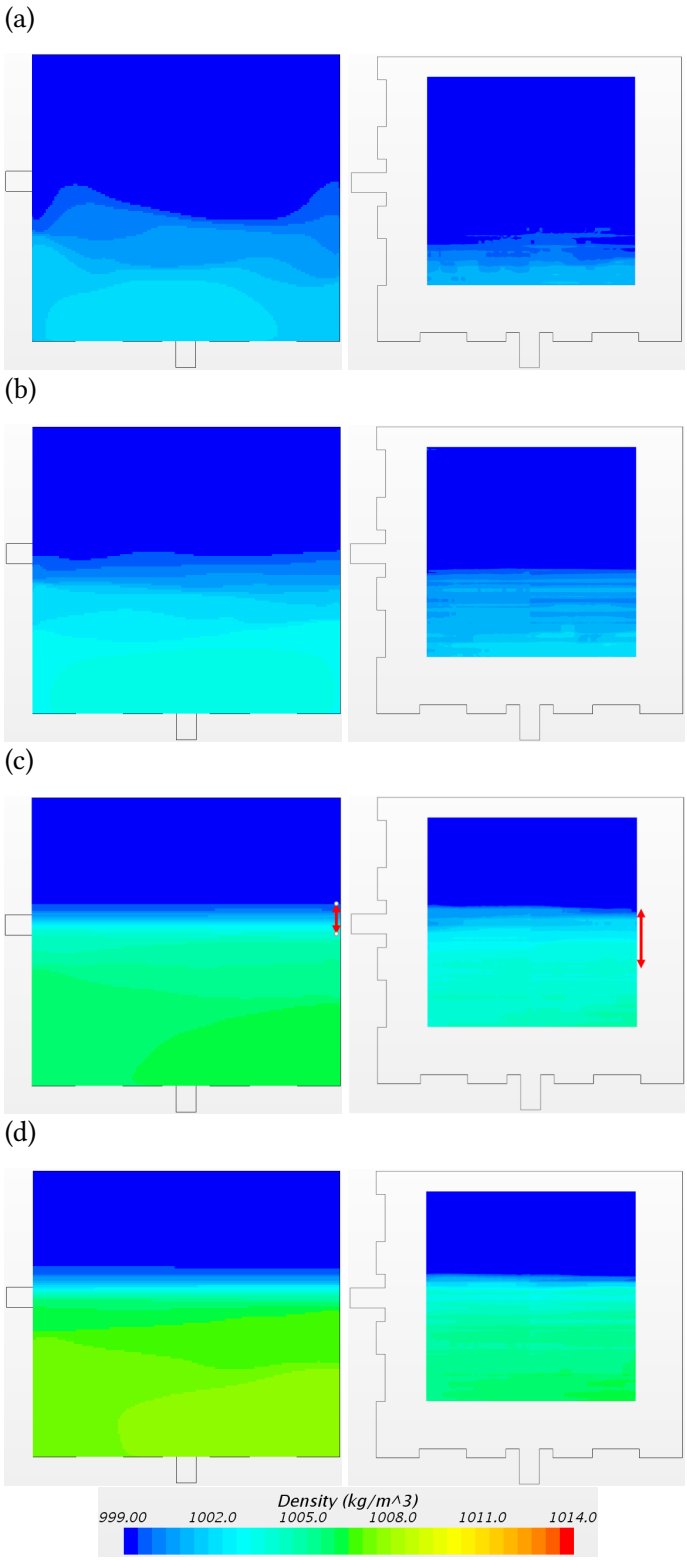

Figure 4.20: Propagation of density fronts at four different times: a) $t = 100s$; b) $t = 200s$; c) $t = 500s$; d) $t = 700s$. Simulations (left) versus experiments (right) with inverted density gradient.

(a) (b)

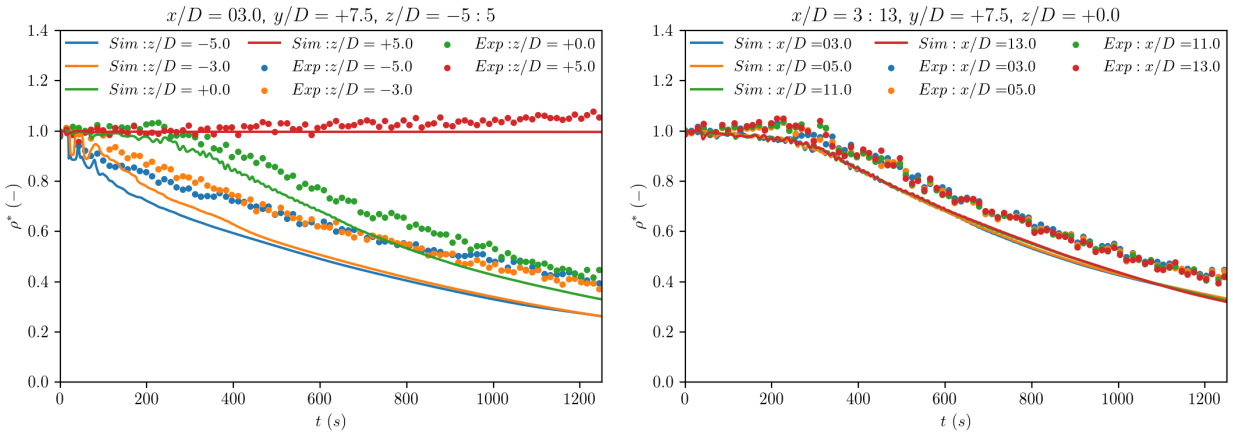

Figure 4.21: Propagation of stratified fronts for a 3% density difference. Experiments (dots) versus CFD (lines): a) At several heights at $x/D = 3$; b) At several distances away from the inlet at $z/D = 0$.

To explain the discrepancies between the RANS simulations and the experiments, we refer back to the equations of the TKE k and the turbulence dissipation rate ϵ described in Section 1.2.3.2:

$$\frac{\partial}{\partial t}(\rho k) + \frac{\partial}{\partial x_i}(\rho k U_i) = \frac{\partial}{\partial x_i}\left[\left(\mu + \frac{\mu_t}{\sigma_k}\right)\frac{\partial k}{\partial x_i}\right] + G_k + G_b - \rho\epsilon, \tag{4.6}$$

$$\frac{\partial}{\partial t}(\rho\epsilon) + \frac{\partial}{\partial x_i}(\rho\epsilon U_i) = \frac{\partial}{\partial x_i}\left[\left(\mu + \frac{\mu_t}{\sigma_\epsilon}\right)\frac{\partial \epsilon}{\partial x_i}\right] + \frac{\epsilon}{k}C_{\epsilon 1}\left(G_k + C_{\epsilon_3}G_b\right) - C_{\epsilon 2}f_2\rho\frac{\epsilon^2}{k}. \tag{4.7}$$

The discrepancies observed between the RANS simulations and the experiments could be explained by inspecting the source/sink term of k and the source/sink term of ϵ due to density gradients. The term that appears as source/sink term in the balance equation for the turbulent kinetic energy is given by Equation 4.8:

$$G_b = -\frac{1}{\rho}\frac{\mu_t}{Sc_t}\frac{\partial(\rho g_i)}{\partial x_i}, \tag{4.8}$$

where ρ is the density, g the gravity, Sc_t the turbulent Schmidt number, and the turbulent/eddy viscosity is calculated by $\mu_t = \rho C_\mu k^2/\epsilon$.

Furthermore, in the balance equation for the dissipation rate of turbulent kinetic energy (Equation 4.7), G_b also acts as source term as:

$$\frac{\epsilon}{k} C_{\epsilon 1} C_{\epsilon 3} G_b, \tag{4.9}$$

where $C_{\epsilon 3}$ is a model coefficient:

$$C_{\epsilon 3} = \begin{cases} 1 & G_b \geq 0 \\ 0 & G_b < 0 \end{cases}. \tag{4.10}$$

In the case where the heavier fluid is injected into a lighter environment, the positive density gradient ($\frac{\partial \rho}{\partial x_i} > 0$) yields a positive G_b. Therefore, the source terms for turbulent kinetic energy (TKE) and its dissipation are both positive and non-zero. From the comparison between simulations and experimental data, it can be deduced that the TKE is under-predicted in the simulation. This can be due to an over-prediction of the TKE dissipation term.

In the case where the lighter fluid is injected into an heavier environment, the negative density gradient ($\frac{\partial \rho}{\partial x_i} < 0$) yields a negative G_b. Therefore, the density difference leads to the appearance of a sink term in the balance equation for the TKE and no term in the dissipation equation. The comparison with the experimental data has shown that turbulent kinetic energy is over-predicted in this case. This means that the turbulent kinetic energy dissipation is under-predicted.

These results seem to indicate that the current model shown in Equation 4.10 produces opposite effects of what is desired and that a more adequate model (at least qualitatively) would be represented by

$$C_{\epsilon 3} = \begin{cases} 1 & G_b < 0 \\ 0 & G_b \geq 0 \end{cases}. \tag{4.11}$$

Further investigations are needed to clarify the level at which TKE is produced and dissipated by

buoyancy effects.

4.2.7 Summary of Findings

In this chapter, we provided high-resolution experimental measurements of the propagation of stratified fronts for a positively and negatively buoyant jet with a 1.5% and 3% $\Delta\rho$. Through these data, we found two processes by which these fronts can be characterized: the speed of the propagation fronts and the extension of the mixing zone around the stratified layer. In addition, we assessed the capabilities of the Standard $k\epsilon$ turbulence model to predict these two processes for the cases with negative and positive gradient environments.

In both cases, the local trends of the stratified density fronts were well predicted by the RANS simulations. However, the speed of front propagation and the extension of the mixing areas were different for both cases. When lighter fluid was injected, the fronts were found to be slower in the simulations than in the experiments. Additionally, the mixing region around the stratified front was found to be larger in the simulations. By conducting experiments with a 3% $\Delta\rho$, the same trends were observed; however, the speed of front propagation were larger than in the 1.5% $\Delta\rho$ case. When heavier fluid was injected, the opposite behaviors were observed for the two mechanisms. With the injection of the lighter fluid into a denser fluid, our observations indicate an over-prediction of turbulent mixing in the simulation (creating a larger mixing region) that can be attributed to an excess of production (or lack of dissipation) of TKE in the RANS models. In the case where a heavier fluid is injected, the opposite occurs. Furthermore, we checked the repeatability of these measurements by conducting two additional experiments. The variability in these measurements were within 2%, which is indicative of a highly repeatable experiment. Furthermore, we discussed the importance of the adequate measurement and definition of the boundary conditions, and how inadequate boundary condition representation could lead to large offsets in the speed of the propagation of the fronts.

Chapter 5

Development of an Advanced Instrumentation for Measurements of Turbulent Scalar Fluxes

In this section we present a new experimental technique aimed at the simultaneous measurement of velocity and scalar fluctuations with high spatial and temporal resolution. This experimental technique utilizes WMSs in combination with Stereo Particle Image Velocimetry (SPIV) to achieve synchronized measurements of both velocity and scalar fluctuations, and therefore of the turbulent fluxes $\overline{u_j'\phi'}$. The proof-of-concept of this measurement technique was obtained in the jet flow of the HiRJet facility. Acquired experimental data indicates a high temporal resolution of proposed technique and capabilities of achieving a high level of synchronization which is confirmed by cross-correlation between WMS and SPIV signals.

5.1 Simultaneous SPIV and WMS Measurements

The SPIV and WMS systems were arranged to operate simultaneously, in order to obtain both the velocity and concentration fields. In these measurements, the WMS frame was oriented perpendicular to the jet's main axis and placed at a streamwise location.

The laser sheet was positioned in between the WMS electrodes from one side of the tank, and the two cameras were positioned on the opposite side as shown in Figure 5.1. In this configuration, both cameras were located in the same side of the water tank in the forward direction of the scattered light. As previously demonstrated by Petrov et al. [85], this configuration provides a better signal-to-noise ratio and similar signal intensity for both cameras. However, as shown in Figure 5.2, the second camera is still affected by a stronger laser light reflection from the WMS

electrodes. Nevertheless, positioning of both cameras on the front scattering side made it possible to obtain reliable particle displacement measurements for both cameras. In order to estimate the effects of stronger light reflection on one of the cameras, velocity vectors were calculated in three different ways: (a) from camera 1 stand-alone, (b) from camera 2 stand-alone, and (c) from both cameras simultaneously. In addition, signal cross-correlations (discussed in Section 1.2.2.2) with the flow concentration obtained by WMSs were performed for each of these three cases. The operation of the two measurement systems (i.e., high-speed cameras and WMSs) was synchronized by sending a master signal (start-trigger) from the WMS unit to the PIV high-speed controller unit to start the image acquisition of the SPIV system and the signal acquisition of the WMS system.

The spatial alignment of WMS and PIV measurements was achieved by applying an image transformation. This transformation algorithm uses PIV calibration images to correct the image's perspective as shown in Figure 5.2c. In this way, the same coordinate system is used for the WMS and PIV measurements.

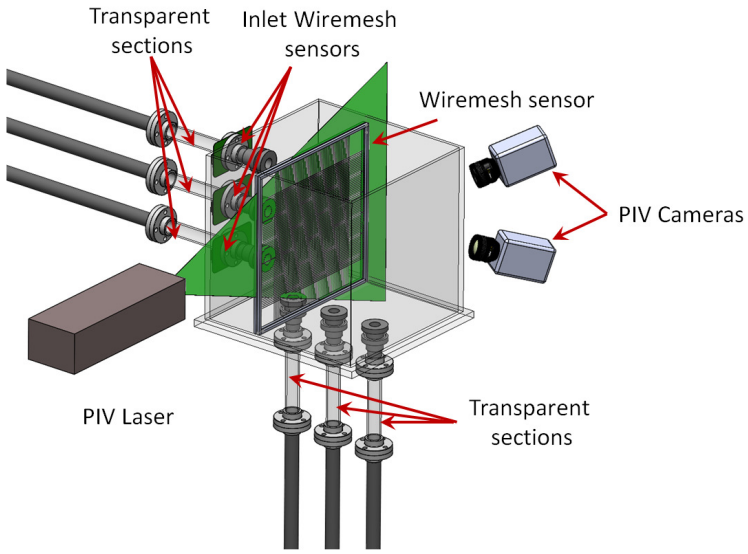

Figure 5.1: HiRJet facility with WMS and PIV instrumentation.

(a) (b)

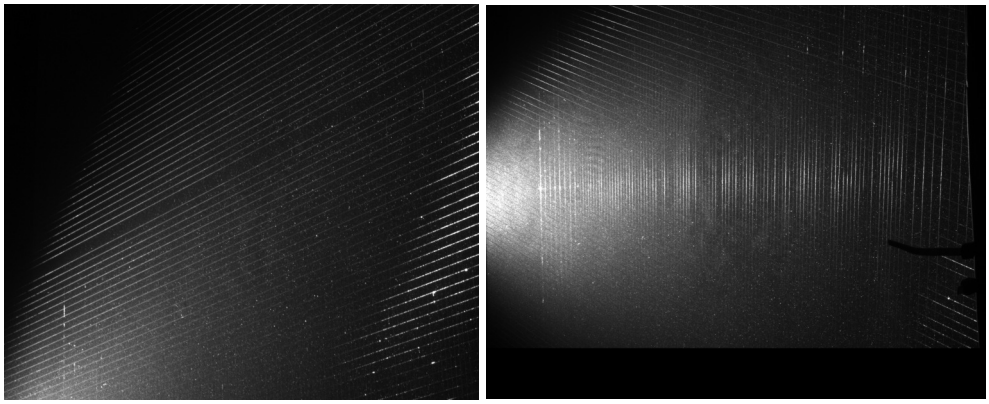

(c)

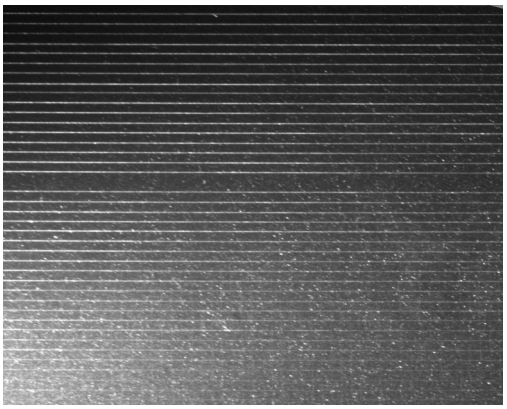

Figure 5.2: SPIV raw images: a) Camera 1; b) Camera 2; c) Camera 2 transformed.

5.1.1 Experimental results

Experiments were performed at a jet Reynolds number $Re_j = 5300$, based on the jet exit velocity U_j, the jet diameter D and the kinematic viscosity ν. Water was injected from the HiRJet central side nozzle, and the central bottom nozzle was used as an outlet. All other inlet and outlet nozzles were closed. The x, y and z coordinates represent the horizontal, vertical and spanwise directions, respectively. The origin of the coordinate system is set at the jet center, in the exit plane of the jet. The time-averaged velocity components corresponding to the x, y and z directions are U, V and W and the velocity fluctuations are u' , v' and w', respectively.

Several experiments were performed where tap water was injected into deionized water (by having different conductivities, the injected fluid acts as the tracer fluid). The measurement plane

was located at $214\ mm$ ($5.6D$) from the inlet nozzle. Data acquisition started at the time point when the injected plug appeared in the inlet WMS. For each experimental run, five points for signal processing were selected in the jet region, as indicated in Figure 5.3.

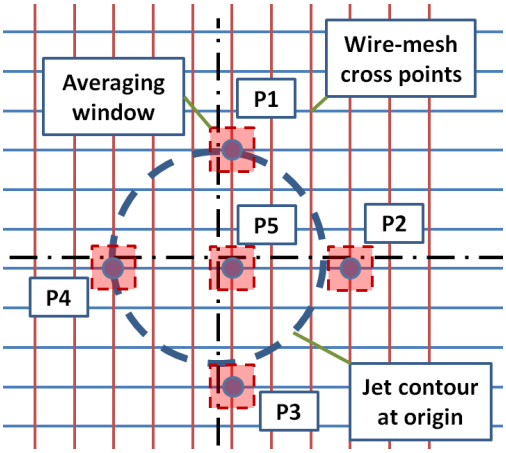

Figure 5.3: Locations for signal processing.

A LDV measurement system (Artium TRX-LDV 150 mW), was used to measure the inlet velocity profile in the transparent horizontal section at a distance of $x/D = -10$ upstream from the exit plane of the jet. The LDV probe point was traversed across the pipe diameter with a step size of $1\ mm$, acquiring 2500 measurements for each measurement position. The measured velocity profile, with its corresponding standard deviation is shown in Figure 5.4.

In order to confirm that the flow at the inlet of the test section is fully developed, the radial velocity profile measured by means of the LDV system was compared to the fully developed velocity profile calculated using the CFD code STAR-CCM+. Moreover, the $1/7$ power-law velocity profile calculated for the same mass flow rate, was also added for reference. Excellent agreement between measured and computed values is obtained in the central region of the pipe. The disagreement observed in the proximity of the pipe wall may be partly due to the loss of accuracy in the LDV measurement in this region (due to changes in index of refraction).

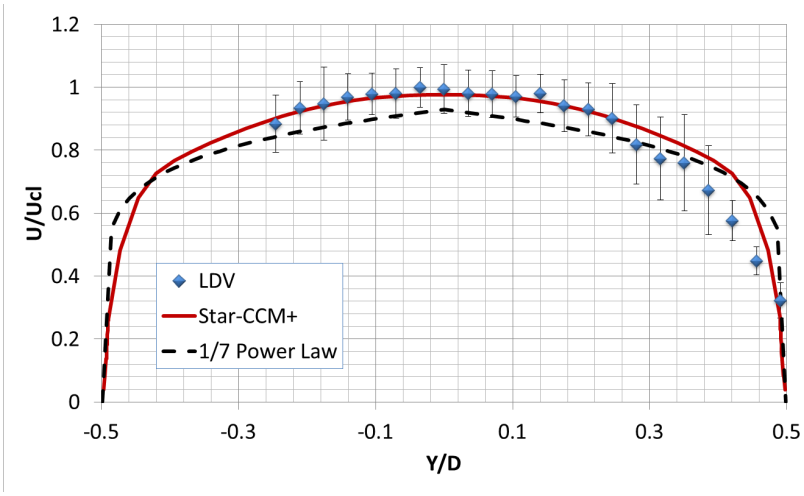

Figure 5.4: Inlet velocity profile.

5.2 Standalone WMS Results

WMS data were acquired at a frequency of $500\ Hz$ for total measurement duration of $60\ s$. Two additional separate runs, of the duration of $1\ s$ each, using only deionized water and only tap water, respectively, were performed for calibration purposes. Snapshots of the concentration fields measured at time $1\ s$, $30\ s$, and $60\ s$ are reported in Figure 5.5. Here, the concentration at the same instance at the inlet nozzle, is shown on the top left.

The frequency spectrum of the WMS data is shown in Figure 5.6. The measured spectra follow the characteristic Kolmogorov slope of -5/3 for higher frequencies and -1 slope for lower frequencies, which is typical for turbulent flows [86].

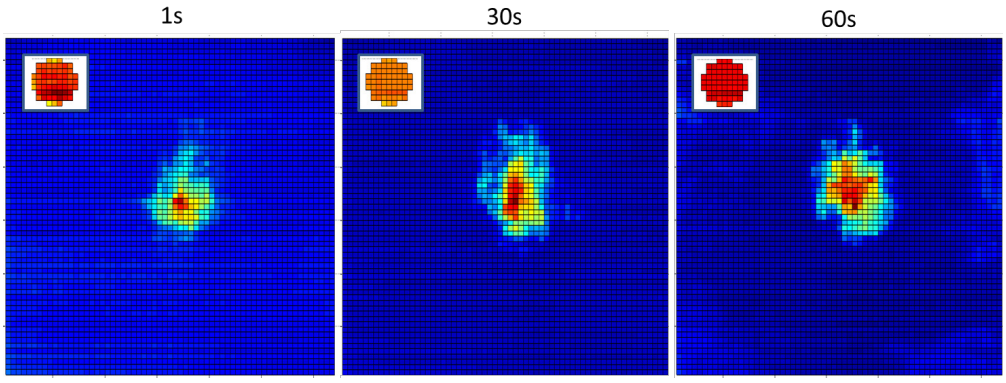

Figure 5.5: Snapshots of the concentration field at various time steps.

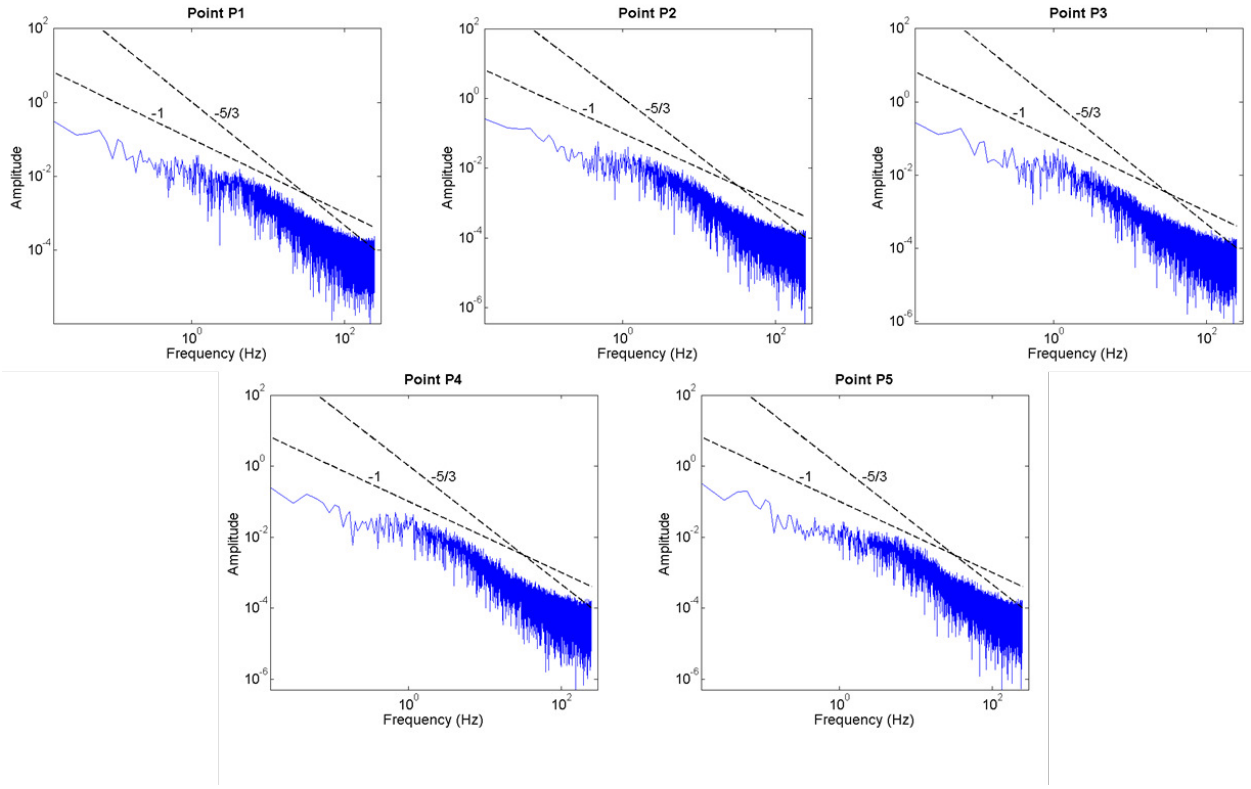

Figure 5.6: Frequency spectra of the concentration measurements (WMS).

5.3 Standalone PIV results

In Figure 5.7, the mean streamwise velocity U field, obtained from SPIV measurement at the streamwise location $x/D = 4.8$, is shown. This measurement was taken when the WMS was in its designated place.

Given the configuration of the jet with respect to the laser sheet, it can be safely assumed that the out of plane velocity is dominant. This is confirmed by the SPIV measurements reported in Figure 5.7, where the three mean velocity components U, V and W, are shown. As it was concluded in previous work [85], by having a dominant out of plane velocity component, it is possible to use two-component velocity vectors measured using a single camera in presented arrangement. However, it is important to point out that in this case the absolute velocity magnitude will differ by the presence of the projection of the other 2 velocity components.

To test the reliability of the single camera processing technique with respect to two-camera

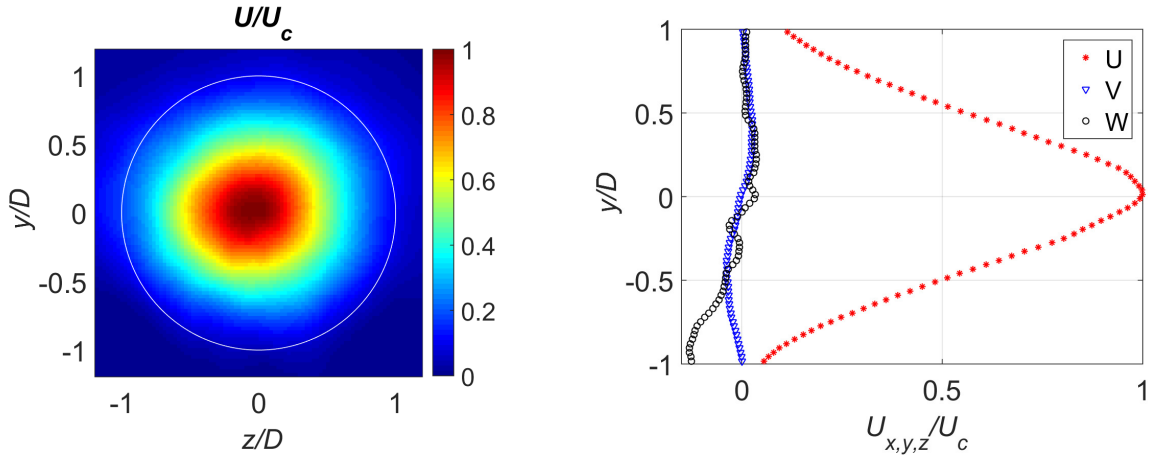

Figure 5.7: Mean streamwise velocity field U and profiles of three velocity components (U, V and W) obtained by means of SPIV measurements at streamwise location $x/D = 4.8$.

data processing, the cross correlation between the two measurements (single camera vs. two cameras) as well as the frequency spectrum of the measured instantaneous velocity were examined. In this way, it is possible to check whether the amplitude and frequency of the velocity fluctuations obtained with the two processing techniques (single camera vs. two cameras) are consistent.

The cross-correlation coefficient between velocities obtained with a single camera $u_1(\boldsymbol{x}, t)$ and with two cameras $u_2(\boldsymbol{x}, t)$ is calculated by:

$$\rho_{u_1' u_2'}(\tau) = \frac{\sum_{k=1}^{M} u_1'(t_k) u_2'(t_k + \tau)}{\sqrt{\sum_{k=1}^{M} \left[u_1'(t_k)\right]^2} \sqrt{\sum_{k=1}^{M} \left[u_2'(t_k + \tau)\right]^2}}, \tag{5.1}$$

where M is the number of data samples, and u_1' and u_2' fluctuating velocity components.

Examining Figure 5.8a, it can be concluded that the frequency spectrum of the velocity fluctuations using the stereo velocity reconstruction (SPIV) can be adequately captured by the single camera processing technique. The cross correlations between the signals obtained with single camera and SPIV are reported in Figure 5.8b. The high correlations at time lag $\tau = 0\ s$ indicate consistency between the two processing techniques.

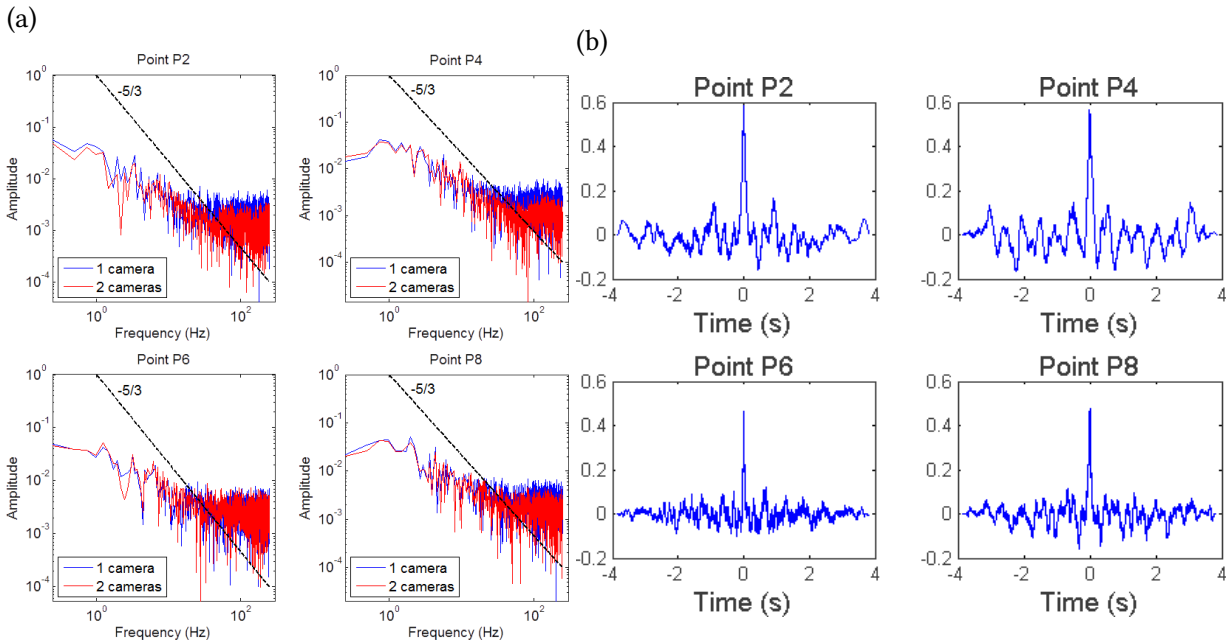

Figure 5.8: PIV results obtained by velocity reconstruction of 2 cameras vs. 1 camera: a) Spectra; b) Cross-correlation.

5.4 WMS and PIV Signal Comparison

Comparison between PIV and WMS signals in frequency domain, as well as, corresponding cross-correlations are presented in Figures 5.9, 5.10, and 5.11. Here, the equation for the correlation coefficient is given by:

$$\rho_{u_1'\phi'}(\tau) = \frac{\sum_{k=1}^{M} u_1'(t_k)\phi'(t_k+\tau)}{\sqrt{\sum_{k=1}^{M}\left[u_1'(t_k)\right]^2}\sqrt{\sum_{k=1}^{M}\left[\phi'(t_k+\tau)\right]^2}}, \tag{5.2}$$

where ϕ' is the fluctuating scalar variable.

We would like to note to the reader that the WMS signal (concentration) is averaged across a certain fluid volume, defined by the WMS probe spacing. Therefore, when correlating the signals from WMSs with the velocity signals from PIV, it is reasonable to evaluate two distinct correlations: one using the velocity measured in the center of the corresponding WMS measurement volume, and another using the velocity averaged across the corresponding WMS sensor measurement area, as indicated in Figure 5.3.

The spectra for the PIV stand-alone cases, indicate better similarity with the WMS signals (especially at the lower frequencies) than the case with both cameras; however, at higher frequencies, the signal-to-noise ratio appears to drop faster for the PIV measurements. The cross-correlations between the WMS signals with a single velocity (blue) and with a local averaged velocity (red) show strong signal correlations. However, it is evident that reflection from the wires, which appears on images from the second camera, significantly increases the noise level and leads to significant reduction in the correlation of the two signals. As expected, the correlation between the concentration and velocity measurements is higher when the average local velocity is used.

Furthermore, spatial correlations (described in Section 1.2.2.2) performed on the normalized velocity fields and normalized concentrations values for points P1, P2, P3, P4 and P5 are shown in Figures 5.12, 5.13, and 5.14. As for the single-point correlations, and also for the 2D spatial correlation, a strong correlation of velocity and concentration signals can be observed when using the velocities obtained from the camera with low light reflection (camera 1). Very low correlation without any dominant peaks is found when using the velocity from the camera 2, which experienced significant light reflection.

(a)

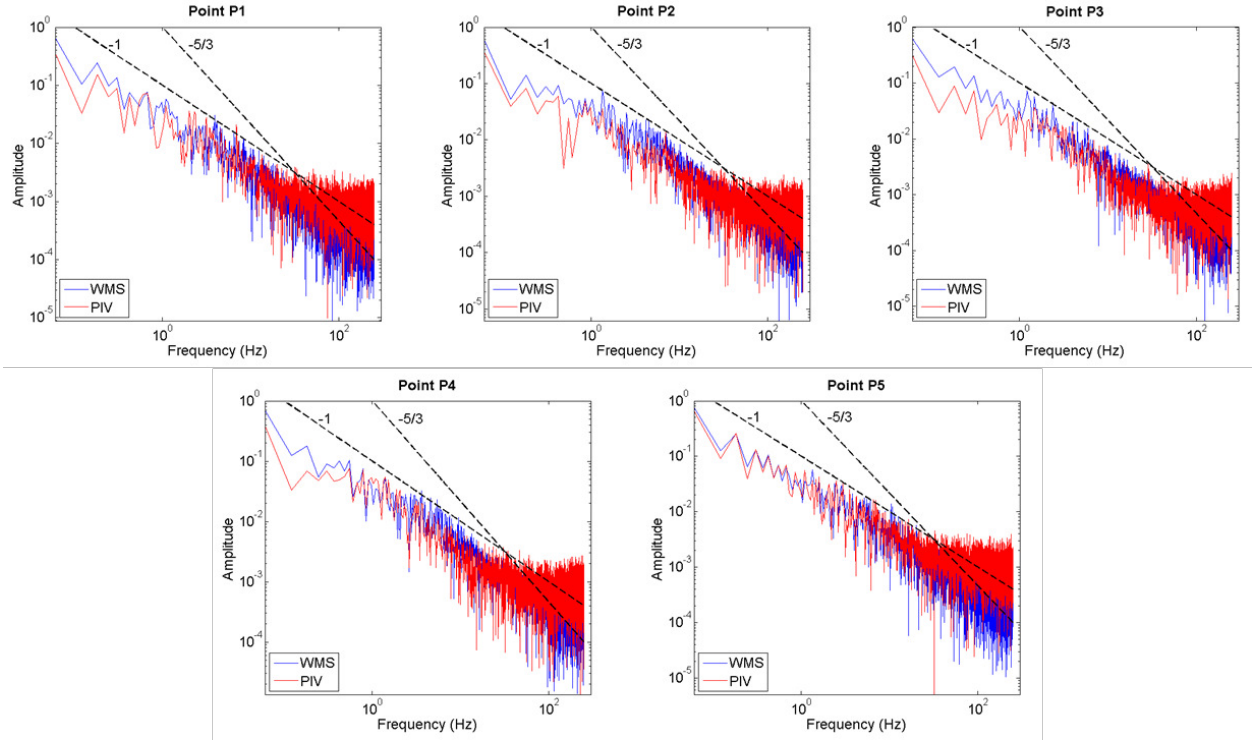

(b)

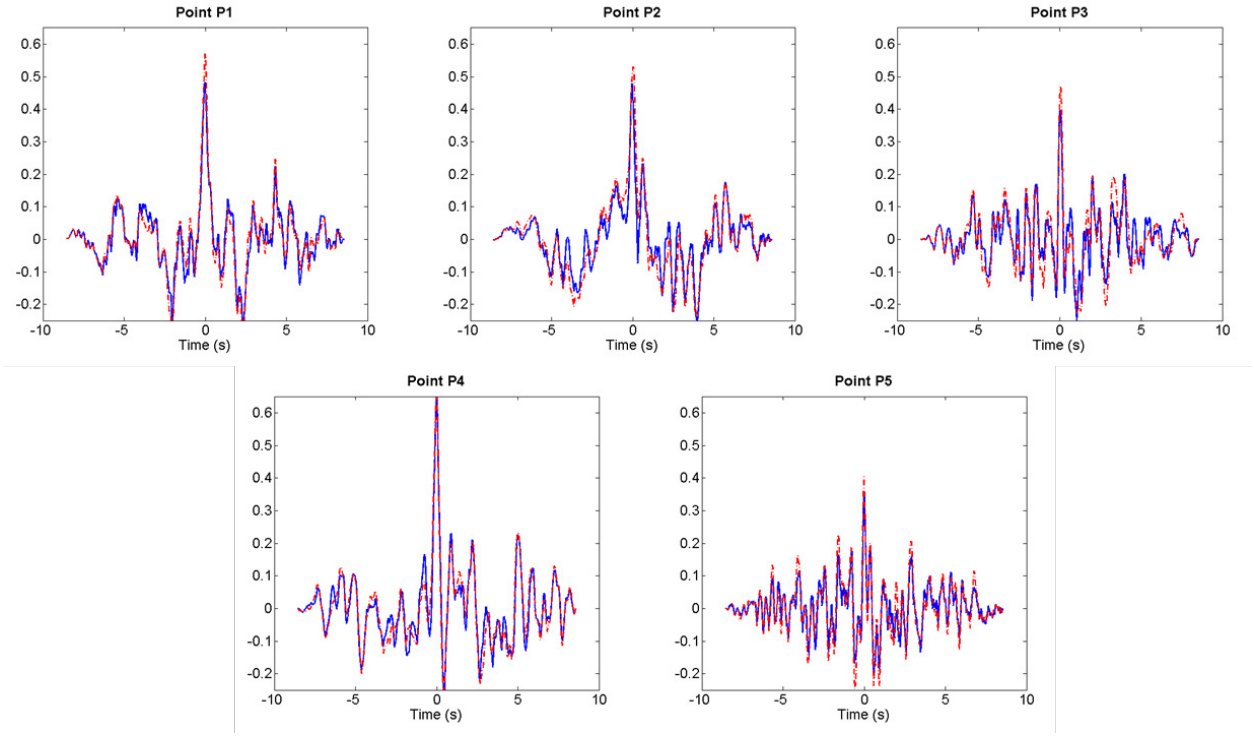

Figure 5.9: Signal comparison between the dominant velocity reconstructed from the first PIV camera (stand-alone) and the WMS concentration measurement: a) Spectra; b) Cross-correlation.

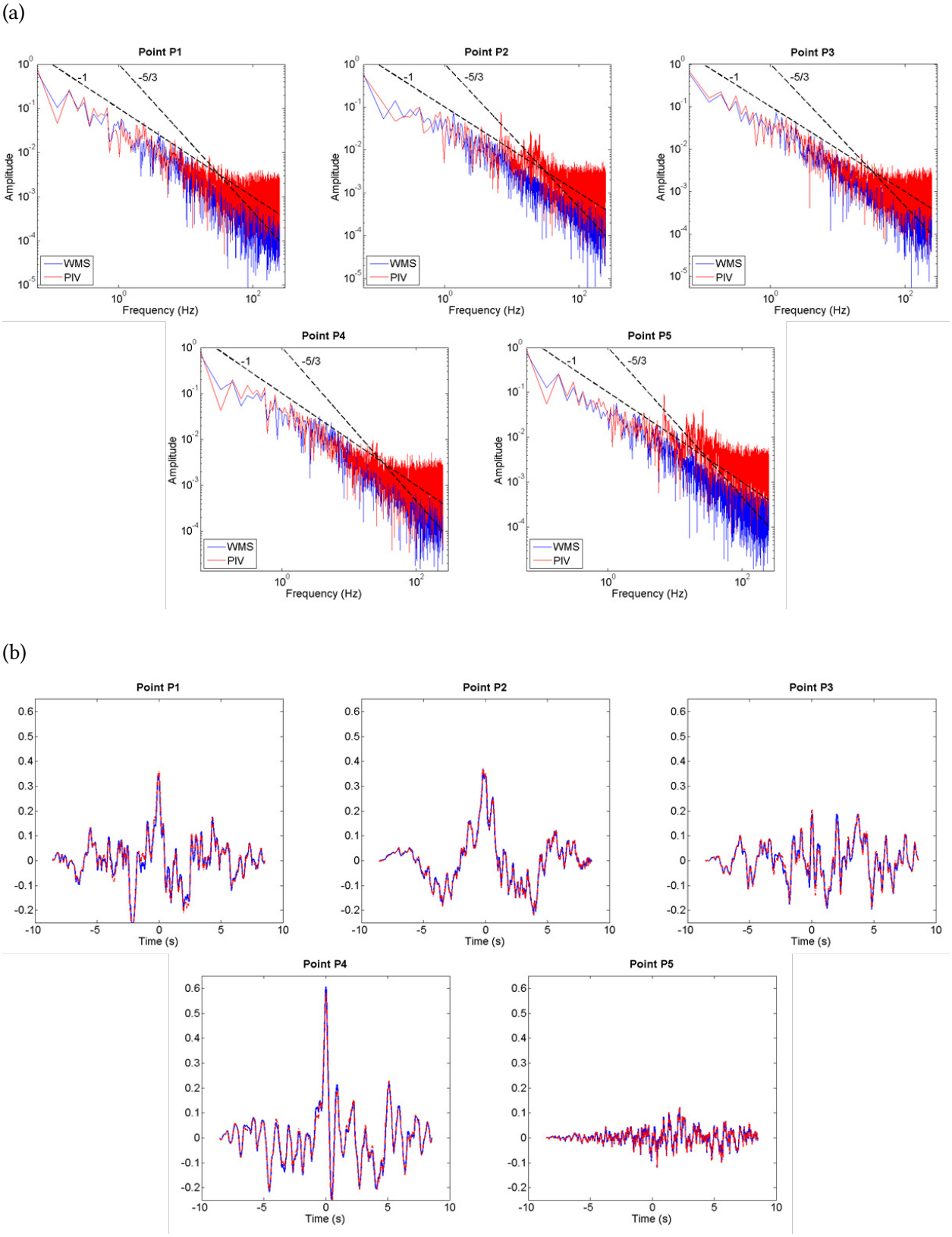

Figure 5.10: Signal comparison between the dominant velocity reconstructed from the second PIV camera (stand-alone) and the WMS concentration measurement: a) Spectra; b) Cross-correlation.

(a)

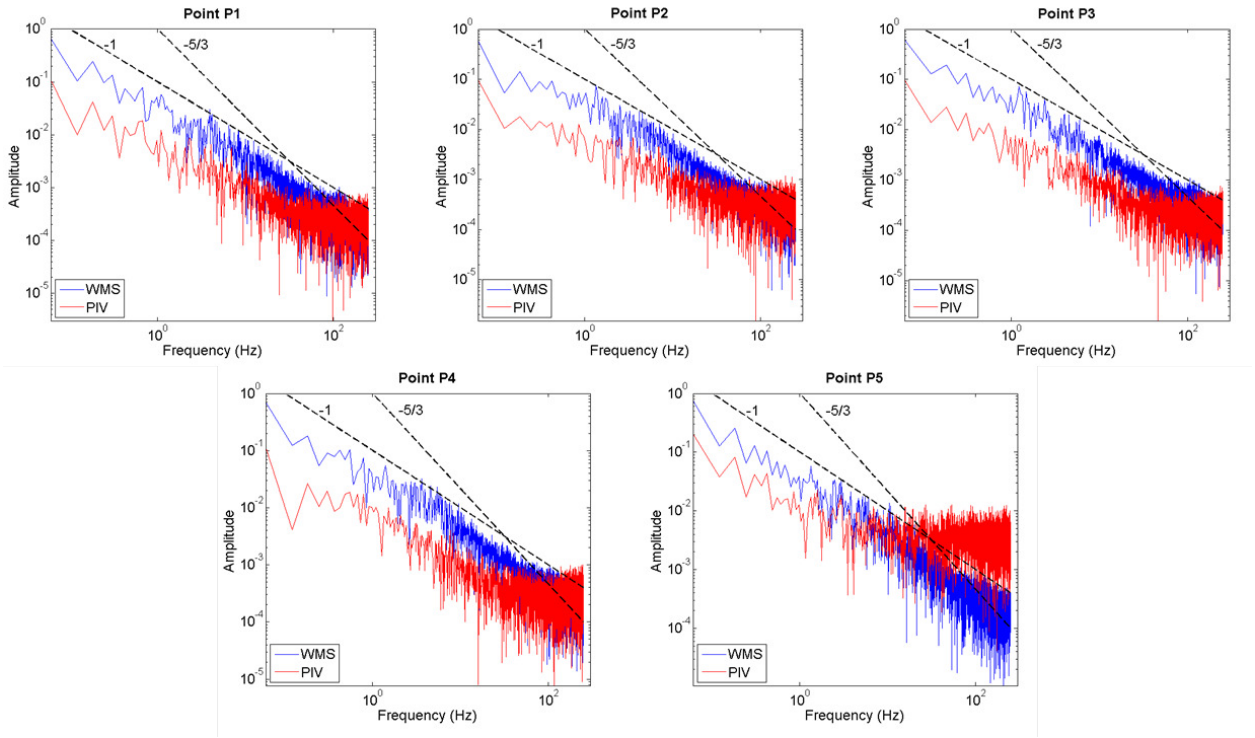

(b)

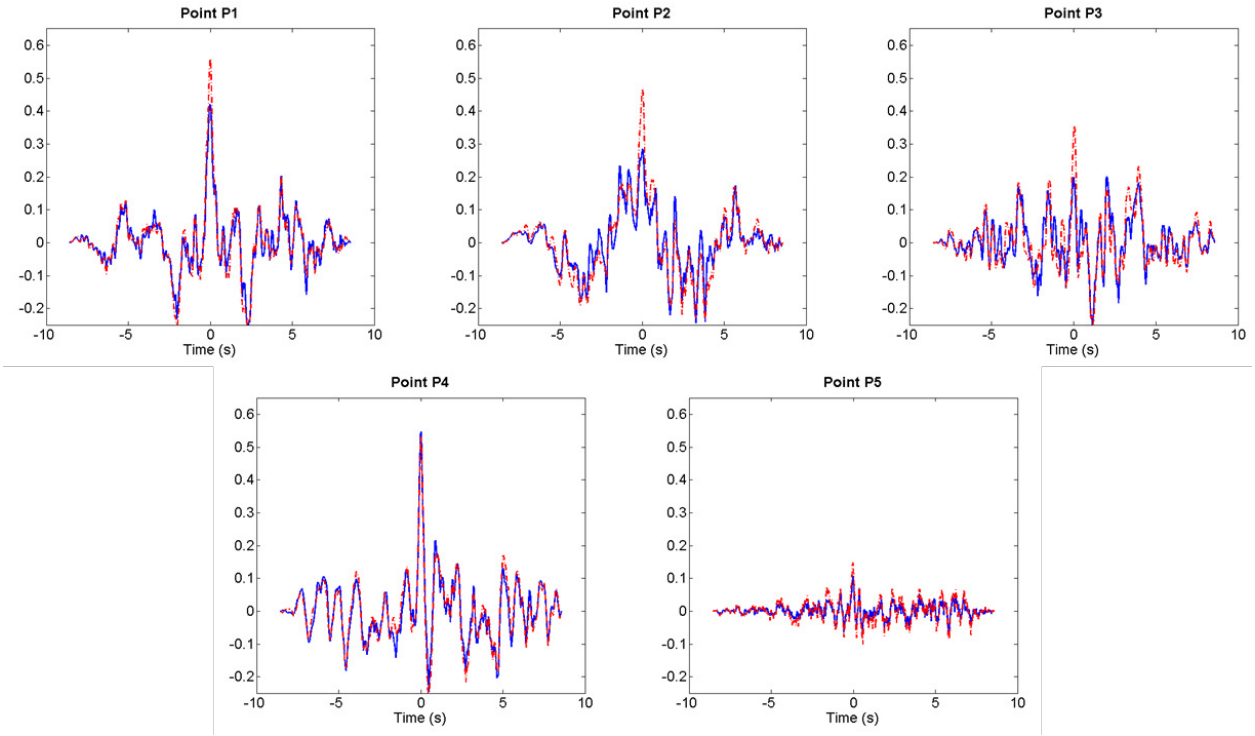

Figure 5.11: Signal comparison between the dominant velocity reconstructed from both PIV cameras and the WMS concentration measurement: a) Spectra; b) Cross-correlation.

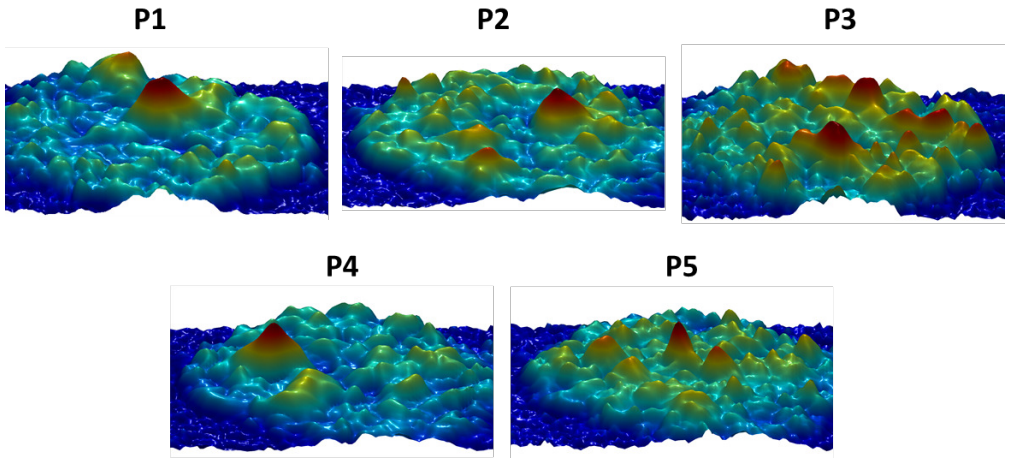

Figure 5.12: Spatial correlation for concentration and velocities reconstructed using the first PIV camera stand-alone.

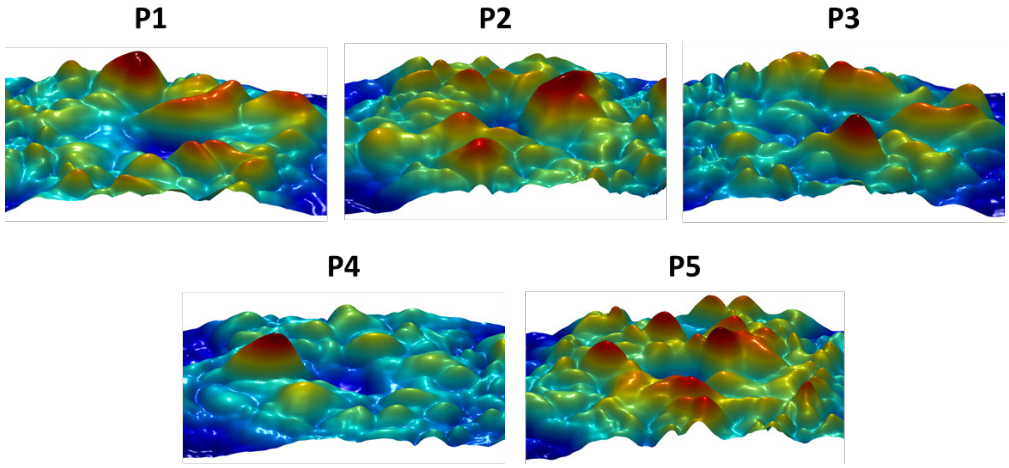

Figure 5.13: Spatial correlation for concentration and velocities reconstructed using the second PIV camera stand-alone.

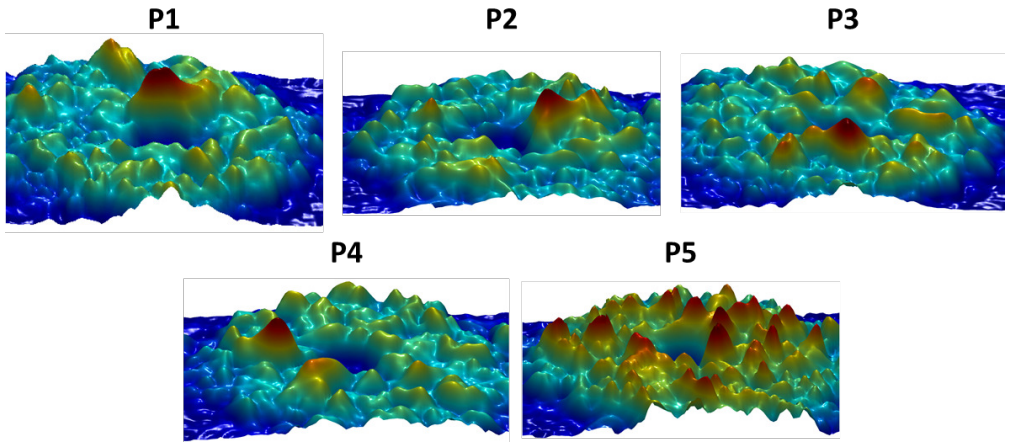

Figure 5.14: Spatial correlation for dual camera PIV processing.

5.4.1 Summary of Findings

In this chapter, a new experimental measurement technique based on the combined and synchronized use of a WMS and a PIV system was introduced. With this experimental technique, turbulent fluxes can be measured directly. The results obtained from the experiments have shown an essential signal similarity for both velocity and concentration. The cross-correlation peaks between these signals are considerable and can serve as the proof-of-concept for the experimental setup and measurement techniques discussed in this chapter. Furthermore, factors contributing to a reduction of the signal-to-noise level were successfully eliminated or significantly reduced compared to the preliminary work presented in Reference [85]; however, wire reflection still remains an issue that needs to be addressed.

Chapter 6

Conclusions and Future Work

In this chapter, we provide a summary of the contents of this thesis and provide recommendations for future work.

6.1 Conclusions

The primary goal of this thesis was to investigate selected fluid dynamics phenomena of interest for passive safety features of LWRs and advanced reactors, in order to gain more physical insight and develop a high-resolution high-fidelity experimental database that can be used for the validation and further advancement of CFD models. The focus of this thesis is on the interactions of multiple jets in a plenum and the propagations of stratified fronts in the presence of positive and negative density gradients. We utilized advanced measurement techniques to obtain high-resolution experimental data suitable for CFD validation, and assessed our data's accuracy through repeatability and reproducibility tests. In Chapter 1, we presented the motivation for our investigation of multiple jet interactions and the propagation of stratified fronts. Here, we also provided a brief theoretical background needed for the analysis of experimental data, and a description of the equations implemented in RANS-based turbulence models. Chapter 2 provided a description of the HiRJet and the RCCS separate-effects test facility, and provided an overview of the state-of-the-art measurement techniques used to acquire velocity and density distributions in these facilities.

In Chapter 3, we began with the analysis of PIV data of two, four, and six rectangular jets obtained in the RCCS facility. These measurements were obtained on the plane traversing all of the

rectangular channels. The time-averaged statistics of these three configurations were analyzed, from which their similarities and differences were described. Through convergence studies, it was confirmed that far less measurement instances are needed for the convergence of the mean flow fields compared to the Reynolds stresses. The convergence plots exhibited broader spread/scatter for the Reynolds stress components, indicating that these quantities are far more sensitive to variations in the flow. Furthermore, to verify the accuracy of the acquired PIV data, repeatability and reproducibility tests were carried out. Our analysis indicated that even in the best case scenario, where the PIV laser was not realigned for a new measurement, variations up to 2% (on average) in the mean velocity profiles, and up to 8% in the Reynolds stresses occur from variations in the boundary conditions. When the laser was realigned, with the same or with a different type of laser, the differences in the Reynolds stresses increased up to 16 %. These tests exposed the significant variations that can occur between successive PIV measurements, and that uncertainty bands that do not consider changes in the measurement conditions and human effects, do not always capture these large variabilities. Through comparisons between experimental data and results from RANS simulations of the two jet configuration, we identified the under- and over-production of the Reynolds stresses along with their consequent effects on the velocity profiles. By comparing the sources of TKE due to shear in the flow, we showed how the TKE energy is not well predicted by the RANS simulations, illustrating how these terms require further development (or tuning of the model coefficients) to predict the flows investigated herein.

We then proceeded with frequency analysis of the two jet case with time-resolved PIV data. Through PSD analysis of the two jet configuration, we discerned the dominant frequencies in the inner and outer shear layers, and associated these dominant frequencies to coherent structures in the flow through SPOD. We determined that the structures from the cross-stream velocity component, occurring at Strouhal $St = 0.47$, are responsible for the connection and interaction between the inner shear layers. These structures grow along the streamwise direction, which illustrates the stronger exchange of energy between them as the distance from the inlet increases. On the other hand, the structures from the streamwise component provided wave-like fronts os-

cillating along the streamwise direction. These fronts illustrated the propagation of the vortices in the recirculation zone and their growth and decay along the streamwise direction. Furthermore, through SPOD analysis of measurements with Reynolds numbers $Re = 6,900 - 48,500$, we determined that the coherent structures were essentially independent of Reynolds number for this range. This observation indicated that these structures are part of a common mixing mechanism which occurs at Strouhal number $St = 0.47$. Lastly, we expanded our analysis to the cases with four and six jets, where we observed the same structures at the same Strouhal number; however, the structures were not as distinct as those seen for the two jet configuration. We speculate that lack of clarity of the coherent structures in these configurations is caused by the higher local Reynolds numbers and larger feedback present when more jets are present; however, further investigations are needed to identify the lack of well defined coherent structures.

In Chapter 4, we investigated the propagation of stratified fronts in the presence of positive and negative density gradients in the HiRJet facility. Wire-mesh sensors were used to measure the time-dependent density field. The experimental data were then used to assess the RANS models. It was found that, when lighter fluid was injected into the denser fluid, the simulations over-predicted the extension of the mixing region and under-predicted the speed of the density front propagation. When heavier fluid was injected into the lighter fluid, instead, the opposite behaviors were observed. We attributed the differences between the simulations and experiments to an excess of TKE when lighter fluid is injected, and due to a lack of TKE when the denser fluid is injected. We speculate that the excess and lack of TKE in the systems are caused by the inadequate representation of the TKE dissipation rate ϵ in these RANS models. We also observed that by increasing the density differences when the lighter fluid is injected, the speed of the propagation of the fronts was found to be faster but followed the same general progression in time. Lastly, through repetitions of the experiments, we determined that the variability in these measurements were as large as 2%, and therefore, are highly repeatable.

In Chapter 5, we introduced an experimental technique to measure the correlation between local concentration and velocity fluctuations, based on the combined and synchronized use of a

WMS and a PIV system. This development enabled the simultaneous measurement of velocity and concentration fields and the direct measurement of the turbulent fluxes. The results obtained from the experiments showed an essential signal similarity for both velocity and concentration, and the cross-correlation peaks between these signals were considerable and served as the proof-of-concept for the experimental setup and measurement technique. Furthermore, we described some of the challenges encountered when utilizing this measurement technique, and outlined some routes for future improvement of this technique.

6.2 Future Work

Through the obtained measurements of velocity fields in the RCCS facility, and density distributions in the HiRJet facility, we compiled a significant amount of CFD-grade data with well defined boundary conditions. We investigated the sources for the differences between the experimental and computational data, and provided some avenues for further exploration including the further investigation of the sources of TKE due to shear and due to buoyancy effects. To expand on the discussion of the propagation of stratified fronts, experiments with higher Reynolds numbers as well as larger density differences should be carried out to explore the dependency of these quantities on the speed of the fronts and the extent of the mixing regions. Additional simulations with other RANS models as well as LES simulations, could further help identify if the observed differences occur in other simulations, or if they are only artifacts of the models used herein. Experiments utilizing the higher and lower injection nozzles can help investigate the effects of the injection height on the overall mixing mechanisms. Furthermore, through experiments using the nozzles at the bottom of the tank, discrepancies due to wall effects as well as jet curvature effects could be suppressed to simplify the phenomena under investigation.

For the RCCS facility, measurements at additional cross-sections would be of great benefit to further describe the flow fields. The utilization of other measurement techniques such Stereo PIV or Tomographic PIV would provide the third velocity component, which is a key additional information needed to understand if the differences in the Reynolds stresses are caused by the

redistribution of TKE along the third direction, which is not obtained through planar PIV. The expansion of measurements for the cases of four and six jets at various Reynolds numbers would also help with the development of our database. Lastly, to improve the measurement technique of the scalar fluxes, measurements with different types of particles and filters, would be beneficial to suppress the noise in the signals created from the laser reflections on the WMS probes.

Bibliography

[1] NRC. U.S. Nuclear Regulatory Commission (NRC), "Glossary". [Online]. Available: https://www.nrc.gov/reading-rm/basic-ref/glossary.html. [Accessed 1 July 2019].

[2] J. Duderstadt and L. Hamilton. *Nuclear Reactor Analysis*. 1976.

[3] D. Diamond, B. Bromley, and A. Aronson. Analysis of Boron Dilution Transients in PWRs. Technical report, 2002.

[4] D. Diamond, B. Bromley, and A. Aronson. Analysis of Boron Dilution Transients in PWRs. In *PHYSOR 2004 - The Physics of Fuel Cycles and Advanced Nuclear Systems: Global Developments*, pages 1–9, 2004.

[5] P. Pla, C. Parisi, R. Galetti, F. Auria, G. Galassi, and R. Reventos. Basis for calculating boron dilution scenarios in PWR by 3D neutron kinetics. In *The 14th International Topical Meeting on Nuclear Reactor Thermalhydraulics, NURETH-14*, pages 1–19, 2011.

[6] C. Tsai, M. Kazimi, and A. Henry. Three dimensional effects in analysis of PWR steam line break accident. Technical report, Energy Laboratory and Department of Nuclear Engineering - Massachusetts Institute of Technology, 1984.

[7] N. Todorova, B. Taylor, and K. Ivanov. Pressurized Water Reactor Main Steam Line Break (MSLB) Benchmark. Technical report, NEA Nuclear Science Committee, 2002.

[8] S. Schollenberger, L. Dennhardt, and B. Schoen. Primary Coolant Loop Test Facility (PKL2) Project - Final Report. Technical report, 2017.

[9] T. Takeda and I. Ohtsu. ROSA/LSTF Test and RELAP5 Analyses on PWR Cold Leg Small-Break LOCA with Accident Management Measure and PKL Counterpart Test. *Nuclear Engineering and Technology*, 49(5):928–940, 2017.

[10] C. Boyd and R. Skarda. CFD Predictions of Standby Liquid Control System Mixing in Lower Plenum of BWR. *Nuclear Engineering and Design*, 279:109–115, 2014.

[11] C. Boyd and R. Skarda. CFD Predictions of Standby Liquid Control System Mixing in Lower Plenum of BWR. Technical report, U.S. Nuclear Regulatory Commission (NRC), 2014.

[12] S. Lomperski, W. D. Pointer, C. P. Tzanos, T. Y. C. Wei, and A. R. Krauss. Generation IV Nuclear Energy System Initiative. Air-Cooled Option RCCS Studies and NSTF Preparation (ANL-GenIV-179). Technical report, 2011.

[13] O. Abdelhak, H. Mhiri, and P. Bournot. CFD analysis of thermal stratification in domestic hot water storage tank during dynamic mode. *Building Simulation*, 8(4):421–429, 2015.

[14] G. Ntinas, X. Shen, Y. Wang, and G. Zhang. Evaluation of CFD turbulence models for simulating external airflow around varied building roof with wind tunnel experiment. *Building Simulation*, 11(1):115–123, 2018.

[15] Z. Wang, H. Zhang, B. Dou, H. Huang, W. Wu, and Z. Wang. Experimental and numerical research of thermal stratification with a novel inlet in a dynamic hot water storage tank. *Renewable Energy*, 111:353–371, 2017.

[16] N. Georgiadis, D. Yoder, and W. Engblom. Evaluation of Modified Two-Equation Turbulence Models for Jet Flow Predictions. *AIAA Journal*, 44(12):3107–3114, 2006.

[17] K. Ito, K. Inthavong, T. Kurabuchi, T. Ueda, T. Endo, T. Omori, H. Ono, S. Kato, K. Sakai, Y. Suwa, H. Matsumoto, H. Yoshino, W. Zhang, and J. Tu. CFD Benchmark Tests for Indoor Environmental Problems: Part 1 Isothermal - Non-Isothermal Flow in 2D and 3D Room Model. *International Journal of Architectural Engineering Technology*, 2(1):1–22, 2015.

[18] L. Koch, J. Bridges, and A. Khavaran. Flow field Comparisons From Three Navier-Stokes Solvers for an Axisymmetric Separate Flow Jet. In *40th AIAA Aerospace Sciences Meeting & Exhibit*, pages 1–10, 2002.

[19] F. Menter, M. Kuntz, and R. Langtry. Ten Years of Industrial Experience with the SST Turbulence Model. *Turbulence, Heat and Mass Transfer 4*, 576:1–8, 2003.

[20] Z. Zhang, Z. Zhai, W. Zhang, and Q. Chen. Evaluation of Various Turbulence Models in Predicting Airflow and Turbulence in Enclosed Environments by CFD: Part 2 - Comparison with Experimental Data. *HVAC&R Research*, 13(6):871–886, 2007.

[21] E. Anderson and R. Spall. Experimental and Numerical Investigation of Two-Dimensional Parallel Jets. *Journal of Fluids Engineering*, 123(2):401–406, 2001.

[22] M. Andreani, A. Badillo, R. Kapulla, and B. Smith. Synthesis of the OECD/NEA-PSI CFD benchmark exercise. In *16th International Topical Meeting on Nuclear Reactor Thermal Hydraulics (NURETH-16)*, pages 1787–1801, 2015.

[23] S. Ghahremanian and B. Moshfegh. Evaluation of RANS Models in Predicting Low Reynolds, Free, Turbulent Round Jet. *Journal of Fluids Engineering*, 136(1):1–13, 2013.

[24] T. van Hooff, B. Blocken, and Y. Tominaga. On the accuracy of CFD simulations of cross-ventilation flows for a generic isolated building: Comparison of RANS, LES and experiments. *Building and Environment*, 114:148–165, 2017.

[25] V. Petrov and A. Manera. Validation of Star-CCM+ for Bouyancy Driven Mixing in a PWR Reactor Pressure Vessel. In *The 14th International Topical Meeting on Nuclear Reactor Thermalhydraulics, NURETH-14*, pages 1–11, 2011.

[26] A. Dave, K. Cramer, V. Petrov, and A. Manera. CFD simulations of temperature distribution in the cavity pool of an ex-vessel cooling system. In *2014 International Congress on Advances in Nuclear Power Plants (ICAPP 2014)*, pages 1–6, 2014.

[27] A. Manera and V. Petrov. Best Practices for CFD-Grade Experiments and Recent Developments in High-Resolution Measurement Techniques. In *The 18th International Topical Meeting on Nuclear Reactor Thermal Hydraulics (NURETH-18)*, pages 1–13, 2019.

[28] C. Bailly and G. Comte-Bellot. *Turbulence*. Springer International Publishing, 2015.

[29] S. Pope. *Turbulent Flows*. Cambridge University Press, 2001.

[30] P. Bernard and J. Wallace. *Turbulent Flow - Analysis, Measurement, and Prediction*. 2002. ISBN 0471332194.

[31] P. Kundu, I. Cohen, and D. Dowling. *Fluid Mechanics*. Academic Press, 2016.

[32] P. Welch. The Use of Fast Fourier Transform for the Estimation of Power Spectra: A Method Based on Time Averaging Over Short, Modified Periodograms. In *IEEE Transactions on Audio and Electroacoustics*, volume 15, pages 70–73, 1967.

[33] K. Taira, S. Brunton, S. Dawson, C. Rowley, T. Colonius, B. McKeon, O. Schmidt, S. Gordeyev, V. Theofilis, and L. Ukeiley. Modal Analysis of Fluid Flows: An Overview. *AIAA JOURNAL*, 55(12):4013–4041, 2017.

[34] J. Lumley. *Stochastic Tools in Turbulence*. Academic Press, 1970.

[35] P. Schmid. Dynamic mode decomposition of numerical and experimental data. *Journal of Fluid Mechanics*, 656:5–28, 2010.

[36] A. Towne, O. Schmidt, and T. Colonius. Spectral proper orthogonal decomposition and its relationship to dynamic mode decomposition and resolvent analysis. *Journal of Fluid Mechanics*, 847:821–867, 2018.

[37] A. Kolmogorov. The Local Structure of Turbulence in Incompressible Viscous Fluid for Very Large Reynolds Numbers. *Doklady Akademii Nauk SSSR*, 30(4):301–305, 1941.

[38] P. Durbin and B. Pettersson. *Statistical Theory and Modeling for Turbulent Flow*. Wiley, 2011.

[39] D. Laidlaw and A. Vilanova. *New Developments in the Visualization and Processing of Tensor Fields*. Springer, 2012.

[40] Siemens. *STAR-CCM+ 12.06 Documentation*. 2017.

[41] M. Raffel, C. Willert, S. Wereley, and J. Kompenhans. *Particle Image Velocimetry - A Practical Guide*. 2007.

[42] LaVision. *Particle Image Velocimetry - Product Manual*. 2018.

[43] K. Peiponen, R. Myllyla, and A. Priezzhev. *Optical Measurement Techniques*. Springer, 2009.

[44] H. Prasser, A. Bottger, and J. Zschau. A new electrode-mesh tomography for gas liquid flows. *Flow Measurement and Instrumentation*, 9:111–119, 1998.

[45] Teletronic-Rossendorf. *WMS200 Wire Mesh Sensor System Manual*. 2015.

[46] V. Petrov, D. Nunez, J. Downing, A. Dave, and A. Manera. High resolution experiments of velocity and concentration fluctuations in a jet flow. *Nuclear Engineering and Design*, 312: 361–374, 2017.

[47] M. Farmer, D. Kilsdonk, C. Tzanos, S. Lomperski, R. Aeschlimann, and D. Pointer. Topical Report : Natural Convection Shutdown Heat Removal Test Facility (NSTF) Evaluation for Generating Additional Reactor Cavity Cooling System (RCCS) Data. Technical report, 2005.

[48] R. Vilim and E. Feldman. Scalability of the Natural Convection Shutdown Heat Removal Test Facility (NSTF) Data to VHTR / NGNP RCCS Designs Nuclear Engineering Division (ANL-GenIV-049). Technical report, 2005.

[49] C. P. Tzanos. CFD Analysis for the Applicability of the Natural Convection Shutdown Heat Removal test Facility (NSTF) for the simulation of the VHTR RCCS. Technical report, 2005.

[50] T. Nguyen, V. Petrov, and A. Manera. Design of a scaled experimental facility for the NGNP Reactor. In *American Nuclear Society 2014 Winter Meeting and Technology Expo.*, 2014.

[51] Y. Li, F. Li, X. Cheng, and Y. Yang. Experimental investigation on the temperature distribution in the cavity pool of ex-vessel cooling system. *Annals of Nuclear Energy*, 53:90–98, 2013.

[52] J. Fernandez-Seara, F. Uhia, and J. Sieres. Experimental analysis of a domestic electric hot water storage tank. Part I: Static mode of operation. *Applied Thermal Engineering*, 27(1): 129–136, 2007.

[53] D. Miller and E. Comings. Force-momentum fields in a dual-jet flow. *Journal of Fluid Mechanics*, 7(2):237–256, 1960.

[54] E. Tanaka. The Interference of Two-Dimensional Parallel Jets : 1st Report, Experiments on Dual Jet. *JSME*, 13(56):272–280, 1970.

[55] E. Tanaka. The Interference of Two-Dimensional Parallel Jets : 2nd Report, Experiments on the Combined Flow of Dual Jet. *JSME*, 17(109):920–927, 1974.

[56] H. Elbanna, S. Gahin, and M. Rashed. Investigation of two plane parallel jets. *AIAA Journal*, 21(7):986–991, 1983.

[57] Y. F. Lin and M. J. Sheu. Investigation of two plane parallel unventilated jets. *Experiments in Fluids*, 10(1):17–22, 1990.

[58] Tanmoy Mondal, Manab Kumar Das, and Abhijit Guha. Periodic vortex shedding phenomenon for various separation distances between two plane turbulent parallel jets. *International Journal of Heat and Mass Transfer*, 99:576–588, 2016.

[59] N. Ko and K. Lau. Flow structures in initial region of two interacting parallel plane jets. *Experimental Thermal and Fluid Science*, 2(4):431–449, 1989.

[60] A. Nasr and J. C.S. Lai. Comparison of flow characteristics in the near field of two parallel plane jets and an offset plane jet. *Physics of Fluids*, 9(10):2919–2931, 1997.

[61] E. A. Anderson, D. O. Snyder, and J. Christensen. Periodic Flow Between Low Aspect Ratio Parallel Jets. *Journal of Fluids Engineering*, 125(2):389–392, 2003.

[62] N. E. Bunderson and B. L. Smith. Passive mixing control of plane parallel jets. *Experiments in Fluids*, 39(1):66–74, 2005.

[63] S. Lee and Y. A. Hassan. Experimental study of flow structures near the merging point of two parallel plane jets using PIV and POD. *International Journal of Heat and Mass Transfer*, 116:871–888, 2017.

[64] H. Li, N. K. Anand, and Y. A. Hassan. Computational study of turbulent flow interaction between twin rectangular jets. *International Journal of Heat and Mass Transfer*, 119:752–767, 2017.

[65] H. Li, N. K. Anand, Y. A. Hassan, and T. Nguyen. Large eddy simulations of the turbulent flows of twin parallel jets. *International Journal of Heat and Mass Transfer*, 129:1263–1273, 2018.

[66] D. Neal and B. Smith. Re-Thinking of Data Acquisition Rates in the Era of Expensive Data. In *2016 ASME Fluids Engineering Division Summer Meeting*, 2016.

[67] R. Moffat. Describing the uncertainties in experimental results. *Experimental Thermal and Fluid Science*, 1(1):3–17, 1988.

[68] M. Sullivan. *Statistics - Informed Decisions Using Data.* 4th edition, 2013.

[69] T. Nguyen, V. Petrov, and A. Manera. A separate-effect test facility for CFD-Grade measurements of the RCCS upper plenum. In *International Topical Meeting on Nuclear Reactor Thermal Hydraulics, NURETH-16*, volume 2, pages 1601–1614, 2015.

[70] R. Adrian. Twenty years of particle image velocimetry. *Experiments in Fluids*, 39(2):159–169, 2005.

[71] H. Allelein, K. Fischer, J. Vendel, J. Malet, S. Schwarz, M. Houkema, H. Paillere, and A Bentaib. International Standard Problem ISP-47 on Containment Thermal-hydraulics - Final Report. Technical report, 2007.

[72] B. Smith, J. Mahaffy, K. Angele, and J. Westin. Report of the OECD/NEA-Vattenfall T-Junction Benchmark Exercise. Technical report, 2011.

[73] M. Andreani, A. Badillo, and R. Kapulla. Synthesis of the OECD/NEA-PSI CFD benchmark exercise. *Nuclear Engineering and Design*, 299:59–80, 2016.

[74] B. Smith, M. Andreani, R. Kapulla, A. Badillo, G. Mignot, and S. Paranjape. The Nuclear Energy Agency - Paul Scherrer Institut Computation Fluid Dynamics Benchmark Exercise. Technical report, 2016.

[75] A. Boomsma, S. Bhattacharya, D. Troolin, S. Pothos, and P. Vlachos. A comparative experimental evaluation of uncertainty estimation methods for two-component PIV. *Measurement Science and Technology*, 27(9):1–17, 2016.

[76] A. Sciacchitano and B. Wieneke. PIV uncertainty propagation. *Measurement Science and Technology*, 27(8), 2016.

[77] B. Wilson and B. Smith. Uncertainty on PIV mean and fluctuating velocity due to bias and random errors. *Measurement Science and Technology*, 24(3), 2013.

[78] Z. Xue, J. Charonko, and P. Vlachos. Particle image pattern mutual information and uncertainty estimation for particle image velocimetry. *Measurement Science and Technology*, 26 (7), 2015.

[79] D. Combest, P. Ramachandran, and M. Dudukovic. On the gradient diffusion hypothesis and passive scalar transport in turbulent flows. *Industrial and Engineering Chemistry Research*, 50(15):8817–8823, 2011.

[80] R. Fox. *Models for turbulent transport*. Cambridge University Press, 2009.

[81] Z. Warhaft. Passive Scalars in Turbulent Flow. *Annual Review of Fluid Mechanics*, 32:203–240, 2000.

[82] B. Younis, C. Speziale, and T. Clark. A rational model for the turbulent scalar fluxes. In *Proceedings of the Royal Society A*, volume 461, pages 575–594, 2005.

[83] R. Sobey, A. Johnston, and R. Keane. Horizontal round buoyant jet in shallow water. *Journal of Hydraulic Engineering*, 114(8):910–929, 1988.

[84] D. Xu and J. Chen. Experimental study of stratified jet by simultaneous measurements of velocity and density fields. *Experiments in Fluids*, 53(1):145–162, 2012.

[85] V. Petrov, T. Nguyen, D Nunez, A. Dave, and A Manera. High resolution experiments of velocity and concentration fluctuations in a jet flow. In *16th International Topical Meeting on Nuclear Reactor Thermal Hydraulics (NURETH-16)*, 2015.

[86] A. Perry, S. Henbest, and M. Chong. A theoretical and experimental study of wall turbulence. *Journal of Fluid Mechanics*, 165:163–199, 1986.